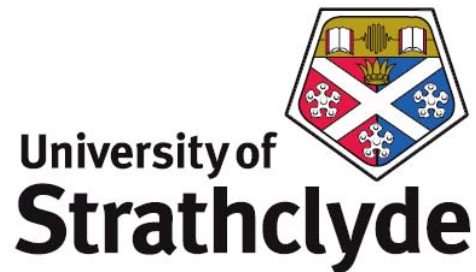


Experimental nonlinear optics for applications in optical microscopy

Greg Norris

A thesis presented in partial fulfilment
of the requirements for the degree of
Doctor of Philosophy



Department of Physics and Applied Physics
University of Strathclyde

March 2011

This thesis is the result of the author's original research. It has been composed by the author and has not been previously submitted for examination which has lead to the award of a degree.

The copyright of this thesis belongs to the author under the terms of the United Kingdom Copyright Acts as qualified for the University of Strathclyde Regulation 3.49. Due acknowledgement must always be made of the use of any material contained in, or derived from, this thesis.

Signed:

Date:

Abstract

The motivation of this thesis was to develop efficient and improved optical excitation sources for applications in confocal laser scanning microscopy (CLSM) and multiphoton laser scanning microscopy (MPLSM), with emphasis on extending the wavelength coverage of existing laser sources using nonlinear optical methods.

This included quantitative and qualitative structural analysis of periodically poled nonlinear materials using MPLSM. These materials, used in nonlinear optical frequency conversion, rely upon consistent poling lengths for quasi-phase matched operation. The described technique provided a non-destructive assessment of inhomogeneities within the crystal structure, which may impact upon frequency conversion efficiency processes.

Following this analysis, innovative pump geometries were investigated for ultra-short pulsed singly resonant synchronously pumped optical parametric oscillators (SPOPOs). Through application of a novel bi-directional pump geometry, an increase in peak power of up to 90 % was observed, with peak powers in excess of 18.8 kW generated. This substantially outperformed any pump geometry previously implemented. This source was then applied to three photon laser scanning microscopy.

Next, a visible, wavelength tunable, ultra-short pulsed source based on sum frequency mixing was developed for MPLSM at wavelengths shorter than 700nm. With average output power of ~ 150 mW, the source was applied to MPLSM of biological and non-biological UV excitable samples and results were compared with the longer wavelength Ti:Sapphire system.

Finally, a SC source and Ti:Sapphire laser were applied for optical beam induced current (OBIC) microscopy of an InGaN LED to provide information regarding the spectral response of the diode and imaging of the active region. This provided additional information regarding inhomogeneity and hence efficiency.

This one was for Granda.

Never forgotten.

Acknowledgements

The process of doing a PhD has been one of the most life-changing and rewarding experiences I have ever had. Throughout this journey I have met, and become indebted to many wonderful people.

The first person I thank is my supervisor Dr Gail McConnell, for her guidance, encouragement, friendship and continuous belief in my capabilities. Her practical skill, knowledge and ingenuity make her group a truly exciting environment to work. Gail, thank you for all the things you have taught me, the opportunities which you have given me and for being an all-round great boss.

The second person I would like to thank is Prof. Erling Riis, who has twice been charged with the task of Norris supervision. Thank you for being on hand for advice and help with various issues. Also, for the many items I have been allowed to ‘borrow’ from the photonics labs over the years, which have been much appreciated.

Further thanks go to Prof Fu-Jen Kao for his hospitality in Taipei and for the late night (for Prof Kao, due to time differences) discussions about our experiments over Skype.

Dr Brad Amos has also been a wonderful help with the many exotic and fantastic samples he has allowed me to image and for his excellent advice with all things to do with microscopy.

Additional thanks go to the last (and best) of the ‘old school’ biologists... Dr Owain Millington. Thank you for the various samples you have allowed me to test (sorry about the mosquito) and for the good chat throughout this time.

Dr John Harris must be thanked for the help, advice, and the general Rock n Roll he provided from my first day at the CfB all the way to the streets of Shanghai. Cheers man.

As a fellow member of ‘team OPO’, Dr Wei Zhang provided valuable help with practical and theoretical discussions of all things OPO. He also taught me the art of

‘borrowing’ from photonics... Big thanks for this, and for being an all around great guy.

To the ‘newer’ generation of our group, i.e. Rumelo and Alison, I have very much enjoyed your company and working with you both over the last two years. I hope I have been as much help to you, as you have been for me.

To Ewan and Bob in the photonics workshop, and to the guys in the electronics workshop, I would like to express my gratitude for all of the excellent things you have built or mended for me.

Without the following people, this experience would not have been anywhere near as enjoyable; Griff, ‘Big Tony’ Aghedu, Kyle, Dave B, Vivienne, Sarah, Fei, Shang, Craigy, Elric, Eduardo and Debbi. Also, I have really enjoyed getting to know the new SIPBS lunch crew; Tam, Mark, Dave G and Emma. A special mention must be made to Miss Debbie Allan for the early morning (and late night) coffees, which were crucial during the writing-up period. Her support and encouragement throughout this time have been great. I am sure she, more than most, will be glad not to hear the ‘T-word’ for a while

The person who would like to thank next is the guy who has certainly been the most influential on me with regards to my decision to pursue a career within physics. My big brother Ian has been an inspiration to me throughout my entire life. Having already experienced this process within the Photonics department at Strathclyde, he has always been there to point me in the right direction and steer me away from any pitfalls. His friendship, advice and intelligence have been extremely helpful to me, and I will be eternally grateful. He also taught me that having a good attitude towards any task is half the battle. Cheers buddy!

Next I would like to thank both sets of my grandparents. Their unconditional love and support throughout my whole life really is been something which I will always appreciate. They are four truly amazing people and I would like to thank them very much for everything they have ever done for me. A special thought is reserved for my Gran and Granda at this difficult time.

Finally, I would like to thank the two people who have made all of this possible. My parents have done everything they possibly can to ensure that every dream I have is fulfilled. Their constant love and encouragement have been critical to the completion of this research and I could never thank them enough. But here's a try... Thank you!!!

Table of contents

<u>Chapter 1</u>	<u>Introduction</u>	<u>1</u>
1.1	Optical microscopy and the diffraction limit	
1.2	Spatial resolution	4
1.3	Contrast mechanisms	7
1.3.1	Fluorescence	7
1.3.2	Harmonic generation	12
1.3.3	Optically induced current	14
1.4	Confocal laser scanning microscopy	16
1.5	Multiphoton laser scanning microscopy	19
1.6	Light sources for microscopy	22
1.6.1	Incoherent sources	23
1.6.2	Coherent sources	24
1.6.2.1	Lasers in CLSM	25
1.6.2.2	Lasers in MPLSM	26
1.6.2.2.1	Mode-locking	26
1.6.2.2.2	Active mode-locking	28
1.6.2.2.3	Passive mode-locking	30
1.6.2.2.4	Ultra-short pulsed lasers in MPLSM	31
1.7	Motivation	32
1.8	References	34
<u>Chapter 2</u>	<u>Theory of nonlinear optical frequency conversion</u>	<u>38</u>
2.1	Introduction	38
2.2	Elementary principles in nonlinear optical frequency conversion in bulk media	39
2.3	Sellmeier equation and dispersion	41
2.4	Anisotropy	44
2.4.1	Uniaxial and biaxial crystals	44

2.5	Nonlinear d coefficient	45
2.6	Phase matching (Type I and Type II)	47
2.7	Quasi-phase matching	49
2.8	Periodically poled Lithium Niobate (PPLN) fabrication	51
2.9	Material tolerance	52
2.9.1	Walk-off	53
2.9.2	Spectral acceptance	55
2.9.3	Temperature acceptance	56
2.9.4	Angular acceptance	56
2.10	Nonlinear optical frequency conversion in optical fibres	57
2.10.1	Overview of photonic crystal fibres	58
2.10.1.1	Self-phase modulation	59
2.10.1.2	Raman scattering	60
2.11	Conclusion	60
2.12	References	61

Chapter 3 Non-destructive analysis of periodically poled Lithium Niobate using optical microscopy techniques 64

3.1	Introduction	64
3.2	Experiment	69
3.3	Results	72
3.4	Conclusions	76
3.5	References	77

Chapter 4 Single-pass, double-pass and bi-directional pump geometries for improved efficiency synchronously pumped optical parametric oscillators 80

4.1	Introduction and motivation	80
-----	-----------------------------	----

4.1.1	Historical review of optical parametric oscillators	82
4.2	Optical parametric processes	82
4.2.1	Optical parametric amplification	85
4.2.2	Optical parametric oscillation	86
4.2.2.1	Singly resonant oscillation	87
4.2.2.2	Doubly resonant oscillation	89
4.3	Optical parametric oscillator design	90
4.3.1	Synchronously pumped optical parametric oscillators	91
4.3.1.1	Pump lasers for SPOPOs	92
4.3.2	Crystal selection	95
4.3.3	Wavelength control	96
4.3.4	OPO cavity design	99
4.4	Experiment	102
4.4.1	Single pass pumping SPOPO	102
4.4.2	Double pass pumping SPOPO	107
4.4.3	Bi-directional pumping SPOPO	110
4.5	Results	112
4.5.1	Single pass pumping SPOPO: Results	112
4.5.2	Double pass pumping SPOPO: Results	118
4.5.3	Bi-directional pumping SPOPO: Results	120
4.6	Discussion	123
4.7	Application of the bi-directional pumped SPOPO to three photon laser scanning microscopy	125
4.8	Conclusion	131
4.9	References	132

Chapter 5 Femtosecond-pulsed tunable visible laser source for short-wavelength two photon microscopy 137

5.1	Introduction	137
5.1.1	Light sources for ultraviolet excitation	137

5.1.2	Challenges and limitations in application of ultraviolet radiation in optical microscopy	139
5.2	Sum frequency mixing: Theory	141
5.3	Sum frequency mixing: Geometries	144
5.3.1	Single-pass pumping	145
5.3.2	Extra-cavity pumping	146
5.3.3	Intra-cavity pumping	148
5.4	Sum frequency mixing: Experiment	150
5.5	Sum frequency mixing: Results	153
5.6	Application and comparison of a Ti:Sapphire laser and a SFM source for two photon microscopy: Experiment	157
5.7	Application and comparison of a Ti:Sapphire laser and a SFM source for two photon microscopy: Results	161
5.8	Conclusion	168
5.9	References	169
<u>Chapter 6</u>	<u>AC and DC optical beam induced current microscopy of InGaN light emitting diodes</u>	<u>174</u>
6.1	Introduction	174
6.2	Theory of AC detection	177
6.3	Experimental method	178
6.3.1	One photon and two photon DC OBIC: Experiment	180
6.3.2	Two photon AC OBIC: Experiment	183
6.4	Analysis method	184
6.5	Results and discussion	185
6.5.1	DC spectral response: one photon DC OBIC	185
6.5.2	DC spectral response: two photon DC OBIC	187
6.5.3	AC spectral response: two photon AC OBIC	188
6.5.4	Frequency Modulation: two photon AC OBIC	190
6.5.5	Phase variation: two photon AC OBIC	191

6.6	Conclusion	193
6.7	References	195
Chapter 7	Conclusion	198
<hr/>		
7.1	Review	198
7.2	Future work	200
7.3	References	201

Journal articles

- Harris J, Norris G and McConnell G, Characterisation of periodically poled materials using nonlinear microscopy, *Optics Express* 16 (8) 5667-5672 (2008).
- Norris G and McConnell G, Relaxed damage threshold intensity conditions and nonlinear increase in the conversion efficiency of an optical parametric oscillator using a bi-directional pump geometry, *Optics Express* 18 (5) 3993-3999 (2010).

Conference proceedings

- Harris J, Norris G, Esposito E and McConnell G, Characterisation of periodically poled materials using multi-photon microscopy, *Focus on Microscopy*, Osaka (2008).
- Harris J, Norris G and McConnell G, Characterisation of periodically poled materials using multi-photon microscopy, QEP-18, Edinburgh (2008).
- Norris G and McConnell G, A fs-pulsed synchronously pumped optical parametric oscillator developed for three-photon and third harmonic generation microscopy, *Focus on Microscopy*, Krakow (2009).
- Norris G and McConnell G, Doubling the peak output power of a synch-pumped optical parametric oscillator through a novel pump geometry, *Biophotonics: Technology and Applications*, London (2009).
- Norris G, Kao F-J and McConnell G, Single-photon and two-photon DC and RF optical beam induced current microscopy of InGaN light emitting diodes, *Focus on Microscopy*, Shanghai (2010).
- Norris G and McConnell G, Novel bi-directional pump geometry for synchronously pumped optical parametric oscillators with a nonlinear increase in output power for application in microscopy, *Focus on Microscopy*, Shanghai (2010).

Abbreviations

AOM	Acousto-optic modulator
CLSM	Confocal laser scanning microscopy
cw	Continuous wave
DFM	Difference frequency mixing
DRO	Doubly resonant oscillator
EOM	Electro-optic modulator
GVD	Group velocity dispersion
GVM	Group velocity mis-match
IR	Infrared
LED	Light emitting diode
MPLSM	Multiphoton laser scanning microscopy
NA	Numerical Aperture
NIR	Near-infrared
OBIC	Optical induced current
OPA	Optical parametric amplification
OPO	Optical parametric oscillator or oscillation
PMT	Photo-multiplier tube
PPLN	Periodically poled Lithium Niobate
PSD	Phase sensitive detection
QPM	Quasi phase matching
ROI	Region of interest

SA	Saturable absorber
SC	Supercontinuum
SESAM	Semi-conductor saturable absorbing mirror
SFM	Sum frequency mixing
SHG	Second harmonic generation
SHG LSM	Second harmonic generation laser scanning microscopy
SPM	Self-phase modulation
SPOPO	Synchronously pumped optical parametric oscillator
SRO	Singly resonant oscillator
UV	Ultraviolet
ZDW	Zero dispersion wavelength

Chapter 1 Introduction

1.1. Optical microscopy and the diffraction limit

The challenge of viewing samples on a microscopic scale has been one that has motivated scientists for hundreds of years. The first instruments used for resolving beyond the capabilities of the human eye were simple arrangements using a single bi-convex lens such as that seen in Fig 1.1.

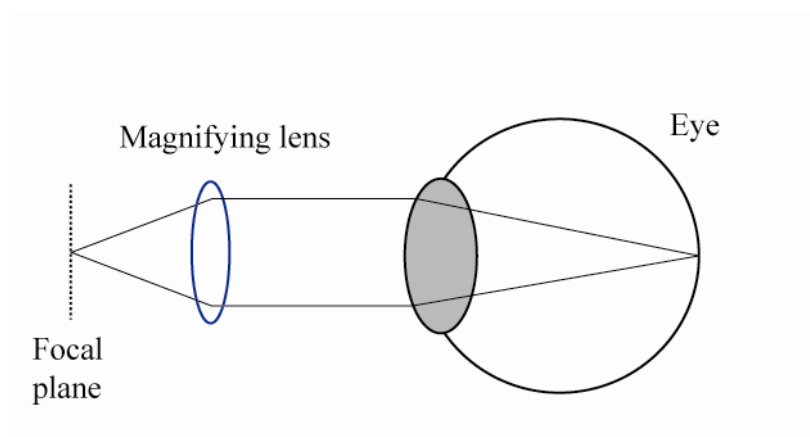


Figure 1.1 A simple magnifier

By placing an object at the focal plane of a short focal length lens, the object was therefore imaged at infinity. The resulting wide angular separation between point sources of light was produced by an illuminated sample. The cornea and lens of the eye could then be used to form the final image onto the retina.

In order to improve the resolution of this simple magnification technique, the compound microscope was created in the early 17th century by Robert Hooke [1]. This technique involved the implementation of two lenses, namely an objective lens and an eyepiece.

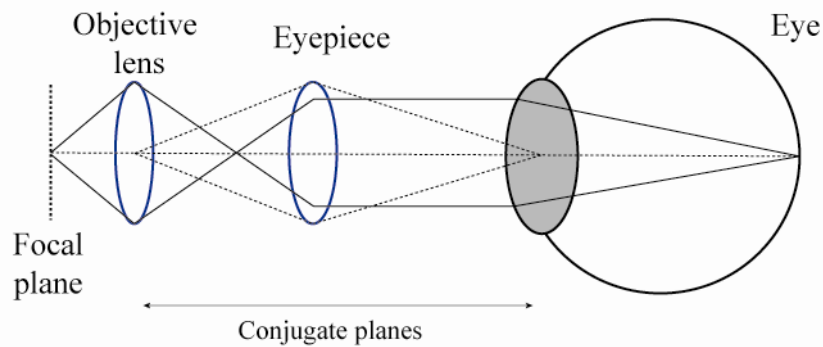


Figure 1.2 Compound microscope

An objective lens with a short focal length was placed close to a sample. The objective lens generated a real image at the focus of the eyepiece, causing the light to become focused at infinity (similar to the role of the magnifying lens shown in Fig. 1.1). Again the eye creates the final magnified, virtual image. It was important that the eyepiece had a variable control upon distance in order to ensure that the back of the objective and the pupil of the eye were at conjugate planes [1, 2].

One of the first amendments to Hooke's compound microscope was the introduction of a bright source of illumination underneath the sample. He used a liquid-filled globe to project the flame from an oil lamp onto the specimen. This technique is known as bright-field microscopy and is still recognisable as transmission microscopy methods used by many researchers today. In place of Hooke's liquid filled globe, the modern day microscope uses a white light source that is focused onto the sample using a condenser lens. By illuminating the sample and hence improving the contrast, images could be vastly improved. This will be described in more detail in Sections 1.2 and beyond.

Illumination of a sample is one of the most important factors in achieving a high contrast image. Many of the early forms of illumination, such as that used by Hooke, were subject to ghosting and non-uniform illumination over the field of view. This

was due to inhomogeneities in the light source and/or the method used to bring the light to the sample. In 1893, August Köhler presented a method which addressed this problem, providing uniform illumination over the field of view, even for non-uniform sources. This method is known as Köhler illumination and requires the additional implementation of a field stop diaphragm, a condenser aperture and a collective and condenser lens to the previous compound microscope [3].

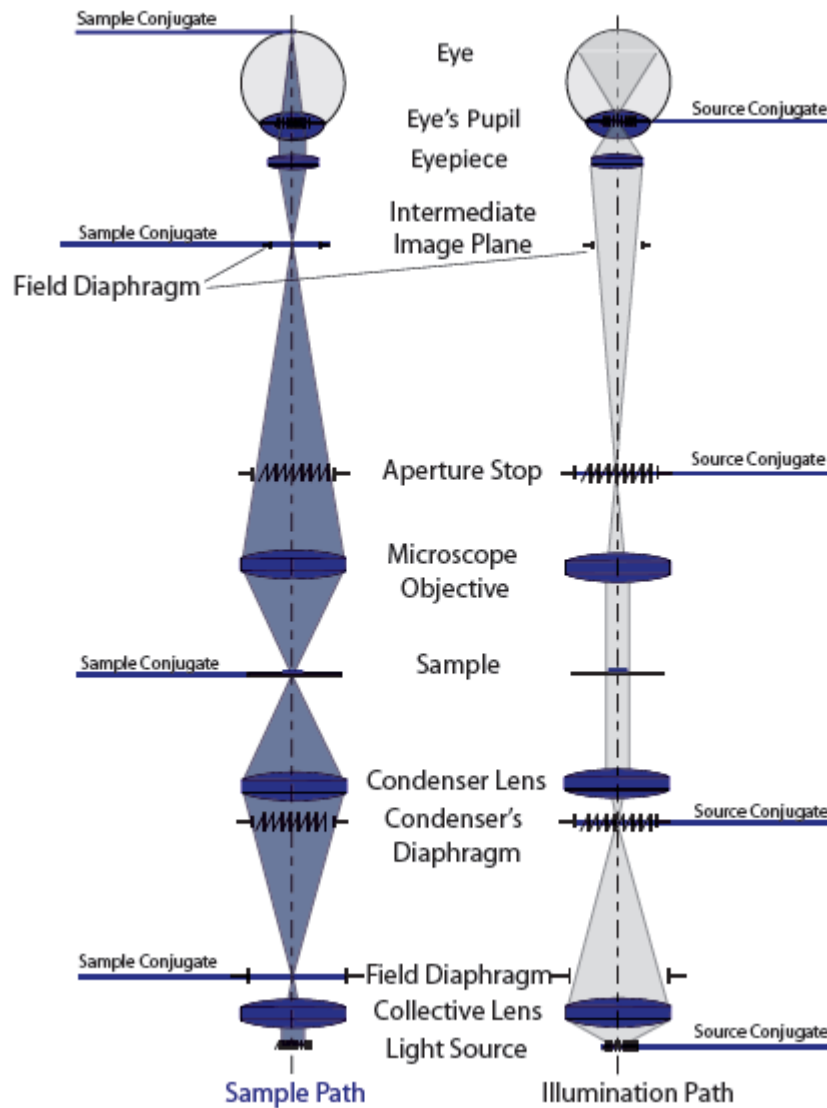


Figure 1.3 Köhler illumination; LHS illustrating the image formation path and the RHS showing the illumination path

Use of a high numerical aperture (NA) collective lens permits the focusing of the light source at the rear focus of a condenser lens. Condenser lenses are typically used to focus light onto the sample, however this is not the role in this form of illumination. As a result of the reciprocal relationship between the image and rear focal plane, light emerging from the condenser is completely out of focus. This results in a uniform illumination at the sample. However, as a result of aberrations in the lenses or non-uniform illumination, this may not be the case for all angles of light convergence.

This situation is addressed by inserting a field diaphragm directly after the collector lens, and an equivalent aperture at the back focus of the objective lens. The collector diaphragm determines the angle of the convergence and hence the realised NA of the system. The out of focus light passes through the sample and the filament is imaged at the rear focal point of the objective and results in no imaging of the light source's filament at the detector, which may be the eye, a camera or another photo-detector.

Despite the success of the system described in Fig. 1.3, it is somewhat limited for use with thick or turbid biological samples. This restricts the practical use of the microscope. Where the light source for excitation and signal collection both propagate through the same lens, known as epi-illumination [3], the microscope becomes useful for imaging of opaque and absorbing samples. This is achieved by inserting a beam-splitter or dichromatic beam splitter in the imaging path. This allows illumination of the sample in the forward direction and the generation of a reflectance or back-scattered image in the reverse direction to the incoming illumination. The full potential of epi-illumination was not realised until such a system was used in conjunction with fluorescence microscopy, which will be described later in this chapter.

1.2 Spatial resolution

As described in Section 1.1, the amount of light which a lens accepts ultimately has a direct effect upon the resolution of the microscope system. The acceptance (and emission) of a lens is characterised by the numerical aperture (NA) [4]:

$$NA = n \sin \theta \quad (1.1)$$

Here, n represents the refractive index of the medium within which the lens is working (usually air, water, oil or glycerol) and θ is the half-angle of the maximum cone of light which may enter the given lens.

As a consequence of diffraction induced by the aperture of a lens, light from the sample is not imaged as a collection of point sources. The light is instead imaged as a central bright disk, surrounded by concentric rings which reduce in intensity. This intensity distribution is known as an Airy disk. The radius r_{min} , of the Airy disk's central ring limits the smallest point to which a beam may be focused and may be described by [4]:

$$r_{min} = \frac{0.61\lambda}{NA} \quad (1.2)$$

Lateral resolution of a system may be expressed in terms of the positioning of two point sources, with diffraction images in the same plane, are separated by a small distance d . If the d is greater or equal to r_{min} , then the points can be resolved. This is known as the Rayleigh criterion.

During the late 19th century Ernst Abbe not only demonstrated that lenses were subject to diffraction but he also quantified the required conditions for a light source to be diffraction limited,

$$d_{\min} = \frac{1.22\lambda}{NA_{obj} + NA_{cond}}. \quad (1.3)$$

Abbe's resolution limit takes into account the role of both the objective lens (NA_{obj}) and the condenser lens (NA_{cond}). This provided a lateral distance between two lines of a periodic grating that could be resolved.

As a result of Eq. (1.2) & (1.3), it can be seen that lateral resolution is directly proportional to the wavelength of the illuminating light and inversely proportional to the NA of both the objective and condenser lenses used.

Using the Airy disk diffraction pattern described for the Rayleigh criterion in three dimensions, axial resolution (which is defined as the minimum distance in the z -direction between which two point sources can be identified) may be described by

$$z_{\min} = \frac{2\lambda n_s}{(NA_{obj})^2}, \quad (1.4)$$

where n_s is the refractive index of the sample.

1.3 Contrast mechanisms

In addition to resolution, contrast plays a pivotal role in determining the overall quality of an image. Following from the introduction of light sources for sample illumination described in Section 1.1, various additional techniques for achieving high contrast have been developed. One of the first of these techniques was developed in 1934 by the Dutch physicist Frits Zernike and is known as phase contrast microscopy [5]. This technique uses a combination of optics to introduce corresponding changes in amplitude, this in turn can be visualised as contrast within a sample. This technique greatly increased contrast for many transparent biological samples. Issues such as the need for samples to be fixed, and its inability to image thick samples required. However the need for further development of additional contrast mechanisms is required.

Techniques to increase contrast range from use of samples which emit frequencies differing from the illumination source, to samples that generate an electric current which can be used for surface mapping. This section provides an overview of the contrast mechanisms used within this thesis.

1.3.1 Fluorescence

The property of fluorescence has been observed for thousands of years, through the naturally occurring fluorescence produced by minerals such as Autunite, Fluorite and Calcite, when observed under certain illumination conditions. The first scientific record of fluorescence was reported by John F.W. Herschel in 1845 [6], when fluorescence was observed from a transparent quinine solution under illumination by sunlight.

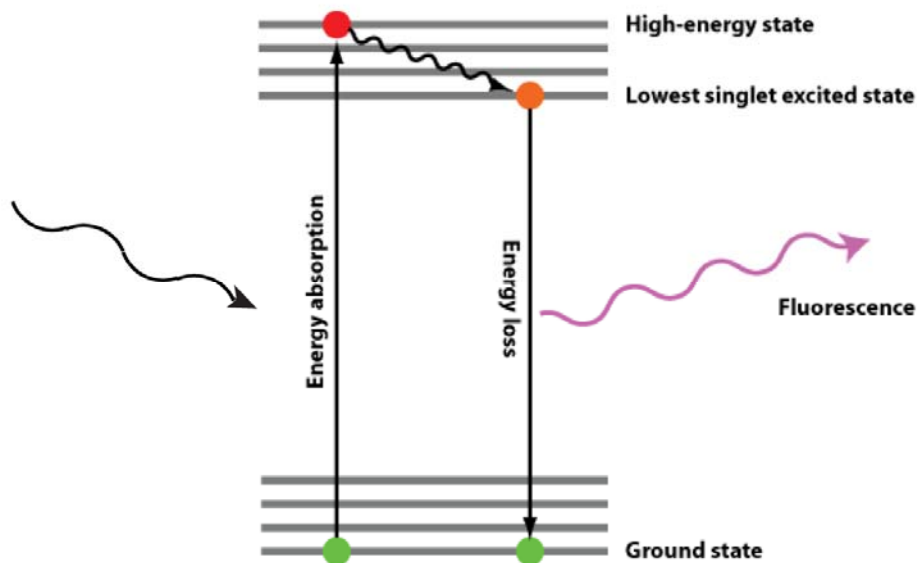


Figure 1.4 Jablonski diagram describing the electronic transitions involved in fluorescence

In 1852, Sir George Stokes was the first to describe the wavelength changing properties of such materials and highlighted the red-shifted emission resulting from this interaction [7]. To understand the mechanism of fluorescence, it is convenient to consider a description of the electronic states of a fluorescent molecule (as represented by the Jablonski diagram in Fig. 1.4).

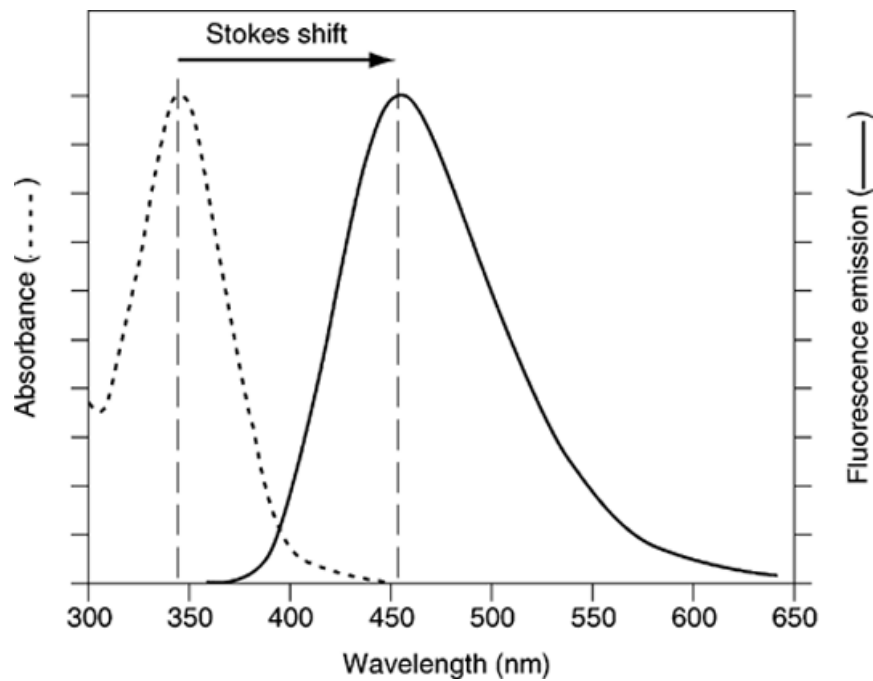


Figure 1.5 The red shifted (Stokes shift) for a standard fluorophore with an absorbance in the UV

Fluorescent molecules permit the transition of an electron from a ground state to an upper energy level (excited state). This is achieved through absorption of the energy from an incident photon with energy equal to the difference in electronic states. The electron then experiences a non-radiative decay to the lowest singlet excited state [4]. Radiative decay to the ground state then results in the emission of a photon with lower energy than that used for excitation as illustrated in Fig 1.5. Since a molecule is at equilibrium when electrons are in the ground state, the excited state is a short-lived event, on the nanosecond scale.

Since its application to microscopy, fluorescence has become a vital imaging tool in the field of life science and materials analysis. As a result of the expansive range of available fluorophores (which can be attached to biological structures using histochemistry), labelling of samples has allowed identification of cells and sub-cellular components which are not visible using alternative contrast techniques [8-10].

Fluorescence microscopy is particularly useful when used in combination with an epi-illumination (epi-fluorescence) geometry, such as that introduced in Section 1.1. Most fluorescent microscopes are configured in an epi-illumination mode, due to the substantially decreased amount of excitation light to which the detector is exposed. Additionally, fluorescence returns through the same path as the excitation beam, therefore the same objective lens (and galvo-mirrors which can be used for laser scanning) may be used, greatly simplifying the system [3].

Application of fluorescence to a microscope requires the addition of three filters to a standard epi-illumination microscope: an excitation filter, emission filter and a dichroic beam splitter. These filters are used in order to separate strong excitation light from the weak fluorescent signal produced by a sample and ensure that only the fluorescence signal reaches the detector.

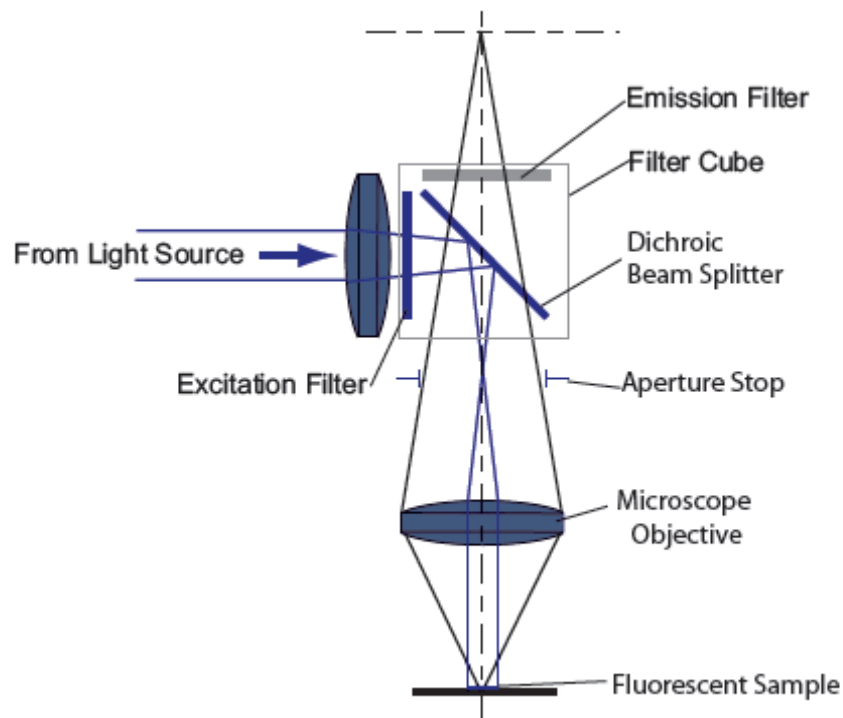


Figure 1.6 Epi-fluorescence microscope

Figure 1.6 shows the configuration of an epi-fluorescent microscope. The excitation filter is required to ensure the correct wavelength of light used for the efficient excitation of the sample. The dichroic beam splitter allows the introduction of the excitation light to the microscope and collection of the fluorescent signal. This is made possible through careful selection of the dichroic beam splitter such that the excitation source is reflected or absorbed and the Stokes shifted fluorescence is transmitted.

When considering illumination of biological samples, attention must be paid to power levels to which the sample is exposed and also the wavelength of light (shorter wavelengths result in higher damage). Phototoxicity is a toxic reaction which is incurred through the application of light to a sample [4]. Unfortunately, complete transfer of energy from a photon to the promotion of an electron to a higher energy level may not occur. Some of this energy may be transferred to oxygen and result in the generation of oxygen radicals. These are toxic to biological samples, often leading to swift cell death.

Despite the many advantages incurred when using an epi-fluorescent microscope, a major drawback is the generation of fluorescence from lateral planes above and below the focal plane, leading to a detrimental contribution from out of focus light to the image, which can conceal details in the focal plane [11]. Figure 1.7 gives an epi-fluorescent bright-field image of a 5 day old quail embryo fixed in formaldehyde and stained with Alexa 488-phalloidin taken from a study by Swedlow et al [12]. Here it can be seen that very little information can be gained from this poor contrast image, as a result of the contribution from the out-of-focus light. From this it is possible to conclude that for a wide range of thin live samples including cell cultures, bacteria, etc, epi-fluorescence imaging is a very useful technique. However with application to tissues thicker than $\sim 5 \mu\text{m}$, poor quality images are generated and alternative forms of imaging are required.

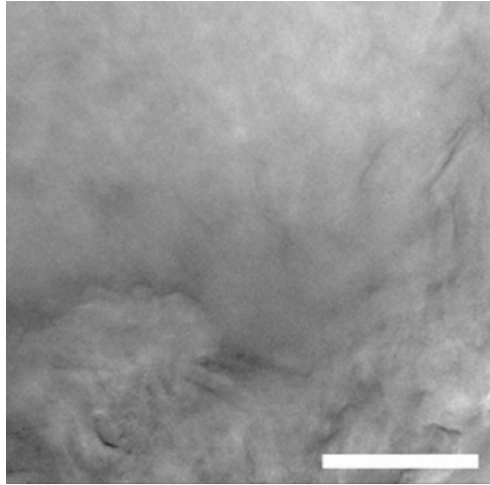


Figure 1.7 Brightfield image of a thick sample (quail embryo), here the scale bar represents 50 μm . [Reproduced from [12]]

1.3.2 Harmonic generation

An alternative method to fluorescence for obtaining a contrast image is through harmonic generation. Such a technique is based upon a nonlinear event induced within a sample; whereby incident light is converted to a frequency at double that of the incident beam. This case is known as second harmonic generation (SHG). The topic of nonlinear optics will be discussed in further detail in Chapter 2. However as a simple description; if two identical low energy photons are considered, under certain conditions they may combine to generate the new frequency. This process may only be achieved when a sample exhibits a non-centrosymmetric molecular structure.

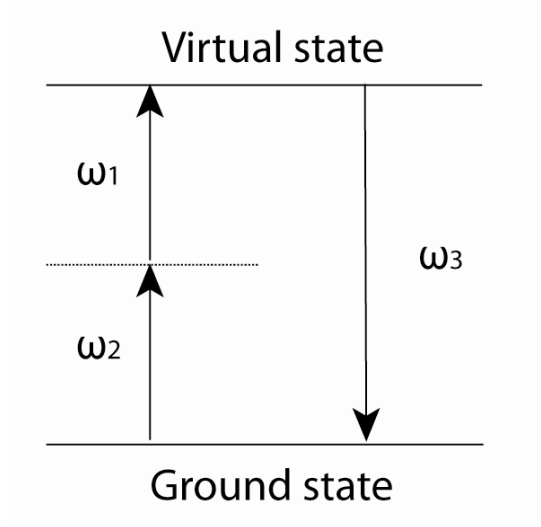


Figure 1.8 Second harmonic generation. Where ω_1 and ω_2 are pump photons with the same frequency and ω_3 is a frequency double that of the pump photons.

Despite the similarity of this process to fluorescence, in that a new frequency is generated as a result of incident light, no absorption of photons takes place and a Stokes shift does not occur. In this case, energy is conserved and the frequencies involved may be represented by the relationship

$$\omega_1 + \omega_2 = \omega_3, \quad (1.5)$$

where, for SHG, incoming photons ω_1 and ω_2 are equal and the resultant frequency ω_3 is double that of ω_1 .

The first report of SHG in microscopy was performed by Hellwarth *et al* in 1974 [13]. This involved the use of a Q-switched YAG laser at 1064 nm, applied to a ZnSe polycrystal for imaging of its physical structure. Since this time, SHG imaging has found a wealth of applications in both material analysis and biological systems.

As a result of the inherent frequency conversion induced by the sample, no exogenous fluorophores need to be used. This is advantageous, as fluorophores may interfere with the behaviour of a biological process. Also, due to the lack of actual excitation of electrons such as that seen in fluorescence samples are not subject to phototoxicity or photobleaching [14].

An additional benefit to using harmonic generation imaging is the longer wavelengths which are used for illumination of the sample. Longer wavelengths are subject to less scatter and therefore deeper penetration of a sample is achievable [9].

Similarly to SHG, a similar nonlinear process may be incurred for three incident photons for frequency conversion, which is known third harmonic generation (THG). This increases the excitation wavelength further; however, greater photon densities are required for such a process.

Despite the advantages of harmonic imaging, the samples which may be used are limited to those which provide a molecular structure suitable for access to its nonlinear susceptibility. This in turn also requires the need for high intensity laser sources which can often be expensive.

1.3.3 Optically induced current

When considering the mechanism for contrast imaging of a particular sample, it is often important to consider alternative methods to standard optical detection methods. For example within material analysis of semi-conductors such as light emitting diodes (LEDs), it is often of interest to evaluate the electronic response of the device.

The mechanism for generation of light from an LED can be described by consideration of the electronic transitions between the p-type and n-type materials within the semi-conductor.

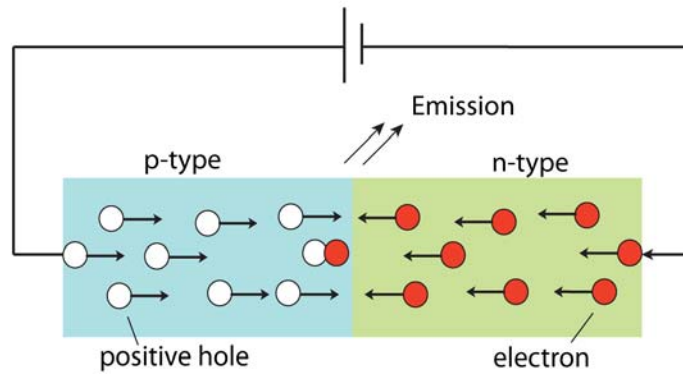


Figure 1.9 Mechanism for photon emission from LED when subjected to a current

When current flows across a diode, electrons and ‘holes’ travel in the opposite direction. At the point where an electron encounters a hole, the electron drops down to a lower energy level, resulting in the emission of a photon, as illustrated in Fig. 1.9. This technique is termed as electroluminescence.

One imaging technique which looks to take advantage of these p-n junction transitions is known as optical beam induced current (OBIC). This is in essence the reverse condition of electroluminescence, whereby incident light is used to generate electron-hole pairs, resulting in an induced current, as illustrated in Fig. 1.10. This current may then be reconstructed to form an electronic map of the active region of a device [15].

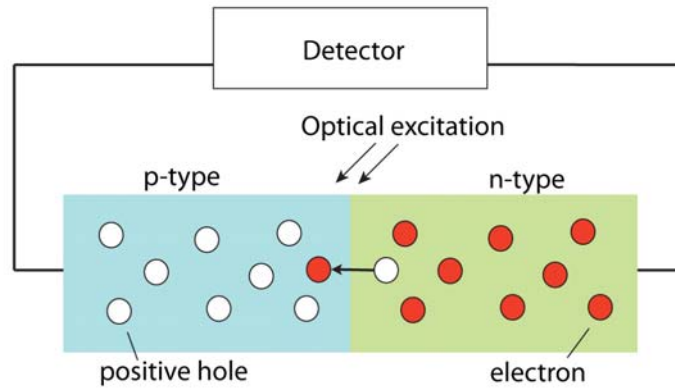


Figure 1.10 Simplified OBIC detection schematic highlighting the p-n transition induced by optical excitation

This technique has been applied in microscopy allowing high resolution imaging with good contrast without incurring damage to devices, with applications including short circuit detection and evaluation of homogeneity.

1.4 Confocal laser scanning microscopy

As described in section 1.3.1, bright-field fluorescence microscopy is a very useful technique for unveiling biological structures which cannot be obtained by other, previously used methods. However, when considering imaging of biological tissue, the technique is severely limited to thin slices. This is a result of the contribution of out of focus fluorescence to an image, when using thick slices. This results in poor contrast images. A technique which aims to address this issue was developed by Minsky [16]. This technique is known as confocal microscopy and implements apertures at the excitation and detection paths. The excitation aperture is used to ensure only one point of interest is imaged. The aperture used in the detection path is used to eliminate out of focus fluorescence. In recent times, this technique for out-of-focus rejection has been implemented for the application of laser excitation sources, as seen in Fig. 1.11. Here it can be seen that only fluorescence generated at the focal plane reaches the detector.

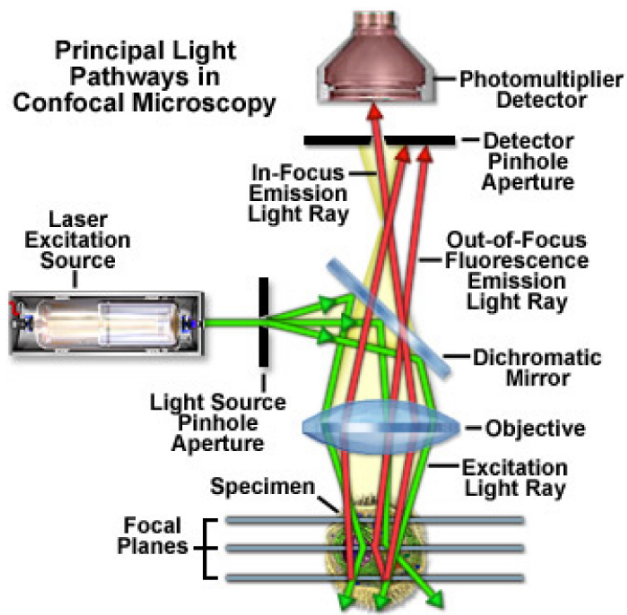


Figure 1.11 Confocal microscopy; fluorescence collection pathway

With the introduction of two galvo-scanning mirrors, the excitation beam may be raster scanned across the sample using laser scanning software. When such a system is used it is known as confocal laser scanning microscopy (CLSM). The detected fluorescence which is generated throughout the scanning region is collected by a detector, typically a photo-multiplier tube (PMT), and then used to generate a contrast image. As the objective lens can be used for focusing of the beam within a sample, and capable of controlled z-translation, this technique can therefore be used for optical sectioning and three dimensional imaging. CLSM therefore offers imaging of samples which is not possible with brightfield fluorescence microscopy [17]. Another great advantage of using this type of imaging is the ability to analyse intact samples non-invasively, allowing for live cell imaging. The minimum average cw power requirement for single photon excitation is typically less than 1 mW [4].

Many of the common fluorophores which are used for biological labelling require excitation in the 320 – 600 nm range [18], along with newer dyes with longer

excitation wavelengths dyes such as mCherry and mPlum [19, 20]. Despite the many advantages achieved through application of CLSM, this technique implements a source, typically continuous wave (cw) laser, with a wavelength corresponding to the peak excitation of the fluorophore. As a result of this, the excitation beam is absorbed throughout the sample resulting in fluorescence at planes other than that of the focal plane (Fig. 1.12).

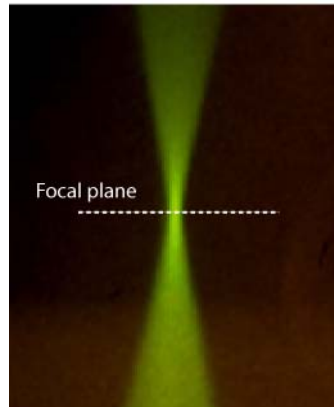


Figure 1.12 Generated fluorescence in single photon excitation throughout a deep sample (reproduced from [21])

Despite the application of the confocal apertures used for isolated detection of the focal plane (illustrated in Fig. 1.11), loss of signal is incurred as a result of this method. Moreover, with prolonged exposure to excitation, fluorescent samples may be subject to photobleaching.

Another issue with CLSM is that the short wavelength sources used for excitation incur greater scattering. This restricts the depth penetration within tissues. Additionally, it has been shown that use of short wavelengths reduces cell viability.

1.5 Multiphoton laser scanning microscopy

A method which was devised to overcome the restrictions of CLSM was pioneered by Denk *et al* [22]. This was based upon the nonlinear absorption of photons by fluorophores and is known as multiphoton laser scanning microscopy (MPLSM).

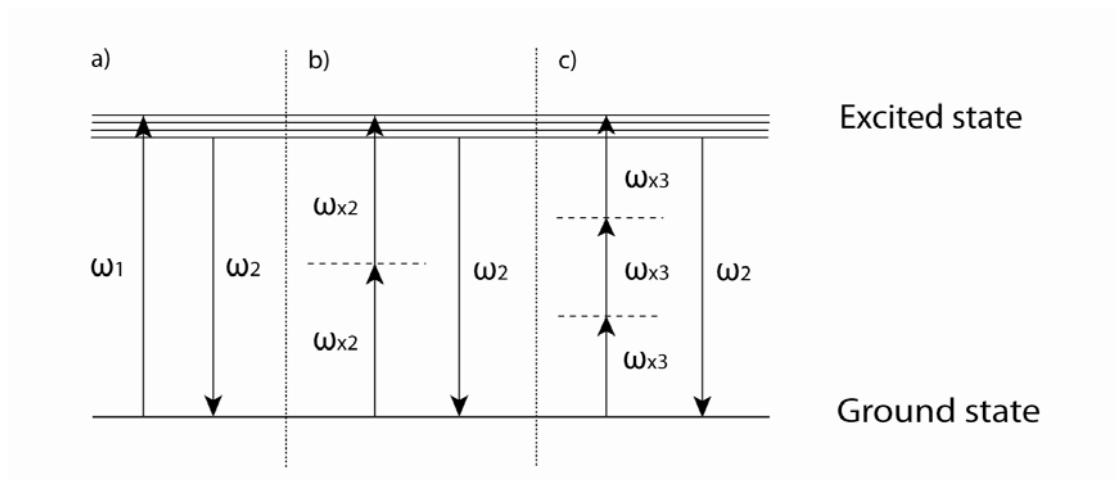


Figure 1.13 Electronic transition states for a) single-photon b) two photon and c) three photon excitation. Virtual states are shown as dashed lines.

Unlike the case of CLSM, which uses a high energy light as the excitation source, E_0 , MPLSM implements a source with energy equal to $E_0/2$. As the fluorescent molecules require certain energy for excitation, using low energy light as an excitation source would not be useful. In 1931, Maria Goeppert-Mayer theoretically described multiphoton excitation in her doctoral thesis [23], however no suitable excitation source was available for this mechanism until the advent of the laser.

The nonlinear absorption of two photons by a fluorescent sample, as illustrated in Fig. 1.13, gives rise to simplest form of MPLSM, as this case places the lowest constraints upon the excitation source. The number of two photon events which occur within a sample can be calculated by using the following equation [4]

$$n = \frac{P^2 \alpha}{\tau (\Delta \nu)^2} \cdot \frac{\pi^2 NA^2}{(hc\lambda)^2} \quad (1.6)$$

where, n = number of two-photon absorption events, P = average power, τ = pulse duration, $\Delta \nu$ = repetition rate. NA = numerical aperture, h = plank's constant, c = speed of light and λ = wavelength.. Therefore, in order to achieve large numbers of two photon absorption events, a high photon density is required.

Since the development of high-power ultra-short pulsed lasers, peak powers in excess of 100 kW are currently available (an overview of laser sources for microscopy will be provided later in this chapter). The beam from such a laser may be tightly focused into a sample to generate a photon density at the focal point which is high enough to allow molecules to absorb two low energy photons simultaneously, resulting in outputs which are sufficient for image formation [22]. As the beam is tightly focused, this results in a highly localised volume of excitation and therefore fluorescence is only stimulated within the focal plane. As a consequence, the laser intensity in the volume surrounding the focal point rapidly decreases, causing a very small number of out-of-focus photons to be generated. Therefore MPLSM provides inherent optical sectioning. This negates the need for the aperture which is used within CLSM, and all signal which is generated may be used for imaging, giving a high signal-to-noise ratio.

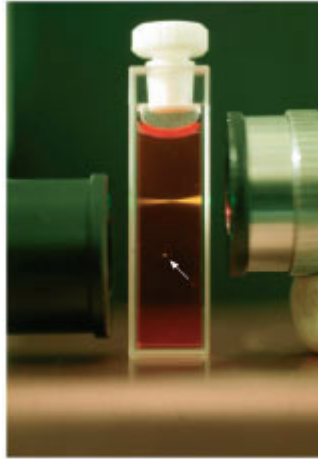


Figure 1.14 CLSM vs. MPLSM: The fluorescent dye (Nile Red) contained within above cuvette is subjected to single photon excitation (from right hand side) and multiphoton excitation (from left hand side). [Courtesy of Dr Brad Amos, MRC]

Figure 1.14 highlights the volume of excitation for both CLSM and MPLSM, when passed through a fluorescent solution. For single photon excitation (produced by the RHS objective), it can be seen that excitation occurs throughout the entire depth of the cuvette. In the multiphoton case (LHS objective), however, only a very small volume of excitation is observed.

One of the other main motivations for using a multiphoton system is due to the increased depth penetration into a sample. The maximum limit for depth penetration into a sample is equal to the working distance of the objective lens. However, in practice this limit is not reached. The fluorescence signal is attenuated as it passes through a sample, and for the single photon case at depth, much of the excitation wavelength will be absorbed by out-of-focus molecules before reaching the focal plane. This effect is much reduced as a result of the longer wavelengths which are used for MPLSM excitation.

Due to the success of the two photon excitation method, researchers have looked to alter this technique in order to observe three photon excitation [24, 25]. Fluorescent

molecules behave in a similar manner regardless of whether they are excited by one, two or three photons. Decreasing the photon excitation energy to approximately one third of that required for single photon absorption, three low energy photons can be simultaneously absorbed. This results in the emission of a photon equal in energy to that of the single photon case. With the ease of implementation to standard multiphoton laser scanning microscopy platforms, the technique has the potential to be implemented throughout a large number of laboratories.

In a study by Debarre et al [26], it was found that cells excited by a longer wavelength had an increased survival rate when compared that of shorter wavelengths. This indicates the benefit of using a longer wavelength source for biological imaging. Despite the promise of three photon microscopy there are very few groups working on this and therefore there is much to be pursued within this field.

As there are advantages to be gained from three photon microscopy, it may raise the question as to whether a four photon excitation may provide further benefits. However when considering the intensities required for two and three photon absorption, they require values on the scale of MW/cm^2 - GW/cm^2 . The required intensity for four (or more) photon absorption is in the range of TW/cm^2 . At such high intensities multiphoton ionisation and plasma formation occurs. Substantial damage to samples is induced as a result of these effects. Therefore, four (or more) photon excitation is not a viable option for biological imaging.

1.6 Light sources for microscopy

As described in Section 1.1, illumination of a sample is critical to the contrast of an image. Therefore consideration must be given to this source. Various factors need to be considered including brightness, wavelength and coherence. This section will

evaluate the usefulness of both incoherent and coherent sources for application within microscopy.

1.6.1 Incoherent sources

The initial light sources used for microscopy were incoherent sources (i.e. no fixed phase relationship between waves). Common types of these sources include incandescent lamps, arc lamps and light emitting diodes (LEDs).

Incandescent lamps (e.g. Halogen lamps) are a common choice for brightfield microscopy due to their continuous spectrum and high brightness. These are also inexpensive and have long operational lifetimes.

Arc lamps (e.g. Mercury arc lamp) often provide brightness in excess of that produced by incandescent lamps, making them particularly useful for brightfield fluorescence microscopy. The broad range of emission of such sources (ultraviolet to infrared), allows for filtering of the source to produce ‘monochromatic’ (depending upon the quality of filter) excitation sources. Despite these benefits, arc lamps are often difficult to align and have operational lifetimes of less than 300 hours.

Light emitting diodes (LEDs) are semi-conductor devices which when subjected to a current, emit light as a result of transitions between the semi-conductors p-n junction. The energy of emitted photons is dependent upon the difference between electronic states within the device. LEDs provide an excellent source of bright illumination and can have operational lifetimes in excess of 50,000 hours [27]. These devices are inexpensive, and due to the wide array of semi-conductor materials available; can cover a wide range of the spectrum. Some of the common high power LED sources used within microscopy are given in Table 1.1.

Wavelength (nm)	Semi-conductor	Approx. average power (mW)
455	InGaN	300
470	InGaN	300
505	InGaN	200
530	InGaN	150
590	AlInGaP	< 25
633	AlInGaP	< 50
435-675	GaN/(Al,Ga)N	200

Table 1.1 Available high power LEDs for application in microscopy

Despite exhibiting lower brightness than arc lamps, LEDs have been successfully applied to fluorescence microscopy.

1.6.2 Coherent sources

The definition of a monochromatic wave is a wave which exhibits a single wavelength λ . However, it is often the case that light sources emit over a finite range of wavelengths $\Delta\lambda$, sometimes referred to as the bandwidth or wave-packet. If the spread of wavelengths has a fixed phase the source is said to be coherent. The average length of such a wave-packet is given by a source's coherence length l_{coh}

$$l_{coh} = \frac{\lambda^2}{\Delta\lambda}. \quad (1.7)$$

The laser is a typical source of coherent light, due to the resonance of the output waves, coherence is ensured. A wide range of gain media and techniques are available to generate laser light, with tailoring of properties including wavelength, pulse duration, repetition rate and others.

1.6.2.1 Lasers in CLSM

The laser is the most suitable source for practical CLSM. For this imaging method the light source requirements are high brightness, high spatial and temporal coherence and monochromaticity, which are all inherent properties of laser sources. Table 1.2 gives a brief list of the various common lasers available for use in practical CLSM, along with their output wavelengths.

Laser	Useful output wavelengths (nm)
Argon ion	351, 488, 514
Krypton-Argon	488, 568, 647
Helium-Neon	543, 594, 612, 633
Diode lasers	405, 440, 488, 630

Table 1.2 Common laser sources in CLSM

As CLSM requires single photon excitation, lasers which operate in continuous wave (cw) mode are required. Additionally, the listed laser sources tend to have limited output power. However, this tends not to be a restriction for CLSM where

fluorescence excitation is possible with sub-milliwatt levels of average power. These sources are also relatively inexpensive.

1.6.2.2 Lasers in MPLSM

As mentioned in section 1.5, MPLSM requires high photon densities at the focal plane. This is made possible using mode-locked laser sources that provide ultra-short pulsed output. A brief review of mode-locking is presented before providing further detail on laser sources commonly used in MPLSM.

1.6.2.2.1 Mode-locking

It is often the case that lasers produce an output which covers a range of frequencies. This is determined by a combination of two main factors.

The first of these is a property of the gain medium which is contained within the laser cavity. The gain bandwidth of a medium is the range of frequencies over which a laser can operate. When selecting a gain medium it is very important to select a crystal which has a gain bandwidth suitable for the application.

The second factor which is important for determining the output frequencies of a laser is the design of the resonant cavity. By using reflective mirrors to build a cavity around a gain medium, light waves are reflected back upon themselves, producing standing waves as a result of constructive and destructive interference. Where interference is constructive, these frequencies are termed as longitudinal modes and are the only frequencies which can be supported within the laser cavity. Together

with the gain bandwidth mentioned previously, the laser resonator design therefore determines the number of these longitudinal modes which may be supported.

In the case of a cw laser, all of the longitudinal modes contained within the gain bandwidth will all operate simultaneously and have no fixed phase relationship. This leads to interference; as the phases of these will be somewhat random they will give rise to an almost constant average power output.

Instead of allowing each of the supported modes within a cavity to operate individually, a fixed the phase relationship between modes can produce periodic interference which can generate an output of short pulses with high intensity. By using methods to fix the phase relationship, modes become phase “locked”. In practical optics, this is known as mode-locking. The pulse train is produced with interval between pulses t_r , which is determined by the cavity round trip time

$$t_r = \frac{2L}{c}, \quad (1.8)$$

where L is the length of laser cavity.

Given that the central frequency produced by the gain bandwidth is ω_0 , with $\pm m$ additional modes. The resulting electric field produced in multimode oscillation can be described at each point using the following equation;

$$E(t) = \sum_{n=-m}^m E_n \exp \left[i \left(\omega_0 + n \frac{2\pi}{t_r} \right) t + \varphi_n \right], \quad (1.9)$$

where E_n and φ_n describe the electric field amplitude and phase for the n th mode. In the case for mode-locking, all phases are locked therefore the phase dependence $\varphi_n = 0$. By determining the product of the sum of Eq. (1.9) for a finite series and its complex conjugate $E^*(t)$, it is possible to obtain an equivalent value for intensity when N modes circulate;

$$I(t) = E(t)E^*(t) = E_0^2 \frac{\sin^2(N\pi t / t_r)}{\sin^2(\pi t / t_r)}. \quad (1.10)$$

By determining when the value of t for which the numerator in Eq. (1.10) becomes zero, i.e. at $t = t_r / N$, this can be used as an approximate value for the FWHM of the pulse duration t_p

$$t_p \approx \frac{t_r}{N} \approx \frac{1}{\Delta\nu}. \quad (1.11)$$

This, in turn, is approximately the reciprocal of the gain bandwidth $\Delta\nu$. This equation highlights Fourier's theorem, which describes the need for large gain bandwidths in order to obtain short pulses.

Techniques for mode-locking are classified as active or passive. A brief synopsis of these methods is presented. A full treatment is provided by Siegman [33].

1.6.2.2.2 Active mode-locking

One technique which is commonly applied for mode-locking involves the introduction of an element into the laser cavity which has controlled losses; this is known as active mode-locking.

Active mode locking typically involves the use of an amplitude modulator such as an acousto-optic modulator (AOM) or an electro-optic modulator (EOM). If the modulating element is synchronised to the round-trip time of the resonator, this can lead to the formation of pulses.

By firstly looking at what effect this has in the frequency domain, it is seen that each longitudinal mode acquires sidebands due to the modulating loss of the acousto-optic element. By inducing a modulation of frequency ν_m , to a mode of frequency ν_0 , the mode will acquire sidebands at $\pm \nu_m$. If this modulating frequency is equal to the frequency mode separation $\nu_m = c/2L$ the sidebands overlap and couple with longitudinal modes $\nu_0 + \nu_m$ and $\nu_0 - \nu_m$. As these two new coupled modes pass through the modulator, they also experience the same process and produce sidebands at $\nu_0 \pm 2\nu_m$. This continues until all stable modes within the gain bandwidth lock in phase.

By now considering what this type of mode locking means in the time domain, the modulation of the loss-inducing element causes the laser to oscillate pulses around the cavity. Upon each round trip time, the pulse passes through the element when losses are at a minimum. However, despite the main section of the pulse experiencing minimum losses, the wings of the pulse will be slightly attenuated. This attenuation leads to a slight shortening of the pulse. Upon each round trip, the pulse decreases in duration and results in the broadening of the spectral bandwidth. When the spectral bandwidth approaches the gain bandwidth of the crystal, the gain will no longer increase.

An alternative form of active mode-locking which uses a gain medium pumped by a pulsed laser as a tool to generate pulses at an alternative frequency, is known as synchronous pumping. This technique is widely used throughout nonlinear optics as it can be used to produce ultra-short pulsed outputs.

Unlike the alternative methods, the pump source for a synchronously pumped system is already a pulsed source. A resonator can be described as synchronously pumped in the condition where the cavity round trip time matches that of the pump source. When this condition is met, the gain medium within the resonator is only active for the time that the pump pulse is to present; therefore the output from the resonator tends to mimic the duration of these pulses.

In active mode-locking, a serious limitation to the shortening of a pulse is the dependence of the technique on the electrical signal produced by the generator controlling the modulator. However if the pulse itself can be used to modulate the absorption element, much shorter output pulses may be achieved.

1.6.2.2.3 Passive Mode-locking

An alternative to active mode-locking which does not require a modulating element is known as passive mode-locking. This method uses a passive element known as a saturable absorber (SA), which is inserted into the laser cavity in order to fix the phase relationship between cavity modes. The useful attribute of a SA for mode locking is its ability to absorb low intensity light yet transmit light of high intensity, thus responding as a nonlinear mirror.

Upon entering the gain medium, the oscillating light generates noise. Within this noise, fluctuations occur which result in a single predominant spike being formed. As

a result of the nonlinear properties of a saturable absorber, the spike experiences less loss upon each round trip pass than other noise within the system. As a result, this peak will increase much faster than any other of the random peaks until it reaches the intensity required to be transmitted through the SA. As the light continues to oscillate, the process repeats and generates a train of pulses and hence the laser will be mode-locked.

1.6.2.2.4 Ultra-short pulsed lasers in MPLSM

With the discovery of mode-locking techniques, lasers have been produced with high average power and pulse durations of less than 100 fs. This generates peak powers greatly in excess of lasers operating in cw mode.

Ultra-short pulsed laser	Wavelength coverage (nm)	Pulse duration (fs)	Average power (W)
Ti:Sapphire	690 – 1050	< 100	>1
Cr:Forsterite	1230 – 1270	< 65	0.3
Optical parametric oscillator (OPO)	UV – mid-IR	< 100	0.5

Table 1.3 List of the most commonly used tunable fs-pulsed lasers for MPLSM

Wavelength tuning of a laser source is also a highly desirable feature for an excitation source due to the efficiency requirement of fluorophores to be excited at the peak absorption wavelength.

The Ti:Sapphire laser is the perhaps most commonly used ultra-short pulsed laser for application in MPLSM [10, 28, 29]. The reason for this is due to the broad gain

bandwidth provided by the Ti:Sapphire crystal, permitting a wide range of tuning, high output power and pulses below 100 fs. The wavelength coverage of the Ti:Sapphire also strongly corresponds to the excitation wavelength range of many of the commonly used fluorophores.

The Cr:forsterite laser provides ultra-short pulse durations at wavelengths beyond the capabilities of the Ti:Sapphire laser (see table 1.3) [30]. Despite the limited tuning and output power exhibited by the laser, it has also found application in both two photon and three photon microscopy [30, 31]. Despite costing less than a Ti:Sapphire laser, Cr:Forsterite sources also remain very expensive.

Optical parametric oscillators (OPO) offer an alternative to the traditional laser gain media. These useful devices take advantage of parametric conversion (explained further in Chapter 4) to create a source which is tunable over an entire optical octave. With moderate output powers and ultra-short pulses, OPOs are an extremely flexible multiphoton excitation source [32]. However, these tend to be optically pumped by Ti:Sapphire lasers and therefore incur a price which is beyond the budget of many biological labs.

1.7 Motivation

As shown in Table 1.2, the range of lasers available for CLSM is restricted to sources with discrete output wavelengths. However, for flexibility, wavelength tunability is desirable for excitation of the widest possible range of fluorophores.

Similarly, although the most common laser source for MPLSM is the wavelength tunable Ti:Sapphire, the tuning range is still limited and two photon and three photon excitation of all fluorophores is currently not possible using this technology.

The motivation of this thesis was to develop more efficient and improved optical excitation sources for applications in CLSM and MPLSM. The emphasis of this research was on extending the wavelength coverage of existing laser sources using nonlinear optical methods to facilitate new opportunities in microscopy. This was achieved by employing innovative methods to increase the conversion efficiency of nonlinear optical processes, to create new useful laser sources for MPLSM that are complementary to the ubiquitous Ti:Sapphire, and the use of CLSM and MPLSM to analyse components used within optical imaging.

Chapter 2 is an overview of theoretical nonlinear optical principles that are employed experimentally in subsequent chapters.

Chapter 3 brings together CLSM and MPLSM methods to perform quantitative and qualitative structural analysis of periodically poled nonlinear materials of the type used in Chapters 4 and 5. Determination of the quality of crystal structure via non-destructive methods prior to application for nonlinear optical frequency conversion experiments is useful to visualise crystal defects which may affect material performance and hence contribute to changes in conversion efficiency.

Chapters 4 and 5 describe the development of improved ultra-short pulsed laser sources for MPLSM. This includes the requirement of the source to be tunable and provide sufficient power for application to commercial microscope platforms, which incur substantial loss. Specifically, Chapter 4 involves the development of an increased efficiency synchronously pumped optical parametric oscillator by virtue of a novel pump geometry. Chapter 5 reports the design, development and application of an ultra-short pulsed wavelength tunable sub-700nm source. This system, with wavelengths shorter than the conventional Ti:Sapphire laser, is particularly useful for

samples which are excitable in the UV. Direct comparison to the Ti:Sapphire laser was also conducted.

Finally, Chapter 6 reports the use of a different nonlinear optical system, namely supercontinuum generation, as the excitation source for optical beam induced microscopy of InGaN light-emitting diodes. This non-destructive method enables mapping of active region to perform a quantitative assessment of homogeneity and identify structural imperfections that can compromise device performance.

1.8 References

1. Hooke, R., *Micrographia, or, Some physiological descriptions of minute bodies made by magnifying glasses, with observations and inquiries thereupon: by Robert Hooke; with a preface by RT Gunther*. 2003: Dover Pubns.
2. Pawley, J., *Handbook of biological confocal microscopy*. 1995: Plenum Press.
3. Tkaczyk, T.S., *Field Guide to Microscopy*. 2010: SPIE.
4. Pawley, J., *Handbook of biological confocal microscopy*. 1995: Plenum Press.
5. Masters, B.R., *Confocal microscopy and multiphoton excitation microscopy: the genesis of live cell imaging*. 2006: SPIE Press.
6. Kim, B.C., J.H. Jeong, D.S. Jeong, E.Y. Choi, J.H. Kim and K.B. Nahm. *Simplified laser fluorescence scanner for proteomics studies and early cancer diagnosis*. 2002.
7. Behlke M.A., L. Huang, L. Bogh, S. Rose and E.J. Devor, *Fluorescence and fluorescence applications*. Integrated DNA Technologies, 2005: p. 1
8. Giloh, H. and J.W. Sedat, *Fluorescence microscopy: reduced photobleaching of rhodamine and fluorescein protein conjugates by n-propyl gallate*. Science, 1982. **217**(4566): p. 1252.
9. Denk, W., J.H. Strickler, and W.W. Webb, *Two-photon laser scanning fluorescence microscopy*. Science, 1990. **248**(4951): p. 73.

10. Xu, C., W. Zipfel, J.B. Shear, R.M. Williams, and W.W. Webb., *Multiphoton fluorescence excitation: new spectral windows for biological nonlinear microscopy*. Proceedings of the National Academy of Sciences of the United States of America, 1996. **93**(20): p. 10763.
11. White, J., W. Amos, and M. Fordham, *An evaluation of confocal versus conventional imaging of biological structures by fluorescence light microscopy*. The Journal of Cell Biology, 1987. **105**(1): p. 41.
12. Swedlow, J.R., K. Hu, P.D. Andrews, D.S. Roos, and J.M. Murray, *Measuring tubulin content in Toxoplasma gondii: a comparison of laser-scanning confocal and wide-field fluorescence microscopy*. Proceedings of the National Academy of Sciences of the United States of America, 2002. **99**(4): p. 2014.
13. Hellwarth, R. and P. Christensen, *Nonlinear optical microscopic examination of structure in polycrystalline ZnSe*. Optics Communications, 1974. **12**(3): p. 318.
14. Campagnola, P.J. and L.M. Loew, *Second-harmonic imaging microscopy for visualizing biomolecular arrays in cells, tissues and organisms*. Nature biotechnology, 2003. **21**(11): p. 1356.
15. Ramsay, E. and D. Reid, *Investigation of the two-photon optical beam induced current effect in silicon integrated circuits*. Optics Communications, 2003. **221**(4-6): p. 427.
16. Minsky, M., *MINSKY*. 1961, Google Patents.
17. Webb, R.H., *Confocal optical microscopy*. Reports on Progress in Physics, 1996. **59**: p. 427.
18. C. Dunsby, P.M.P. Lanigan, J. McGinty, D.S. Elson, J. Requejo-Isidro, I. Munro, N. Galletly, F. McCann, B. Treanor, B. Onfelt, D.M. Davis, M.A.A. Neil and P.M.W. French, *An electronically tunable ultrafast laser source applied to fluorescence imaging and fluorescence lifetime imaging microscopy*. Journal of Physics D: Applied Physics, 2004. **37**: p. 3296.
19. Shcherbo, D., E.M. Merzlyak, T.V. Chepurnykh, A.F. Fradkov, G.V. Ermakova, E.A. Solovieva, K.A. Lukyanov, E.A. Bogdanova, A.G. Zaraisky, S. Lukyanov and D.M. Chudakov, *Bright far-red fluorescent protein for whole-body imaging*. Nature Methods, 2007. **4**(9): p. 741.

20. Shaner N.C., Campbell R.E., Steinbach P.A., Giepmans B.N., Palmer A.E. and Tsien R.Y., *Improved monomeric red, orange and yellow fluorescent proteins derived from Discosoma sp. red fluorescent protein*. Nature biotechnology, 2004. **22**(12): p. 1567.
21. <http://www.fmhs.auckland.ac.nz/sms/physiology/biophysics/techniques.aspx>. (viewed 21-03-2011)
22. Denk, W., J. Strickler, and W. Webb, *Two-photon laser scanning fluorescence microscopy*. Science, 1990. **248**(4951): p. 73.
23. Göppert Mayer, M., *Über elementarakte mit zwei quantensprüngen*. Annalen der Physik, 1931. **401**(3): p. 273.
24. Wokosin, D.L., V.E. Centonze, S. Crittenden and J. White, *Three-photon excitation fluorescence imaging of biological specimens using an all-solid-state laser*. Bioimaging, 1996. **4**(3): p. 208.
25. Hell, S.W., K. Bahlmann, M. Schrader, A. Soini, H. Malak, I. Gryczynski, and J.R. Lakowicz, *Three-photon excitation in fluorescence microscopy*. Journal of Biomedical Optics, 1996. **1**(1): p. 71.
26. Débarre, D., W. Supatto, A-M. Pena, A. Fabre, T. Tordjmann, L. Combettes, M.-C. Schanne-Klein and E. Beaurepaire, *Imaging lipid bodies in cells and tissues using third-harmonic generation microscopy*. Nature Methods, 2005. **3**(1): p. 47.
27. Anthony, R., A.H. Kolk, S. Kuijper and P.R. Klatser., *Light emitting diodes for auramine O fluorescence microscopic screening of Mycobacterium tuberculosis [Technical Note]*. The International Journal of Tuberculosis and Lung Disease, 2006. **10**(9): p. 1060.
28. Helmchen, F. and W. Denk, *Deep tissue two-photon microscopy*. Nature Methods, 2005. **2**(12): p. 932.
29. Zipfel, W.R., R.M. Williams, and W.W. Webb, *Nonlinear magic: multiphoton microscopy in the biosciences*. Nature biotechnology, 2003. **21**(11): p. 1369.
30. Chen, I.H., S.-W. Chu, C.-K. Sun, P.-C. Cheng and B.-L. Lin, *Wavelength dependent damage in biological multi-photon confocal microscopy: a micro-spectroscopic comparison between femtosecond Ti: sapphire and Cr: forsterite laser sources*. Optical and quantum electronics, 2002. **34**(12): p. 1251.

31. Liu, T.M., S-W. Chu, C-K. Sun, B-L. Lin, P-C, *Multiphoton confocal microscopy using a femtosecond Cr: forsterite laser*. Scanning, 2001. **23**(4): p. 249.
32. Myers, L.E., R.C. Eckardt, M.M. Fejer, R.L. Byer, W.R. Bosenberg, and J.W. Pierce., *Quasi-phase-matched optical parametric oscillators in bulk periodically poled LiNbO₃*. Journal of the Optical Society of. America. B, 1995. **12**(11): p. 2102.
33. Siegman, A. E., Lasers, 1986: University Science Books

Chapter 2 Theory of nonlinear optical frequency conversion

2.1 Introduction

Nonlinear optics is the collective term for the nonlinear response of a material when exposed to a large electro-optic field, and its ability to manipulate the optical properties of the incident beam. A major step forward in this field was the first experimental demonstration of a laser, which was performed in 1960 by Maiman [1], who generated stimulated emission from a ruby crystal. The coherence of the source was exploited by Franken *et al* [2], who focused a Ruby laser (694 nm) into a quartz crystal and observed an output at exactly twice the frequency of the input beam. This demonstration of nonlinear optical frequency conversion has paved the way for experimental nonlinear optics, and the generation of innovative laser sources.

Wavelengths generated by classical laser sources are restricted by the molecular structure of their gain medium, which is often restricted to infrared emission. However, through exploitation of higher order polarisations of a nonlinear optical material (which are prominent at high intensities), existing lasers may be converted to wavelengths from the deep ultraviolet to the far-infrared. This can be achieved through various nonlinear techniques including; sum frequency mixing (SFM), optical parametric oscillation (OPO) and supercontinuum generation (SC). These techniques can also offer a wide range of tuning as a result of either manipulation of phase matching conditions or from second and third order nonlinear optical processes.

Within the field of life sciences, flexibility of laser sources is vital for many applications. Fluorescence microscopy is a commonly used tool for many biologists, which involves labelling of samples with a fluorescent dye. These ‘fluorophores’ can have excitation bandwidths of < 50 nm [3]. Therefore, if a wavelength far from the

peak excitation wavelength is used, inefficient excitation will lead to unnecessary exposure to radiation which may damage the sample.

This chapter presents an overview of the basic theory for general nonlinear optics and provides a discussion of material selection and a description of the limiting factors for efficient frequency conversion. Following from this, a discussion of the generation and advantages of supercontinuum sources are given.

2.2 Elementary principles in nonlinear optical frequency conversion in bulk media

Conventional linear optics provides the model for the response of materials to optical fields of moderate intensity. To gain a perspective of the mechanisms involved in linear optics, a description of the interaction of light with dielectric materials is given. Dielectric materials can be thought of as ions with a positive core, surrounded by clouds of electrons [4]. Under no external driving force, the net polarisation of a nonlinear material is zero. When an electro-magnetic wave is propagated through such a material, a force is exerted upon the electrons. This force produces a displacement from their equilibrium position, resulting in an electric polarisation within the material. As the field propagates, the resultant force upon the electrons induces an oscillating polarisation at a frequency equal to that of the input field (assuming a weak input beam). The electric polarisation created is therefore directly proportional to the input field, and is described by:

$$\mathbf{P}(t) = \epsilon\chi^{(1)} \mathbf{E}(t) \quad (2.1)$$

where \mathbf{P} and \mathbf{E} are the polarization and electric fields respectively, $\chi^{(1)}$ is the constant of proportionality known as the linear susceptibility and ε is the permittivity of the medium.

When subjected to a strong electric field, such as that produced by a focused laser beam, the polarisation of a dielectric material can no longer be described in linear terms as described in Eq. (2.1). Higher order polarisation terms must therefore be taken into account when describing the oscillation of electron clouds with regards to their respective positive ion core [5]. Equation (2.1) can therefore be expressed as

$$\mathbf{P}(t) = \varepsilon\chi^{(1)} \mathbf{E}(t) + \varepsilon(\chi^{(2)} \mathbf{E}^2(t) + \chi^{(3)} \mathbf{E}^3(t) + \dots) \quad (2.2)$$

where $\chi^{(2)}$ and $\chi^{(3)}$ are the second- and third-order nonlinear susceptibilities of the medium. The first term in Eq. (2.2) represents the linear properties of an optical material (i.e. refractive index, absorption and dispersion). The second term is the contributing factor for processes such as second harmonic generation (SHG), sum- and difference- frequency mixing (SFM and DFM) and parametric fluorescence. It is noted that $\chi^{(2)}$ is zero for materials without a centre of inversion, therefore only asymmetric materials are suitable for such processes. Finally, the third term describes effects such as third harmonic generation (THG) and the Kerr effect. The Kerr effect is the result of a change in the refractive index of a medium resulting from the application of an intense electromagnetic field.

This chapter gives a brief overview of the theory of the nonlinear optical processes involved in the experimental chapters to follow (Chapters 3-6). This includes stimulation of parametric fluorescence for use in an OPO and SFM of two laser sources. Both of these processes involve three interacting beams within a nonlinear medium. In order to describe this interaction between each of these beams and the

generation of new frequencies, one must consider Maxwell's equation for an electromagnetic wave [6]

$$\nabla^2 E + \mu_0 \varepsilon \frac{\partial^2 E}{\partial t^2} = -\mu_0 \frac{\partial^2 P_{NL}}{\partial t^2} \quad (2.3)$$

For three interacting beams, ω_1 , ω_2 and ω_3 within a lossless, nonlinear dielectric medium, Eq. (2.3) provides the platform for the solutions to the coupled wave equations [7]:

$$\begin{aligned} \frac{\partial E_1}{\partial z} &= -i\omega_1 \sqrt{\frac{\mu_0}{\varepsilon}} d_{eff} E_3 E_2^* e^{-i\Delta kz} \\ \frac{\partial E_2}{\partial z} &= -i\omega_2 \sqrt{\frac{\mu_0}{\varepsilon}} d_{eff} E_1^* E_3 e^{-i\Delta kz} \\ \frac{\partial E_3}{\partial z} &= -i\omega_3 \sqrt{\frac{\mu_0}{\varepsilon}} d_{eff} E_1 E_2 e^{-i\Delta kz} \end{aligned} \quad (2.4)$$

where Δk is the phase mis-match and the solutions for these can be solved by integration over the effective interaction length of the beams with the nonlinear crystal.

2.3 Sellmeier equation and dispersion

When an electromagnetic wave propagates through a dielectric medium, the response of the medium is a function of the frequency of the wave. This effect is known as material dispersion and is demonstrated through the frequency dependence of

refractive index, $n(\omega)$. This occurs as result of the resonance frequencies through which a medium absorbs the wave through the bound electron within the material.

As the nonlinear processes described within this thesis involve at least three interacting waves at differing wavelengths, to understand why chromatic dispersion creates a problem, a relationship describing the linear dependence of refractive index upon wavelength λ is required. This is can be shown by analysis of the Sellmeier equation

$$n^2 = a_1 + b_1 f + \frac{a_2 + b_2 f}{\lambda^2 - (a_3 + b_3 f)^2} + \frac{a_4 + b_4 f}{\lambda^2 - a_5^2} - a_6 \lambda^2, \quad (2.5)$$

where n describes the refractive index. In the case of the nonlinear material used throughout this thesis, lithium niobate, a_{1-6} and b_{1-4} are parameters which have been previously measured [8] and can be found in Table 1. The variable f relates to the temperature dependence, where $f = (T-24.5^\circ\text{C})(T+570.82)$ for lithium niobate. This particular expression for the Sellmeier equation is particularly useful due to this temperature dependence, as varying crystal temperature is a key method for wavelength tuning within nonlinear processes. The parameters used in Eq. (2.5) are described in a paper by Jundt [8].

Parameter	Value
a_1	5.35583
a_2	0.100473
a_3	0.20692
a_4	100
a_5	11.34927

a_6	1.5334×10^{-2}
b_1	4.629×10^{-7}
b_2	3.862×10^{-8}
b_3	-0.89×10^{-8}
b_4	2.657×10^{-5}

Table 2.1 Sellmeier coefficients for lithium niobate

This enables simple calculation of both the ordinary and extraordinary refractive indices for lithium niobate. This is discussed in more detail in Section 2.4.1.

As a result of the frequency dependence upon refractive index, the velocity of an incoming wave is described by

$$v = \frac{c}{n(\omega)}. \quad (2.6)$$

For an optical pulse travelling through a material, each of its spectral components will travel at differing velocities. When considering the nonlinear regime, material dispersion can lead to significant changes in the nonlinear response [9]. The effects of material dispersion can be quantified by expanding the mode propagation in a Taylor series for a pulse with a central frequency of ω_0 :

$$\beta(\omega) = n(\omega) \frac{\omega}{c} = \beta_0 + \beta_1(\omega - \omega_0) + \frac{1}{2} \beta_2(\omega - \omega_0)^2 + \dots \quad (2.7)$$

The parameters β_1 and β_2 are related to the refractive index by taking the first and second derivatives of Eq. (2.7).

$$\beta_1 = \frac{1}{v_g} = \frac{n_g}{c} = \frac{1}{c} \left(n + \omega \frac{dn}{d\omega} \right), \quad \beta_2 = \frac{1}{c} \left(2 \frac{dn}{d\omega} + \omega \frac{d^2n}{d\omega^2} \right) \quad (2.8)$$

where n_g and v_g represent the group index and group velocity respectively. The envelope of a pulse travels at this group velocity and the β_2 parameter represents the dispersion of the group velocity (GVD) and is the GVD parameter. When this parameter becomes equal to zero, it is referred to as the zero dispersion wavelength (ZDW). At this point a higher order dispersion term β_3 influences the nonlinear response of a material.

2.4 Anisotropy

Standard transparent materials such as glass tend to exhibit isotropic behaviour (i.e. they respond uniformly, regardless of the direction of propagation). However, the crystalline materials used within nonlinear optics exhibit the behaviour of anisotropy. This is a result of the dependence of molecular structure experienced upon direction of beam propagation through the crystal. A consequence of this property is the dependence of an anisotropic material's refractive index not only upon direction of propagation, but also orientation of polarisation, and therefore the phase velocities of incident waves are also determined by these factors. Within nonlinear optics, crystals which exhibit anisotropy are said to be birefringent.

2.4.1 Uniaxial and biaxial crystals

When considering the propagation of a wave through a nonlinear crystal, it is conventional to describe the polarisation of the beam in the following terms. If a beam is polarised perpendicular to the optic axis, it is termed as an ordinary ray. Conversely, if it is polarised parallel to the optic axis, it is termed as the extraordinary beam. Each polarisation will experience refractive indices of n_o and n_e respectively. The optic axis of a nonlinear crystal is defined as the propagation direction which the velocities of the ordinary and extraordinary polarisations travel are equal. The difference between the refractive indices n_o and n_e is known as the refractive index of a material. The extraordinary refractive index is dependent upon the input angle of the wave such that

$$n_e(\theta) = n_o \sqrt{\frac{1 + \tan^2(\theta)}{1 + \left(\frac{n_o}{n_e}\right)^2 \tan^2(\theta)}} \quad (2.9)$$

Nonlinear crystals fall into two main categories, namely uniaxial and biaxial. Uniaxial crystals have a single axis of symmetry, i.e. the optic axis. Biaxial crystals not only have different refractive indices in the ordinary and extraordinary directions, they also have a dependence upon the direction of propagation. This additional consideration leads to more complexity when analysing biaxial materials for practical nonlinear optical frequency conversion. Throughout the work presented in this thesis, uniaxial crystals are used.

2.5 Nonlinear d coefficient

When analyzing nonlinear optical susceptibilities, it is important to describe their behaviour in three dimensions. If a crystal is non-centrosymmetric, i.e. does not have

a centre of inversion, a tensor notation can be used to describe the three dimensional susceptibility, d in relation to $\chi^{(2)}$

$$d_{ijk} = \frac{1}{2} \chi_{ijk}^{(2)} \quad (2.10)$$

where i, j and k describe the dimensions of the tensor. For simpler analysis, it can be assumed a plane wave approximation that the indices j and k are symmetric. Table 2.2 explains how d_{ijk} may be simplified to the term d_{il} .

Orientation	XX	YY	ZZ	YZ=ZY	XZ=ZX	XY=YX
$l =$	1	2	3	4	5	6

Table 2.2 Terms for simplification of the three dimensional tensor to two dimensions

Using this contracted notation, it is possible to express the relation between the Cartesian components of the polarisation and applied electric fields may be described in the following matrix form

$$\begin{bmatrix} P_x \\ P_y \\ P_z \end{bmatrix} = \begin{bmatrix} d_{11} & d_{12} & d_{13} & d_{14} & d_{15} & d_{16} \\ d_{21} & d_{22} & d_{23} & d_{24} & d_{25} & d_{26} \\ d_{31} & d_{32} & d_{33} & d_{34} & d_{35} & d_{36} \end{bmatrix} \begin{bmatrix} E_x^2 \\ E_y^2 \\ E_z^2 \\ 2E_y E_z \\ 2E_x E_z \\ 2E_x E_y \end{bmatrix} \quad (2.11)$$

Equation (2.11) shows that the nonlinear tensor d has 18 elements. For crystals which lack a centre of inversion, each element is zero. This is not the case for materials with a centre of inversion, whereby the majority of terms are non-zero. Symmetry within the nonlinear crystal allows the number of independent elements to be reduced from 18 to 10 providing that the following conditions are met

$$d_{12} = d_{26}, d_{13} = d_{35}, d_{14} = d_{36} = d_{25}, d_{15} = d_{31}, d_{16} = d_{21}, d_{24} = d_{32}, \quad (2.12)$$

which is known as Kleinman symmetry [10]. These components can be used to obtain an effective coupling strength of interacting waves, d_{eff} :

$$d_{eff} = p_1 d p_2 p_3 = p_2 d p_3 p_1 = p_3 d p_1 p_2, \quad (2.13)$$

where p represents the unit polarisation vector. From this, it is seen that high values of d_{eff} lead to high $\chi^{(2)}$ and therefore greater conversion. Crystals with high d_{eff} values are therefore desirable for efficient frequency generation.

2.6 Phase matching (Type I and Type II)

Waves which are said to be phase matched adhere to the condition that the fundamental wave ω_1 travels with the same wave-vector direction as the induced frequency-converted nonlinear wave ω_3 , i.e. where the phase difference is described as

$$\Delta k = k_3 - k_2 - k_1 = 0, \quad (2.14)$$

where $k_i = 2\pi n_i / \lambda_0$. However, due to the presence of material dispersion, as described in Section 2.3, $n_o(\omega) \neq n_e(\omega)$. This results in the waves drifting out of phase, resulting in a phase mis-match, i.e. $\Delta k \neq 0$. Therefore the amount of the frequency converted light ω_3 produced will decrease until the waves reach a point at which they are out of phase by a factor of π . At this point, destructive interference takes place, eliminating the previously generated wave through a back-conversion process. The distance propagated before the energy in a nonlinearly generated wave reaches a maximum is referred to as the coherence length l_c which is given by

$$l_c = \frac{\pi}{2\Delta k} \quad (2.15)$$

Type I phase matching may be used to address this difference in phase. Using this technique, two input beams have the same polarisation and generate a beam with polarisation perpendicular to these.

This can occur for two differing types of crystal; negative and positive. Type I phase matching in negative crystals ($n_o > n_e$) positive crystals ($n_o < n_e$) can be described by $\omega_{1,o} + \omega_{2,o} = \omega_{3,e}$ and $\omega_{1,e} + \omega_{2,e} = \omega_{3,o}$ respectively, and can be illustrated by the index ellipsoids, as shown in Fig. 2.1.

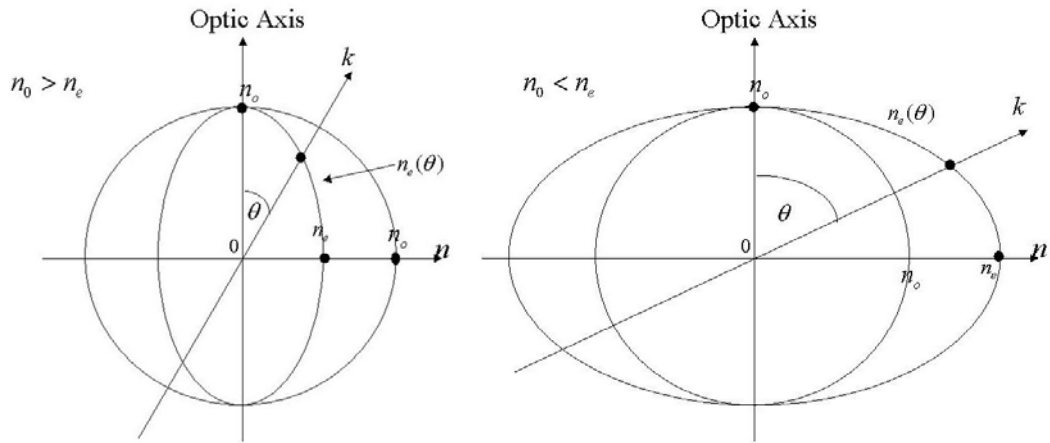


Figure 2.15 An illustration of the matching of refractive indices for an ordinary and extraordinary wave in a) negative uniaxial crystal and b) positive uniaxial crystal.

Type II phase matching corresponds to the case where input beams have orthogonal polarisations. The output of this type of phase matching leads to four possible polarisation combinations as illustrated in Table 2.3.

<i>Crystal type</i>	<i>Polarisation (ω_1)</i>	<i>Polarisation (ω_2)</i>	<i>Polarisation (ω_3)</i>
Negative	o	e	e
Negative	e	o	e
Positive	o	e	o
Positive	e	o	o

Table 2.3 Type II phase matching polarisation combinations

2.7 Quasi-phase matching

Traditionally, phase matching has the requirement for a zero phase mismatch ($\Delta k=0$), however there is an alternative technique known as quasi-phase matching (QPM), which does not have this limitation.

The concept of QPM was first published in 1962 by Armstrong et al [5]. The idea behind this is to introduce a periodic poling structure in the crystal which will compensate for the phase mismatch between the interacting waves. As discussed in Section 2.3, without phase matching, the generated frequency will start to decrease after propagating through one coherence length. By periodically reversing the sign of the nonlinear coefficient every coherence length, this has the effect of adding π to the phase shift of the interacting waves. This reversing of the nonlinear coefficient is achieved through applying periodic electric current to the crystal during fabrication. In the case of lithium niobate, the material used in this thesis, this process permanently reverses the orientation of the Lithium and Niobium ions. Consequently, the energy from the fundamental wave will continuously be converted to the new frequency.

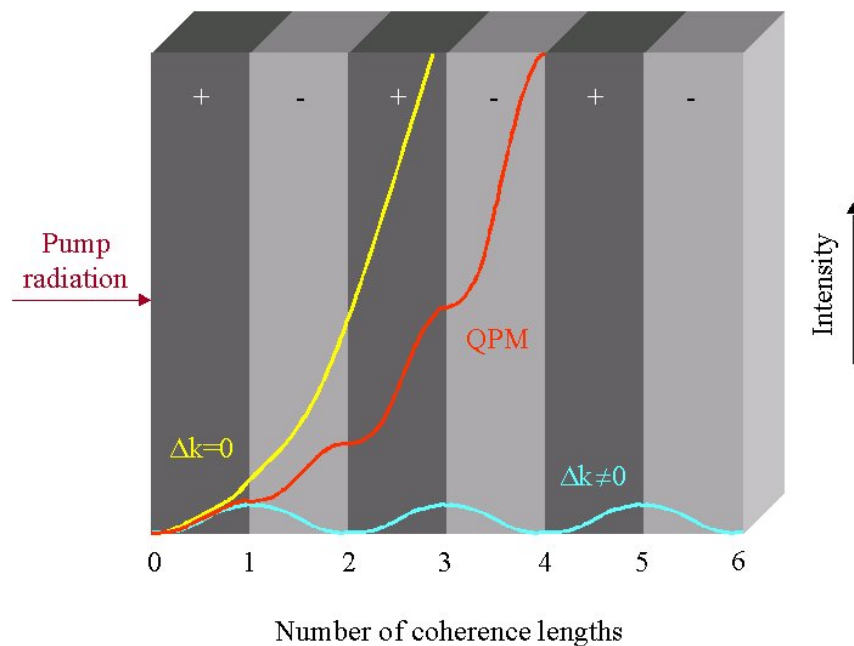


Figure 2.2 Three conditions are shown a) conventional phase matching where $\Delta k = 0$ b) quasi-phase-matching and c) where no phase matching is used $\Delta k \neq 0$ [11].

Considering the phase matching condition for a QPM OPO

$$\Delta k_{QPM} = k_3 - k_1 - k_2 - \frac{2\pi}{\Lambda} \quad (2.16)$$

where Λ is known as the period length which is double the coherence length $2l_c$ (given in Eq. (2.15)). By comparison with Eq. (2.14) it is seen that the additional term of $2\pi/\Lambda$ is present. This is the phase mismatch and it is seen in the following section that this can be used to control the frequency of generated light.

2.8 Periodically poled Lithium Niobate (PPLN) fabrication

Lithium niobate (LiNbO_3) is a medium which is widely used throughout nonlinear optics. It has many properties which make it particularly suitable for this field. These include a high degree of nonlinearity and also a very broad transmission range [12].

The first full description of the structure of LiNbO_3 was published by Abrahams *et al* in 1966 [13]. This description highlighted that the positions of the lithium and niobium ions give rise to a dipole moment. If a large enough electrical current is applied across the crystal, the position of the metal ions relative to the oxygen molecules can be permanently shifted, in order to invert the dipole moment of the crystal. This is illustrated in Fig. (2.3), which shows the basis of periodic poling described previously.

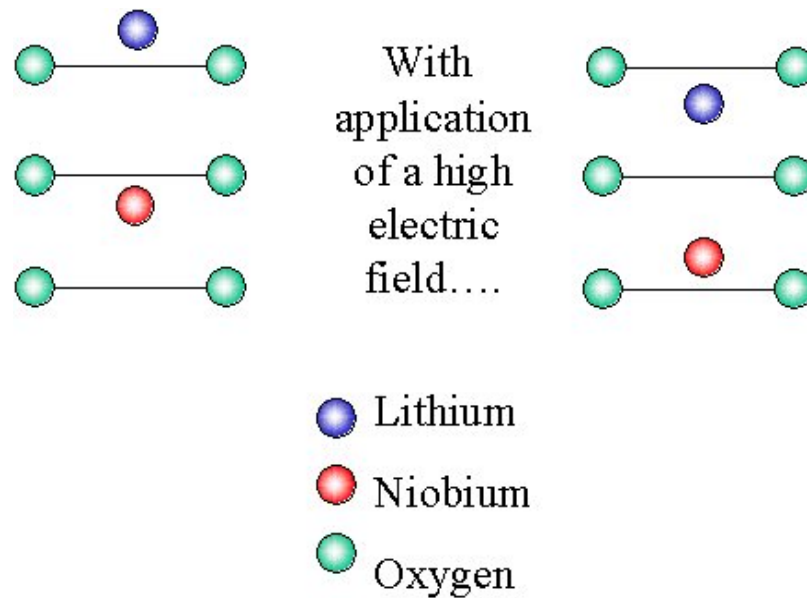


Figure 2.3 Orientation of ions within Lithium Niobate before and after application of a strong electric field. [courtesy of Dr G McConnell]

By periodically applying electric fields across the crystal it becomes possible to have a crystal where a wave experiences an alternating polarisation at every coherence length l_c upon propagation through the crystal. This meets the requirements for QPM described in Section 2.7. Where this process is applied to Lithium Niobate, the resultant material is known as periodically poled Lithium Niobate (PPLN). As PPLN allows phase matching using the highest effective nonlinear coefficient and also has a very high damage threshold, which will be discussed in more detail in Chapter 4, PPLN is a very important crystal within nonlinear optics.

Other techniques can be used for periodic poling such as chemical and thermal methods, however these are not as successful as the case for electrical poling [14, 15].

2.9 Material tolerances

When implementing a nonlinear crystal for the purpose of frequency conversion, it is important to note the tolerances incurred by the crystal. These tolerances are

described by the following parameters; walk off, spectral acceptance bandwidth $\delta\lambda$, crystal temperature acceptance bandwidth δT , and tolerance to angle of incidence $\delta\nu$.

Values for these can be calculated for QPM crystals [16], where the pump source is assumed to be cw with a plane wave approximation. Perfect periodicity of poling is assumed for calculations presented in this thesis.

2.9.1 Walk-off

When considering the propagation direction of a laser beam passing through an isotropic crystal, the beam will follow a path described by the wave-vector \mathbf{k} which is perpendicular to the wavefront and dependent on the properties of the crystal. However, if crystals which exhibit birefringence such as those used in nonlinear optics are considered, \mathbf{k} no longer accurately describes the direction of energy flow or the beam direction. This occurrence is a result of an effect known as ‘spatial walk-off’.

Spatial walk-off is a result of an extraordinary polarised beam which enters a crystal at an angle θ to the optic axis. By changing θ , the refractive index experienced by the extraordinary beam n_e may be altered, and it can be seen that the walk-off angle ρ is dependent on this value

$$\tan \rho = \frac{[n_e(\theta)]^2}{2} \left[\frac{1}{(n_e)^2} - \frac{1}{(n_o)^2} \right] \sin 2\theta. \quad (2.17)$$

Note that for the special case of non-critical phase matching ($\theta = 90^\circ$) walk-off effects are seen to be zero, $\rho = 0$ [17].

The direction of energy propagation for the pump signal and idler beams are described by their respective Poynting vectors ($\mathbf{S}_{o,e}$). As each vector will have a different walk-off angle ρ , the beams will drift out of their spatial overlap upon propagation through the crystal. This leads to inefficient conversion from the pump beam to the generated frequencies.

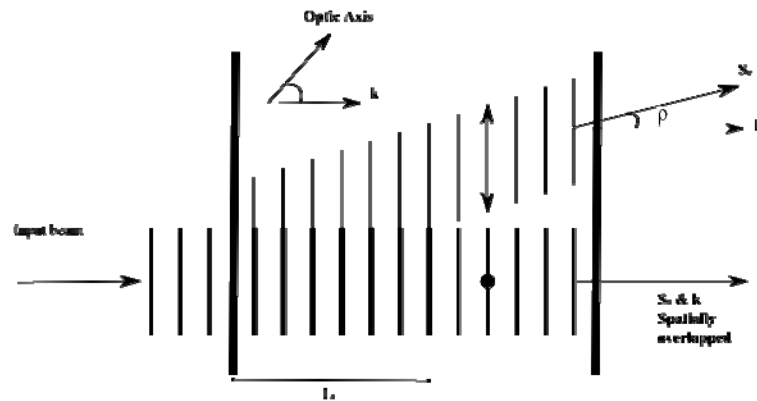


Figure 2.4 The effect of spatial walk off within a nonlinear crystal

The refractive index for an ordinary polarised beam n_o is independent of the input angle and therefore the Poynting vector overlaps with the \mathbf{k} vector. Figure 2.4 shows that there is a length l_a , beyond which conversion becomes negligible, this is known as the aperture length and is calculated using

$$l_a = \pi^{1/2} \frac{w}{\rho}, \quad (2.18)$$

where w is the beam waist. There is no benefit to employing a crystal longer than this length due to the effective aperturing of the output.

One of the benefits of quasi-phase matching is that spatial walk-off is eliminated due to the pump beam propagating in the direction of the optic axis, and therefore provides efficient conversion and allows the use of longer crystals.

When considering pulsed sources, it is important to consider the different group velocities of the pump and generated frequencies as a result of the material dispersion described in Section 2.3. An approximation of the crystal length over which these pulses separate can be defined as

$$L = \frac{c\tau_\omega}{\Delta n}. \quad (2.19)$$

2.9.2 Spectral acceptance

The spectral acceptance bandwidth is a measure of the pump wavelength range which produces gain equal to that of the FWHM of the parametric gain curve at the maximum value i.e. $\Delta k = 0$. This is given by

$$\delta\lambda = \frac{0.4429\lambda}{L} \left| \frac{n_2 - n_1}{\lambda} + \frac{\partial n_1}{\partial \lambda} - \frac{1}{2} \frac{\partial n_2}{\partial \lambda} \right|^{-1}, \quad (2.20)$$

where L is the length of the nonlinear crystal, and n_1 and n_2 are the refractive indices experienced by the pump and the frequency converted beams respectively.

From Eq. (2.20), it can be seen that the spectral bandwidth is inversely proportional to the length of crystal; hence shorter crystals will yield larger acceptance

bandwidths. Ideally, the spectral acceptance of the crystal should cover the bandwidth of the pump source.

2.9.3 Temperature acceptance

Temperature plays a critical role not only in phase matching but also in the tuning of the generated output wavelength, as mentioned previously. Therefore attention must be paid to the range of temperatures over which conversion is efficient. Temperature bandwidth δT , describes the range of temperature defined by the range of two points which produce the FWHM for the maximum parametric gain curve. This is given as

$$\delta T = \frac{0.4429\lambda}{L} \left| \frac{\partial \Delta n}{\partial T} + \alpha \Delta n \right|^{-1}, \quad (2.21)$$

where α is the coefficient of linear thermal expansion.

2.9.4 Angular acceptance

The final acceptance parameter described is that of angular acceptance, $\delta \nu$. This value defines the FWHM range between two angles which produces the maximum gain curve.

$$\delta \nu = 2 \sqrt{1.772 \frac{n_2}{n_1} \frac{l_c}{L} \cos(\nu)} \quad (2.22)$$

Here, ν is defined as the angle at which the fundamental beam propagates (in the $x - z$ plane) with respect to the normal of the crystal surface.

2.10 Nonlinear optical frequency conversion in optical fibres

Supercontinuum generation (SC) is a nonlinear optical phenomenon which occurs as a result of the various nonlinear processes which are induced by the interaction between narrowband, high intensity lasers and a nonlinear medium. Such a medium can be a bulk nonlinear crystal; however it is conventional to use a fibre with a micro-structured core. Upon propagation through such a fibre, the spectrum may be substantially broadened, often to greater than an optical octave [18].

Following from its first observation by Alfano et al in 1970 [19], where a picosecond source was focused into glass, a wealth of applications have been found for such broadband sources. These include fluorescence microscopy [20], materials characterisation [21] and frequency combs [22].

The first observation of SC generation in optical fibres was performed by Lin et al in 1976 [23]. This was performed by pumping a standard silica fibre in the normal group velocity regime. In this case the spectral broadening was attributed to the combination of self-phase modulation, Raman scattering, four-wave mixing and cross phase modulation. With the introduction of photonic crystal fibres (PCF), which allow the zero-dispersion wavelength (ZDW) to be tailored and confine the input light into a small core [24]. High intensities may be achieved and from many commercial lasers with reasonable pump powers.

2.10.1 Overview of photonic crystal fibres

Photonic crystal fibres possess unique characteristics when comparing to those in conventional fibres. The PCF tends to have a solid silica core, a few microns in diameter. Unlike standard fibres which use a solid cladding to confine the beam within the fibre, a PCF uses a microstructured air-silica cladding as shown in Fig.2.5. the cores of these fibres may be designed to be as small as 1 μm [25].

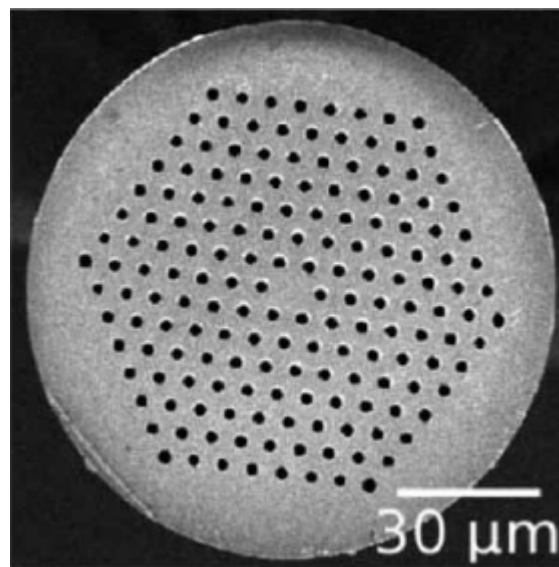


Figure 2.5 A scanning electron microscope image of a PCF microstructure (reproduced from [26])

Control of this microstructure allows increased control of the modal, dispersive and nonlinear effects which occur within the fibre [25, 27]. This core is created through stacking silica rods and tubes in the desired structure and then heated in a controlled manner to draw all of these components down to the size of a typical fibre [27]. Through control of the PCF structure geometry, the dispersion of the fibre may be controlled. As a result the ZDW may be selected based upon this structure [28]. Due to these exceptional properties, PCFs are well-suited to SC generation, with resulting emission demonstrated to span more than an optical octave [29]. The mechanisms behind SC generation include self-phase modulation (SPM) and Raman scattering.

2.10.1.1 Self-phase modulation

One of the dominant effects related to SC generation is that of SPM. This nonlinear phenomenon is induced by the Kerr effect. Due to the third order nonlinear electric polarization ($\chi^{(3)}$) present in the medium, the high intensity of light induces a variation of the refractive index within the medium,

$$n = n_L + n_2 I(\omega). \quad (2.23)$$

In Eq. (2.23), n_L is the linear refractive index, $I(\omega)$ is the optical intensity and n_2 is the nonlinear refractive index coefficient, described by [30]:

$$n_2 = \frac{3}{8n_L} R_e(\chi^{(3)}) \quad (2.24)$$

where R_e represents the real part of the optical field.

Specifically, SPM refers to the self-induced phase shift which is incurred upon propagation through the fibre φ^{SPM}

$$\varphi^{SPM} = \frac{2\pi L}{\lambda} n_2 I(\omega). \quad (2.25)$$

Here, L is the interaction length of the wave with the material. This phase shift corresponds to broadening of the optical spectrum as the pulse propagates through the fibre.

2.10.1.2 Raman scattering

The second dominant effect which will be discussed to help describe SC generation is that of Raman scattering. Stimulated Raman scattering is an inelastic linear effect, created by a photon-phonon interaction [9]. Through interaction with a medium such as a PCF, the energy from an intense pump beam is shifted to lower frequencies (Stokes wave) through scattering from vibrational modes of the material molecules. Shifting of energy to higher frequencies (anti-Stokes wave) can also occur but is less efficient.

$$2\omega_p \rightarrow \omega_{as} + \omega_{st} \quad (2.26)$$

Here, ω_p , ω_{as} and ω_{st} represent the frequencies of the pump, anti-Stokes and the Stokes photons. This process results in shifts in frequency, resulting the broadening of the spectrum.

2.11 Conclusion

This chapter provided a brief overview of basic nonlinear optics, with the aim of describing the nonlinear processes involved in the experiments reported in the following chapters. The benefits of quasi-phase matching were described along with a description of crystal tolerances and practical considerations for nonlinear optical

frequency conversion. A brief overview of supercontinuum generation was also given.

2.12 References

1. Maiman, T., *Stimulated optical radiation in ruby*. Nature, 1960: 187, p. 493.
2. Franken, P., P.A. Franken, A.E. Hill, C.W. Peters, and G. Weinreich, *Generation of optical harmonics*. Physical Review Letters, 1961. **7**(4): p. 118.
3. Pawley, J., *Handbook of biological confocal microscopy*. 1995: Plenum Press.
4. Benson, H., *University physics*. 1996: John Wiley.
5. Armstrong, J., N. Bloembergen, J. Ducuing, and P.S. Pershan, *Interactions between light waves in a nonlinear dielectric*. Physical Review, 1962. **127**(6): p. 1918.
6. Risk, W., T. Gosnell, and A. Nurmikko, *Compact blue-green lasers*. 2003: Cambridge University Press.
7. Koechner, W., *Solid-state laser engineering*. 2006: Springer.
8. Jundt, D.H., *Temperature-dependent Sellmeier equation for the index of refraction, n_e , in congruent lithium niobate*. Journal of Applied Physics, 1974. **45**: p. 3688.
9. Agrawal, G., *Nonlinear fiber optics*. 2007: Academic Press.
10. Kleinman, D., *Nonlinear dielectric polarization in optical media*. Physical Review, 1962. **126**(6): p. 1977.
11. Harris, J., G. Norris, and G. McConnell, *Characterisation of periodically poled materials using nonlinear microscopy*. Optics Express, 2008. **16**(8): p. 5667.
12. Myers, L.E. and W.R. Bosenberg, *Periodically poled lithium niobate and quasi-phase-matched optical parametric oscillators*. IEEE Journal of Quantum Electronics, 2002. **33**(10): p. 1663.

13. Abrahams, S., J. Reddy, and J. Bernstein, *Ferroelectric lithium niobate. 3. Single crystal X-ray diffraction study at 24 C*. Journal of Physics and Chemistry of Solids, 1966. **27**(6-7): p. 997.
14. Risk, W. and S. Lau, *Periodic electric field poling of KTiOPO using chemical patterning*. Applied Physics Letters, 1996. **69**: p. 3999.
15. Houe, M. and P. Townsend, *An introduction to methods of periodic poling for second-harmonic generation*. Journal of Physics D: Applied Physics, 1995. **28**: p. 1747.
16. Fejer, M., Magel, G.A. Jundt, D.H and Byer, R.L., *Quasi-phase-matched second harmonic generation: tuning and tolerances*. IEEE Journal of Quantum Electronics, 2002. **28**(11): p. 2631.
17. Goldberg, L., W. Burns, and R. McElhanon, *Wide acceptance bandwidth difference frequency generation in quasi phase matched LiNbO*. Applied Physics Letters, 1995. **67**: p. 2910.
18. Genty, G., S. Coen, and J.M. Dudley, *Fiber supercontinuum sources (Invited)*. Journal of the Optical Society of America B, 2007. **24**(8): p. 1771.
19. Alfano, R. and S. Shapiro, *Emission in the region 4000 to 7000 Å via four-photon coupling in glass*. Physical Review Letters, 1970. **24**(11): p. 584.
20. McConnell, G. and E. Riis, *Two-photon laser scanning fluorescence microscopy using photonic crystal fiber*. Journal of Biomedical Optics, 2004. **9**: p. 922.
21. Esposito, E., F.J. Kao, and G. McConnell, *Confocal optical beam induced current microscopy of light-emitting diodes with a white-light supercontinuum source*. Applied Physics B: Lasers and Optics, 2007. **88**(4): p. 551.
22. Takara, H., T. Ohara, K. Mori, K. Sato, E. Yamada, Y. Inoue, T. Shibata, M. Abe, T. Morioka and K-I. Sato, *More than 1000 channel optical frequency chain generation from single supercontinuum source with 12.5 GHz channel spacing*. Electronics Letters, 2002. **36**(25): p. 2089.
23. Lin, C. and R. Stolen, *New nanosecond continuum for excited state spectroscopy*. Applied Physics Letters, 2009. **28**(4): p. 216.

24. Skryabin, D., F. Luan, J.C. Knight and P.S.J. Russell, *Soliton self-frequency shift cancellation in photonic crystal fibers*. Science, 2003. **301**(5640): p. 1705.
25. Russell, P., *Photonic crystal fibers*. Science, 2003. **299**(5605): p. 358.
26. Noordegraaf, D., L. Scolari, J. Lægsgaard, T.T. Alkeskjold, G. Tartarini, E. Borelli, P. Bassi, J. Li, and S-T. Wu
, *Avoided-crossing-based liquid-crystal photonic-bandgap notch filter*. Optics Letters, 2008. **33**(9): p. 986.
27. Birks, T., J. Knight, and P.S.J. Russell, *Endlessly single-mode photonic crystal fiber*. Optics letters, 1997. **22**(13): p. 961.
28. Ferrando, A., E. Silvestre, J.J. Miret, J.A. Monsoriu, M.V. Andres, P.S.J. Russell., *Designing a photonic crystal fibre with flattened chromatic dispersion*. Electronics Letters, 1999. **35**(4): p. 325.
29. McConnell, G. and E. Riis, *Ultra-short pulse compression using photonic crystal fibre*. Applied Physics B: Lasers and Optics, 2004. **78**(5): p. 557.
30. Stolen, R. and C. Lin, *Self-phase-modulation in silica optical fibers*. Physical Review A, 1978. **17**(4): p. 1448.

Chapter 3 Non-destructive structural analysis of periodically poled Lithium Niobate using optical microscopy techniques

3.1 Introduction

As described in Chapter 2, the application of nonlinear optical crystals for frequency conversion techniques allows the generation of coherent sources which can operate at frequencies which are not easily achievable directly from laser gain media. QPM is a useful tool for achieving high frequency conversion whilst permitting a phase mismatch of $\Delta k \neq 0$, through periodic inversion of the nonlinear coefficient. The overall efficiency increase of this periodic reversal is based upon phase mis-match as described in Eq. (2.16) and its application with the coupled amplitude equations in (2.4). This describes how the periodic structure can compensate for the differing wave vectors of the fundamental and generated frequencies. The length of the domain period Λ is prescribed at the point of crystal manufacture.

$$\Lambda = \frac{2\pi}{k_3 - k_1 - k_2 - \Delta k} \quad (3.1)$$

The fabrication process is described in more detail in Chapter 2.8.

Periodically poled crystalline materials are extremely attractive due to the very high nonlinear frequency conversion efficiencies possible [1] and, as such, processes such as SHG [2], SFM [3] and OPO [4] can be greatly improved. In order to optimise these materials, the micro-domain structures made by the application of very high electric fields at the design stage have to be fabricated with sub-micron tolerance [1]. In order to use QPM as a method for phase mis-match compensation, the correct period length must be selected. Although this is dependent upon the input

frequencies which are used, approximate lengths of between 5 – 30 μm are common for the previously described nonlinear processes [5]. Such accuracy in fabrication lengths are required in order to ensure that the overall conversion efficiency process is maximised. Periodic poling may be applied to many commonly used nonlinear crystals including Lithium Niobate (LiNbO_3) [6], Lithium Tantalate (LiTaO_3) [7] and Potassium Titanyl Phosphate (KTP) [8]. Analysis of QPM structures is critical to assess the quality and effectiveness of such a device, as this impacts upon the conversion efficiency. Hence non-destructive optical techniques are well suited to study these complex materials.

Nonlinear crystals are often found to be doped with compounds which are used to enhance specific optical properties of a crystal. Using LiNbO_3 as an example of a commonly used nonlinear crystal, it is often the case that the crystal will be doped with magnesium oxide (MgO). This impurity is typically in the order of 5 %. This compound is introduced in the fabrication process and has been shown to increase resistance of the material to photo-refractive damage [9]. Optical damage within LiNbO_3 crystals are a result of vacancies in the structure of the crystal. In a model by Iyi et al [10], it was highlighted that the introduction of MgO resulted in the generation of larger amounts of Li vacancies. As a result, higher photoconductivity is incurred resulting in increased optical damage resistance. An additional and important property of this dopant is that it exhibits luminescence. Luminescence is a process in which a material absorbs photons and then re-radiates photons of a lower energy. The period between absorption and emission is typically on the order of 10 ns and therefore can be considered as analogous to fluorescence in this case. With a peak absorption at 465 nm [11] and emission at 508 nm [12], MgO may be used as a contrast mechanism to obtain optical images of crystals and their structure. Other commonly used dopants which have been implemented in order to improve the characteristics of nonlinear crystals have also been shown to exhibit luminescence (e.g. ZnO and Er^{3+}) [11, 13].

Conventional brightfield microscopy has been demonstrated as a method to determine the uniformity and linearity of periodically poled crystals (an example of which is shown in Fig. 3.1) [14]. Despite this technique allowing for analysis of the periodic structure and damage observed at the surface of the device, defects or inhomogeneities cannot be observed at depth within the crystal.

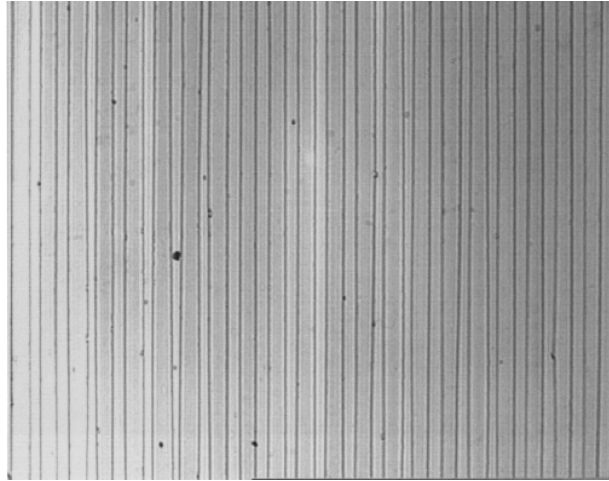


Figure 3.1 Bright-field image of a Mg doped PPLN crystal with a grating period of 25 μm [14]

Alternative studies implementing CLSM [13] and second harmonic generation laser scanning microscopy (SHG LSM) [15] have also been performed in order to provide structural information at depths of up to several tens of μm inside the crystal. These methods provide an improvement upon brightfield imaging, when considering application to the internal inspection of periodically poled crystals. The contrast mechanisms for these techniques are described in Chapter 1.3. However, these laser scanning techniques both exhibit important limitations.

CLSM may be applied to stimulate luminescence within doped regions of a device, the signal from which may be collected at various depths in order to provide optically sectioned images. They may be compiled to provide a three dimensional stack of images for analysis. Unfortunately, CLSM can only penetrate thin

periodically poled crystals ($< 20 \mu\text{m}$) as a result of the single photon absorption process, yet thicker materials are generally used [4, 6]. This limitation was highlighted in a study by Dierolf et al [16].

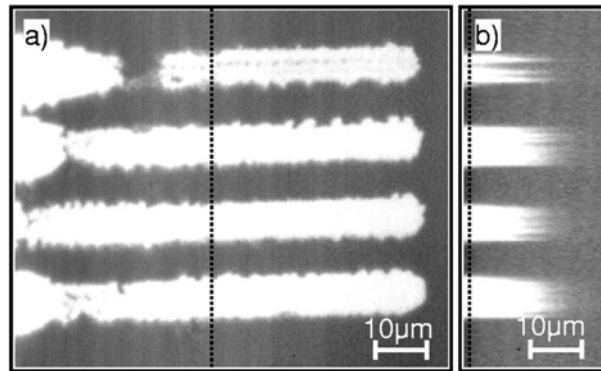


Figure 3.2 Confocal luminescence imaging of a doped PPLN crystal. a) x-y image at a depth of $2 \mu\text{m}$ and b) vertical cross section of the device (reproduced from [16]).

From Fig. 3.2, it can be seen that a depth of approximately $20 \mu\text{m}$, effectively no luminescence could be detected.

SHG LSM, on the other hand, implements longer wavelengths for analysis and hence deeper penetration, however it is a complex technique, requiring correct orientation of the nonlinear crystal relative to the excitation source. Additionally the sample must be temperature controlled in order to ensure efficient generation of SHG through phase matching [17]. When phase matching is not implemented, the SHG signal can be extremely low and therefore careful selection of the detection method is necessary to ensure the greatest signal-to-noise ratio. An example of this was shown by Uesu *et al* [18], where interference techniques were employed to discriminate the low intensity SHG signal from noise to create optical contrast images of periodically poled domains in LiTaO_3 . Results of this study are reproduced in Fig 3.3.

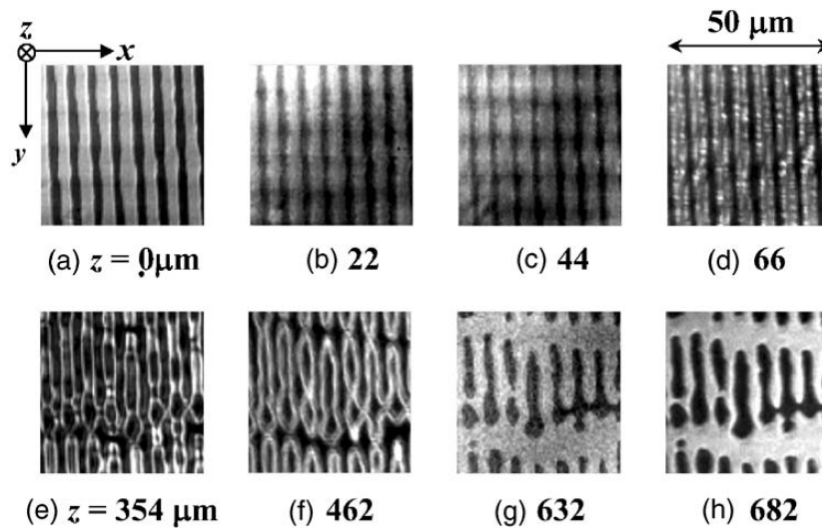


Figure 3.3 SHG tomography of a periodically poled LiTaO₃ crystal at depths of up to 682 μm with use of a SHG interference microscope (reproduced from [18]).

This highlights the depth penetration capabilities of SHG LSM, with useful signal observable at depths in excess of 650 μm. Despite this benefit, the phase matching requirements of this technique introduces additional cost and complexity to the nonlinear imaging system.

The technique of MPLSM, as described in Chapter 1.5, may be used as a novel, non-destructive method for period length analysis throughout the entire depth of a periodically poled crystal. Instead of fluorescence, luminescence generated from the dopant may be used as the contrast mechanism. MPLSM of such a crystal is independent of crystal orientation or temperature as the nonlinear excitation does not depend upon phase matching conditions. The luminescence excitation and emission bandwidths are also very broad [19] when compared to the strict requirement of SHG LSM, where narrowband excitation leads to SHG emission signal at exactly double the frequency of the excitation beam. By comparison MPLSM of a periodically poled crystal can be conducted using standard, commercial multiphoton microscopes and laser sources. Detection over a spectral bandwidth of > 10 nm results in a high signal intensity producing high resolution, high contrast images. In addition to these advantages, multiphoton excitation implements longer wavelengths, resulting in less

Rayleigh scattering and hence allowing deeper penetration. Localisation of excitation due to the nonlinear absorption process also ensures that there is no absorption of the excitation beam before reaching the focal plane [20]. As a result, imaging depths of several hundred μm may be achieved [21].

In this chapter, MPLSM is presented as a novel method for the generation of three-dimensional reconstructions of periodically poled crystals through detection of luminescence resulting from the dopant in the crystal. This permits characterisation and damage analysis throughout the entire depth of thick crystals. The commercial multiphoton system will be compared with an equivalent CLSM platform and results from each will be presented. These methods were demonstrated on a sample crystal of magnesium-oxide doped periodically poled lithium niobate (MgO:PPLN). Properties such as wide transparency over the EM spectrum [22], high nonlinearity [23] and high damage threshold [5] make MgO:PPLN one of the most commonly used nonlinear crystals throughout frequency conversion applications and therefore a useful sample for investigation.

3.2 Experiment

The sample which was used in this experiment was a periodically poled MgO:LiNbO₃ crystal. The uncoated crystal had the following dimensions; length of 5 mm, height of 10 mm, and a depth of 250 μm , as shown in Fig. 3.4.

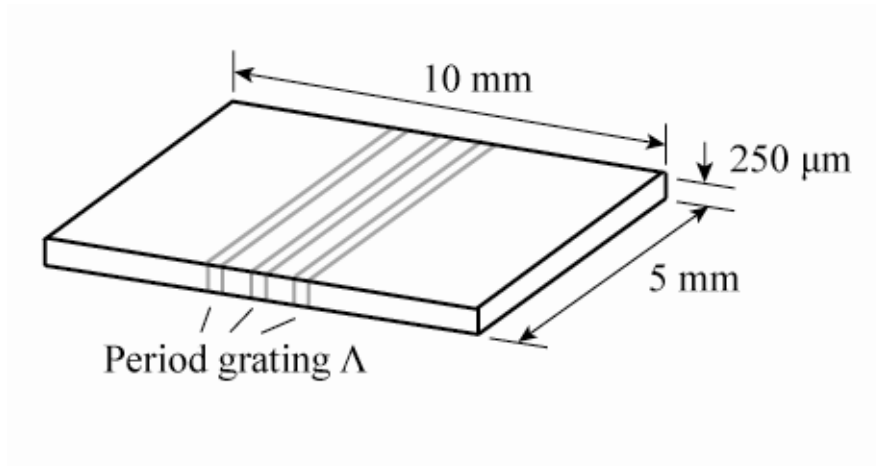


Figure 3.4 Dimensions of the nonlinear crystal used for analysis.

Three period lengths of 10.2, 10.4 and 10.6 μm were specified by the manufacturer. These period lengths are designed for QPM SHG of 1250 nm from a chromium forsterite laser. The period used for this experiment was the 10.6 μm grating, with a manufacturer's estimated single pass efficiency of $\sim 20\%$.

Figure 3.5 highlights the basic experimental setup for both CLSM and MPLSM techniques. In each case, a laser scanning system was coupled into an upright microscope which implemented a 20x (0.75 NA) air immersion lens. This lens was selected to ensure a wide field of view providing analysis of a large section of the crystal whilst maintaining high resolution.

For the CLSM study, a confocal laser scanning system (Leica SP5) coupled to an upright microscope (Leica DM6000). An average power of 1 mW from a $\lambda = 488\text{ nm}$ emitting Krypton/Argon laser source was used to generate single photon luminescence within the crystal. The axial and lateral resolution of this system were calculated from Eq. 1.3 and 1.4 and found to be 1.64 and 0.39 μm respectively. As period lengths tend to be on the order or $> 5\ \mu\text{m}$, as described in section 3.1, this system provides ample resolution for imaging of such structures.

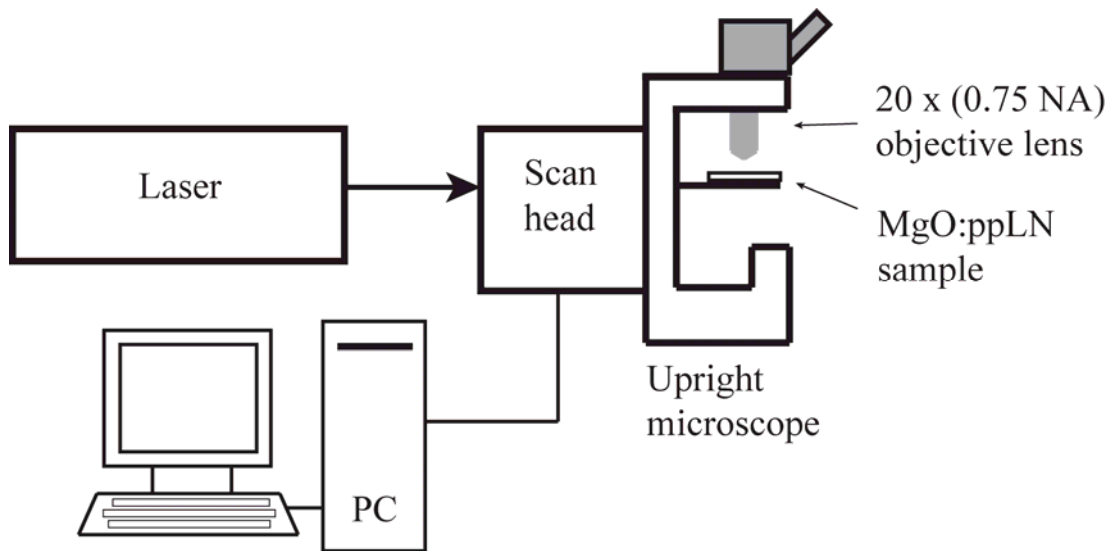


Figure 3.5 Basic experimental setup for both the CLSM and MPLSM platforms

The peak absorption wavelength of the dopant MgO has previously been shown to be 465 nm [11]. The closest source available to this peak excitation wavelength from the CLSM platform was $\lambda = 488$ nm. Through a combination of interchangeable optical filters, the Leica SP5 detection system permitted a detection range which is suitable for the intended application. A detection range of $\lambda = 500 - 600$ nm (spectral resolution of 5 nm) was selected in order to provide optimal luminescence detection whilst blocking the 488 nm excitation source.

For the MPLSM imaging, a laser scanning system (Bio-Rad Radiance MP2000) was coupled into an upright microscope (Nikon E600FN). The excitation source was 1 W, 140 fs-pulsed Ti:Sapphire laser (Chameleon, Coherent), providing a repetition rate of 90 MHz at wavelength of $\lambda = 860$ nm. Using a 20x (0.75 NA) objective, this provided lateral and axial resolutions of 1.05 μm and 1.52 μm respectively. The laser was heavily attenuated in order to provide an average power of 6 mW at the sample plane. The 860 nm wavelength was selected as a result of the flexibility of the MPLSM system. Through use of the continuous tuning properties of the Ti:Sapphire laser, the optimal excitation could be found empirically, ensuring highest efficiency. Contrary to the descanned detection used for the Leica SP5 CLSM system, the

Radiance MP2000 permitted the use of non-descanned detection, allowing any optical loss incurred by the luminescent signal upon travelling through the scan head to be overcome, hence allowing more efficient detection. An optical short-pass filter (700SP, Chroma Technologies) was implemented to ensure that the Ti:Sapphire laser was blocked and the generated luminescence could pass through for detection and creation of contrast images.

Optical sectioned images of 512^2 pixels were captured at a rate of approximately 1 Hz for both systems, with a z-step size of $1\ \mu\text{m}$ used to provide the data required for three dimensional imaging throughout the entire $250\ \mu\text{m}$ depth of the crystal. Image analysis software (Velocity 4, Improvion) was then used to create full three dimensional images of the poling structure of the crystal. Measurements of the domain period length could then be made using the same software. By scanning through the optical sections generated, regions of photo-induced dome and period inhomogeneity could be observed at depth.

3.3 Results

Individual imaging parameters such as aperture size for CLSM and wavelength optimisation for MPLSM were optimised individually for both systems. For single photon luminescence excitation, the Krypton/Argon laser source was operated at maximum power, i.e. 1 mW. The PMT settings were also optimised to achieve the highest signal to noise ratio. For multiphoton luminescence excitation, only 20 % of the available 30 mW excitation power (6 mW) was implemented combined with low gain settings.

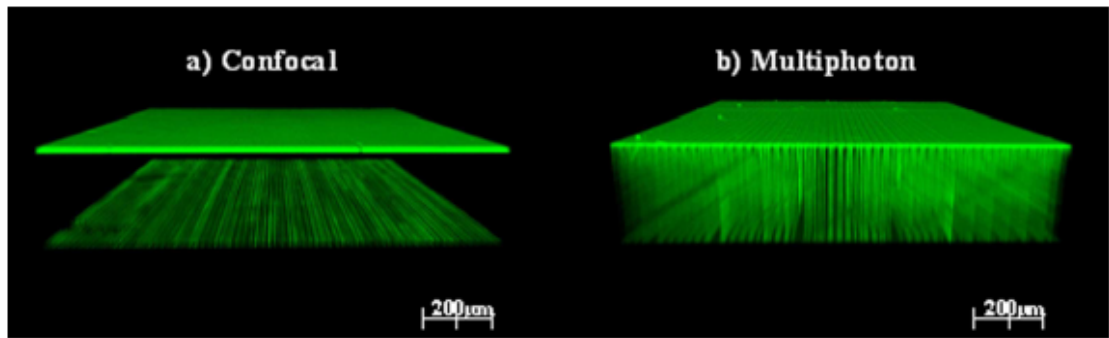


Figure 3.6 Comparison of 3D reconstructions obtained using a) CLSM and b) MPLSM

Figure 3.6 shows a typical three dimensional reconstructions generated using a) the CLSM system and b) the MPLSM system. Upon inspection, the structural detail observed when using multiphoton excitation is far superior to that of single photon excitation.

This improvement is attributed to several factors; (1) less absorption of the excitation source is incurred above the focal plane within the crystal [21]; (2) the MPLSM allowed the implementation of non-descanned detectors which allowed for direct detection and hence greater signal to noise performance; (3) as a result of the nonlinear excitation process, luminescence was only generated within a highly localised focal volume and therefore circumvented the need for an aperture to reject luminescence generated outside of the focal plane, resulting in improved signal detection [21]; and (4) longer wavelengths result in less Rayleigh scattering and hence permitted deeper penetration.

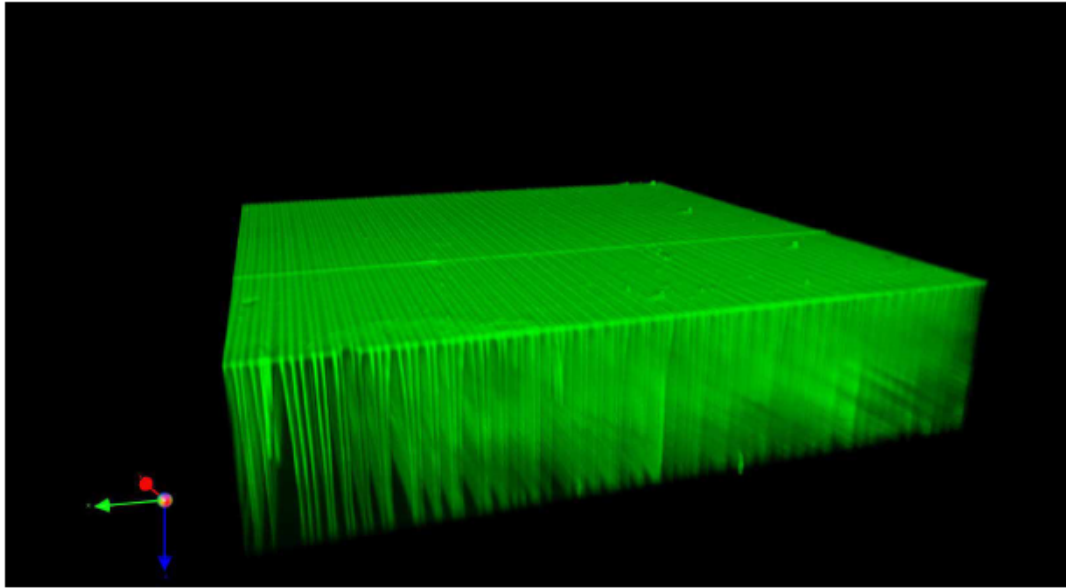


Figure 3.7. A snapshot from a movie of the 3D reconstruction of the luminescent MgO regions within the MgO:PPLN crystal obtained using MPLSM and Velocity 4 software

Figure 3.7 shows a snapshot from a movie of the three dimensional reconstruction of the MgO:PPLN crystal using the MPLSM platform combined with the imaging software. This is a powerful method of analysis as it may be used to thoroughly inspect the crystal visually from different angles, both internally and externally. From Fig 3.7 it is apparent that irregularities within the poling period exist.

Figure 3.8 presents a more quantitative method for analysis of the periodicity and quality of the poling domains. Image a) in the figure displays a comparison between the lateral view and the (XY) and the axial view (XZ) from the reconstruction described in Fig. 3.7. The XY section was imaged at a depth of 20 μm below the top surface of the crystal. For the purposes of clarity and for discussion, three columns have been highlighted which illustrate different features which were observed throughout this study.

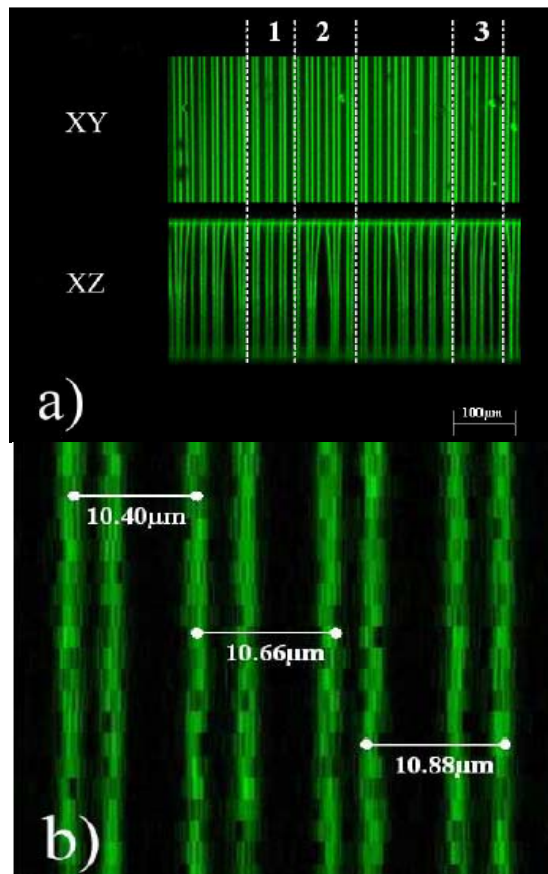


Figure 3.8 a). Comparison of the MgO:ppLN crystal surface view (XY) with the cross sectional view (XZ). Images were taken from the 3D reconstruction of the crystal obtained using MPLSM excited luminescence. **Figure 3.8 (b)** Close-up image taken from Column 1 in (a). Measurements of the crystal periodicity were easily obtained using Volocity 4 image analysis software.

In column 1 in Fig 3.8 a), near identical poling separation is observed in both the XY and XZ dimensions indicative of successful and precise fabrication. In column 2, the XY section shows aperiodicity near the surface of the device. This is reflected in the XZ section while highlights large changes in λ throughout the depth of the crystal. Importantly, when looking at the XY image for column 3, it appears that successful fabrication has been achieved. However when observing the XZ cross section, it is clear that internal deformation of the poling periods has occurred.

Regions of damage are also clearly visible within the XY section of columns 2 and 3 and also at other areas within the crystal. Furthermore, it is clear from the variation in

luminescence signal intensity at different regions of the crystal that the MgO dopant is inhomogeneous across the crystal, with higher dopant concentrations at the period boundaries in all cases. This is a consequence of the fabrication process, where the dopant migrates relative to the direction and strength of the electric field [24].

As well as obtaining visual information about the structure of the crystal, image analysis enables accurate measurement of the MgO:ppLN crystal period length, which contributes towards the performance of the structure for nonlinear frequency conversion. Figure 3.8(b) features a close-up image from Column 1 for close inspection of the luminescence excited within the crystal. Three measurements of the location of this high intensity luminescence signal were taken to illustrate the difference in periodicity within the crystal. The difference in periodicity was measured to be as large as $0.48\mu\text{m}$. Together, the lack of periodicity and the damage observed in Fig. 3.8(a) and Fig. 3.8(b) reduces the efficiency of the QPM process for nonlinear optical frequency conversion

3.4 Conclusion

This analysis highlighted the importance of imaging the internal structure of QPM crystals such as MgO:ppLN, since inspection of the near surface alone cannot give an accurate indication as to whether the fabrication process was successful. Near surface imaging can in fact be completely misleading, i.e. showing near perfect structures, yet having substantial deformation at depth. From this study, it has been shown that MPLSM provides important information from doped periodically poled materials that cannot be easily obtained via brightfield microscopy, CLSM or SHG LSM techniques. Using MPLSM, internal deformation of the crystal structure and dopant inhomogeneity can be identified at depth within thick samples, with sub-micron resolution. Such imaging could potentially be used as an inspection tool to aid in the fabrication and subsequent enhancement of the nonlinear characteristics of both MgO:ppLN and alternative QPM materials.

3.5 References

1. Myers, L.E. and W.R. Bosenberg, *Periodically poled lithium niobate and quasi-phase-matched optical parametric oscillators*, IEEE Journal of Quantum Electronics, 1997. **33**(10): p. 1663.
2. Lim, E., M. Fejer, R.L. Byer, W.J. Kozlovsky, *Blue light generation by frequency doubling in periodically poled lithium niobate channel waveguide*. Electronics Letters, 1989. **25**(11): p. 731.
3. Chen, Y.F., S.W. Tsai, S.C. Wang, Y.C. Huang, T.C. Lin, and B.C. Wong, *Efficient generation of continuous-wave yellow light by single-pass sum-frequency mixing of a diode-pumped Nd: YVO₄ dual-wavelength laser with periodically poled lithium niobate*. Optics Letters, 2002. **27**(20): p. 1809.
4. Myers, L.E., R.C. Eckardt, M.M. Fejer, R.L. Byer, W.R. Bosenberg, and J.W. Pierce, *Quasi-phase-matched optical parametric oscillators in bulk periodically poled LiNbO₃*. Journal of the Optical Society of America B, 1995. **12**(11): p. 2102-2116.
5. Sutherland, R.L., D.G. McLean, and S. Kirkpatrick, *Handbook of nonlinear optics*. 2003: Marcel Dekker.
6. Myers, L.E., R.C. Eckardt, M.M. Fejer, R.L. Byer, and W.R. Bosenberg, *Multigrating quasi-phase-matched optical parametric oscillator in periodically poled LiNbO₃*. Optics Letters, 1996. **21**(8): p. 591.
7. Bruner, A., D. Eger, M.B. Oron, P. Blau, M. Katz and S. Ruschin, *Temperature-dependent Sellmeier equation for the refractive index of stoichiometric lithium tantalate*. Optics Letters, 2003. **28**(3): p. 194.
8. Le Targat, R., J.J. Zondy, and P. Lemonde, *75%-efficiency blue generation from an intracavity PPKTP frequency doubler*. Optics Communications, 2005. **247**(4-6): p. 471.
9. Bryan, D.A., R. Gerson, and H.E. Tomaschke, *Increased optical damage resistance in lithium niobate*. Applied Physics Letters, 1984. **44**(9): p. 847.
10. Iyi, N., K. Kitamura, Y. Yajima, S. Kimura, Y. Furukawa and M. Sato, *Defect Structure Model of MgO-Doped LiNbO₃*. Journal of Solid State Chemistry, 1995. **118**(1): p. 148.

11. Kim, H.W., S.H. Shim, and J.W. Lee, *Growth of MgO thin films with subsequent fabrication of ZnO rods: Structural and photoluminescence properties*. Thin Solid Films, 2007. **515**(16): p. 6433.
12. Zhang, J. and L. Zhang, *Intensive green light emission from MgO nanobelts*. Chemical Physics Letters, 2002. **363**(3-4): p. 293.
13. Dierolf, V. and C. Sandmann, *Inspection of periodically poled waveguide devices by confocal luminescence microscopy*. Applied Physics B: Lasers and Optics, 2004. **78**(3): p. 363.
14. Nakamura, K., J. Kurz, K. Parameswaran, and M.M. Fejer, *Periodic poling of magnesium-oxide-doped lithium niobate*. Journal of Applied Physics, 2002. **91**(7): p. 4528.
15. Rosenfeldt, A. and M. Flörsheimer, *Nondestructive remote imaging of ferroelectric domain distributions with high three-dimensional resolution*. Applied Physics B: Lasers and Optics, 2001. **73**(5): p. 523.
16. Dierolf, V. and C. Sandmann, *Direct-write method for domain inversion patterns in LiNbO₃*. Applied Physics Letters, 2004. **84**(20): p. 3987.
17. Boyd, R., *Nonlinear optics*. 2008: Academic Press.
18. Uesu, Y., H. Yokota, S. Kawado, J. Kaneshiro, S. Kurimura, and N. Kato, *Three-dimensional observations of periodically poled domains in a LiTaO₃ quasiphase matching crystal by second harmonic generation tomography*. Applied Physics Letters, 2007. **91**(18): p. 182904-3.
19. Kaminacuteska, A., J.E. Dmochowski, A. Suchocki, J. Garcia-Sole, F. Jaque, and L. Arizmendi, *Luminescence of LiNbO₃:MgO,Cr crystals under high pressure*. Physical Review B, 1999. **60**(11): p. 7707.
20. Wokosin, D.L., V.E. Centonze, S. Crittenden, J. White, *Three-photon excitation fluorescence imaging of biological specimens using an all-solid-state laser*. Bioimaging, 1996. **4**(3): p. 208.
21. Denk, W., J. Strickler, and W. Webb, *Two-photon laser scanning fluorescence microscopy*. Science, 1990. **248**(4951): p. 73.

22. Moutzouris, K., F. Sotier, F. Adler and A. Leitenstorfer, *Highly efficient second, third and fourth harmonic generation from a two-branch femtosecond erbium fiber source*. Optics Express, 2006. **14**(5): p. 1905.
23. Powers, P., T.J. Kulp, and S. Bisson, *Continuous tuning of a continuous-wave periodically poled lithium niobate optical parametric oscillator by use of a fan-out grating design*. Optics letters, 1998. **23**(3): p. 159.
24. He, X. and D. Xue, *Doping mechanism of optical-damage-resistant ions in lithium niobate crystals*. Optics Communications, 2006. **265**(2): p. 537.

Chapter 4 Comparison of single-pass, double-pass and bi-directional pump geometries for improved efficiency synchronously pumped optical parametric oscillators

4.1 Introduction and motivation

Since the development and widespread application of two photon excitation microscopy during the 1990's, it has become an important and versatile tool for many laboratories. As described in Chapter 1, benefits of two photon excitation include deeper sample penetration, increased cell viability and reductions in photo-bleaching. Applications of this technique include deep tissue imaging [1, 2], label-free imaging [3, 4] and within materials analysis [5, 6].

It had been previously shown by Szmackinski *et al* that the emission wavelength from a fluorophore is independent of the number of photons used to excite the molecule [7]. Therefore, three photon excitation can be a feasible technique for fluorescence imaging of standard fluorophores, if the correct excitation wavelength is applied, whilst enhancing the advantages of two photon imaging.

In a study by Lakowicz *et al*, both two photon and three photon excitation of DNA labelled with DAPI and Hoechst 33342 was demonstrated with use of a ultra-short pulsed laser [8]. Within this study it was highlighted that the necessary increase in peak power required for three photon excitation did not result in adverse effects due to excessive heating or dielectric breakdown being incurred [7]. Hence the applicability of three photon excitation to biological samples was highlighted.

In 1996, Hell *et al* conducted the first fluorescence imaging based upon three photon excitation [9]. This involved excitation of UV excitable beads and was found to

increase axial resolution, when comparing to two photon excitation. Others have demonstrated the use of three photon excitation including Wokosin *et al*, who highlighted the possibility for simultaneously achieving both two and three photon excitation simultaneously [10]. This provided a source which could simultaneously excite fluorescence from multiple dyes over combined emission spectra covering the entire visible range.

Within the field of life sciences, continuously tunable ultra-short pulsed sources of coherent radiation are a highly desirable asset, as they provide microscopists with a versatile source which is tailored to their specific needs [11-13]. As described in Chapter 1, the majority of commercial microscopy systems provide only a few fixed wavelengths for sample illumination (e.g. discrete lines from a Helium-Neon or Argon ion laser). With specific reference to fluorescence microscopy, each fluorophore has its own specific peak excitation wavelength. Therefore efficient excitation is unlikely to be obtained when using fixed sources. This can lead to thermal loading that can be damaging to biological samples and also poor contrast images are likely to be observed [14].

There are alternatives to these fixed sources in the form of tunable lasers. Such lasers include the popular Ti:Sapphire and various dye lasers. These systems provide a continuously tunable output which is obtained as a result of stimulated emission between energy levels in a laser gain medium which has an extended fluorescence bandwidth [15]. While these lasers provide excellent sources of coherent radiation, spanning over various spectral ranges, they tend not to extend beyond the visible and near infra-red [16]. Therefore tunable, longer wavelength sources of coherent radiation are required. Optical parametric oscillators offer a solution to this technology limitation.

This chapter looks to address the challenges of applying optical parametric oscillators to microscopy platforms and address these issues through laser development.

4.1.1 Historical review of optical parametric oscillators

Following from theoretical discussions by Kroll and Armstrong [17, 18] regarding the possibility of parametric amplification and oscillation within a nonlinear medium, Giordmaine and Miller constructed the first optical parametric oscillator in 1965 [19]. The OPO that they constructed was a LiNbO₃ crystal pumped by a pulsed Nd⁺³:CaWO₄, which had been frequency doubled to provide a pump source at 529 nm. The output from this system was tunable over a wavelength range of 970 – 1150 nm.

In 1968, Smith *et al* performed an experiment where the output from a cw Nd:YAG laser was used to pump a Ba₂NaNb₅O₁₅ crystal [20]. This experiment highlighted the possibility for OPOs to be generated with a continuous output. Another important development was that of Byer *et al* who produced a visible cw OPO which was wavelength tunable between 680 – 705 nm, whilst providing a threshold ten times lower than previously observed [21]. Despite the advantage of a low threshold, nonlinear optical frequency conversion efficiencies for cw lasers tend to be low (~1 % in the two previous cases). In order to achieve greater nonlinear optical frequency conversion efficiency, higher peak powers are required.

Ultra-short pulsed lasers provide an excellent source for the production of high peak power pulses. Implementing an ultra-short pulsed laser as a pump source and by employing a technique known as synchronous pumping, an ultra-short pulsed output with high conversion can be obtained with high conversion efficiency. Synchronous pumping is the process of matching the pump cavity round trip time to that of the OPO cavity. One of the first instances where this was implemented was in work by Burneika *et al* [22]; here it was shown that signal pulses could be obtained with a pulse duration of 10⁻¹³ s. Synchronous pumping of OPOs allowed for the generation of high peak powers over the wide tuning range which they can support. Moreover this paper demonstrated the asymmetry of the output power's dependence on OPO

cavity length. The drop in power at de-synchronisation is a result of undepleted gain resulting from poor overlap of the pump and signal pulses. The asymmetry arises from the group velocity difference between the pump and generated frequencies. As a result one direction of detuning results in compensation for the difference in group velocity, and the other further extends this difference [23]. A theoretical analysis for the synchronous pumping of OPOs was later provided by Becker et al [24].

4.2 Optical parametric processes

Despite the wide range of laser gain materials which are currently available, and the various laser transitions these media can cover, many of these are not found at useful frequencies for microscopy purposes. Therefore methods for shifting standard laser frequencies to those which are required have been developed. Various nonlinear frequency conversion techniques are available to induce these shifts in wavelength including harmonic generation along with sum- and difference- frequency generation. One of the serious draw backs of these processes is that the output frequency is solely dependent upon the frequencies of the input beams. One technique which overcomes this problem is the parametric process; which can be implemented to provide a continuously tunable source from a single frequency input beam.

The parametric process may be illustrated by a Feynman diagram as seen in Fig. 4.1. This describes an incoming pump photon with energy $\hbar\omega_1$ and wave vector k_1 , subject to spontaneous parametric down conversion. This results in the generation of two lower energy photons with energy equal to $\hbar\omega_2$ and $\hbar\omega_3$, which are termed signal and idler respectively, with $\hbar\omega_2 > \hbar\omega_3$.

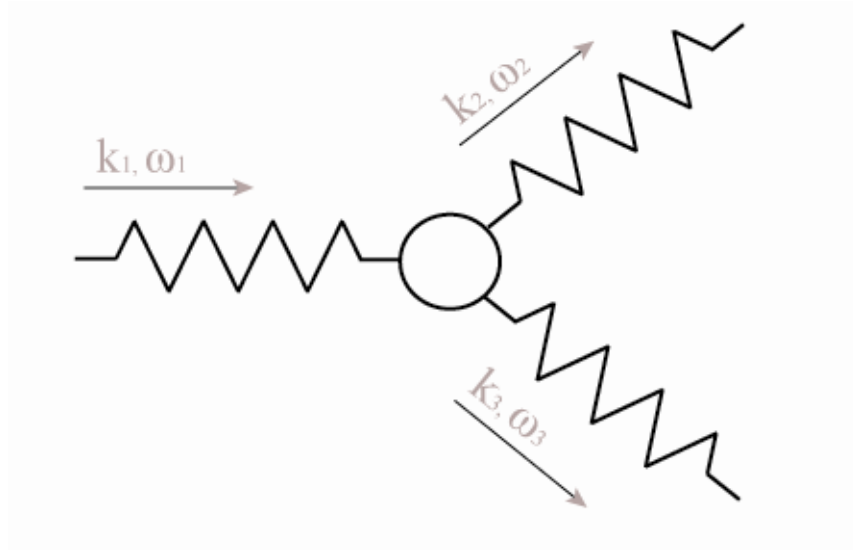


Figure 4.1 Spontaneous parametric down conversion of a pump photon resulting in the generation of a signal and idler photon.

The breakdown of the pump photon to the signal and idler is governed by the principles of conservation of energy

$$\omega_1 = \omega_2 + \omega_3 \quad (4.1)$$

and conservation of momentum

$$k_1 = k_2 + k_3. \quad (4.2)$$

As a result of the frequency condition in Eq. (4.1), it can be seen that (unlike harmonic generation, sum- and difference-frequency generation) the parametric process does not provide two unique frequencies for any given pump frequency.

In a non-dispersive medium, Eq. (4.1) and (4.2) may be satisfied by a continuous range of frequencies, hence providing the wavelength tunability which is characteristic of parametric interactions. Of course, propagation of photons through a nonlinear material will result in dispersion. This may be compensated for with use of birefringent crystals and the application of phase matching, which is described in general terms in Chapter 2.6. In spite of the application of phase matching to spontaneous parametric breakdown, efficiency for the generated frequency tends to be low [25].

4.2.1 Optical parametric amplification

For the case of spontaneous parametric emission, the pump photon is the only frequency present in the initial state. However in the event that both a pump and a signal photon are present, stimulated parametric emission can occur. This is a similar process as to the stimulated emission exhibited by a laser, but no population inversion induced within the medium; signal and idler photons are generated directly through the nonlinear response of the medium.

This process is also known as optical parametric amplification (OPA). The induced amplification of the generated frequencies is incurred by a repetitive difference frequency generation based upon the interaction between the pump and signal. This results in the generation of the idler and from this, greater amounts of the signal, since the process is repeated (for the phase matching condition).

The parametric gain G , incurred upon propagation through a nonlinear crystal of length L , can be defined by the following

$$G = \frac{P_s(L)}{P_s(0)} - 1 = (\Gamma L)^2 \frac{\sinh^2\left(\sqrt{(\Gamma L)^2 - (\Delta k L / 2)^2}\right)}{(\Gamma L)^2 - (\Delta k L / 2)^2}, \quad (4.3)$$

where $P_s(0)$ and $P_s(L)$ represent the signal power at the input and output of the nonlinear crystal. In order to obtain high conversion efficiency, one of the key parameters resulting in high values of G is the gain coefficient Γ

$$\Gamma = 4\pi d_{eff} \sqrt{\frac{I_p(0)}{2\varepsilon_0 n_1 n_2 n_3 c \lambda_2 \lambda_3}}, \quad (4.4)$$

where $I_p(0)$ is the initial pump intensity.

4.2.2 Optical parametric oscillation

Despite the increased efficiency experienced when using an OPA, the gain remains moderate even at high pump intensities. One method which can be used to increase this is through the introduction of feedback into the crystal. A particularly useful method for achieving this is through the introduction of two mirrors at either end of the nonlinear medium to create a resonator. Despite the occurrence of parametric amplification at all levels of pump power, oscillation only occurs above a specified threshold. This threshold is defined as the pump power at which the induced parametric gain exceeds losses within the resonator. At and above this power, resonant waves will grow dramatically. This system is known as an OPO. These are typically found in two forms; singly resonant (SRO) and doubly resonant (DRO) and are illustrated in Fig. 4.2.

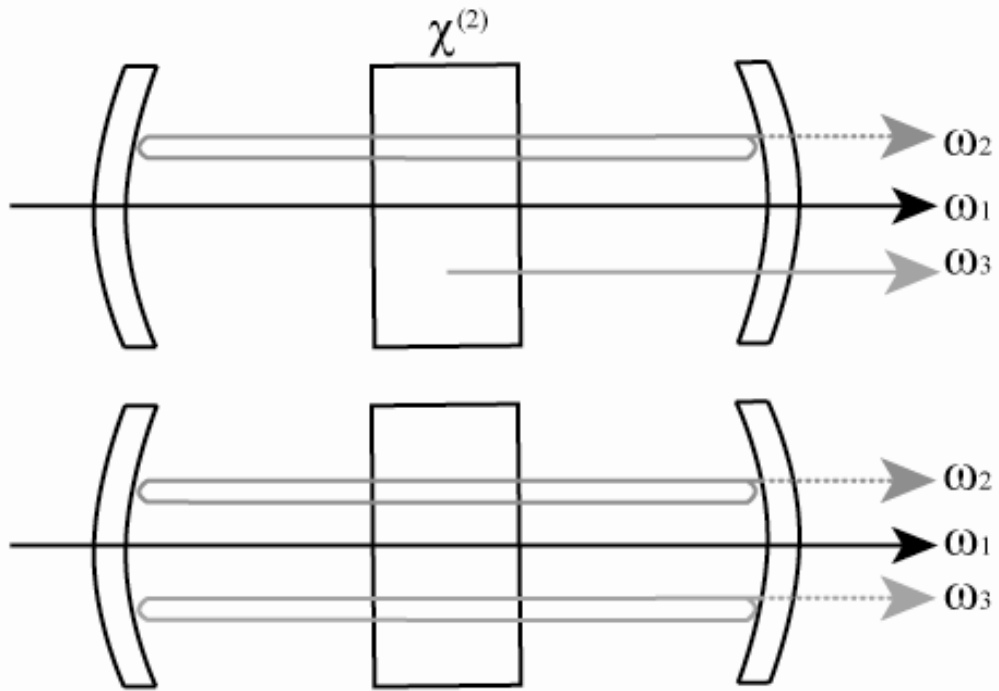


Figure 4.2 Geometries of OPO operation. Above; SRO, only one of the frequencies are resonated within the cavity. Below; DRO, two of the interacting frequencies are resonated. The spatial separation between beams is shown for ease of description, in practice, all beams are overlapped.

4.2.2.1 Singly resonant oscillation

The most straight-forward case for achieving parametric oscillation is obtained by resonating a single frequency (either signal or idler) with use of highly reflecting mirrors at this frequency. If the case is considered where the signal frequency ω_2 is resonant, any change in the resonant cavity modes is coupled with a corresponding change in the idler frequency ω_3 in order to satisfy energy conservation. This results in the continuously tunable output which is characteristic of SROs.

Unlike a laser which experiences gain upon each pass through the gain medium, parametric gain is only achieved when the signal and pump beams propagate in the same direction through the nonlinear medium. This is the case because the DFG process described in Section 4.2.1. is not a phase matched interaction. For a SRO the

steady state threshold is determined when the round trip loss of the resonated beam equals the single pass gain through the crystal and for low loss systems may be described by the following [26]

$$(\Gamma L)_{th}^2 = 2[1 - R_2 \exp(-\alpha_2 L)], \quad (4.5)$$

where R_2 is the total reflectance of the cavity mirrors at the signal frequency and α_2 is the corresponding absorption coefficient.

With use of the plane wave approximation, the threshold can be described in terms of pump power

$$P_{th} = A \frac{\epsilon_0 n_2^2 n_1 c \lambda_1^2}{\pi^2 d_{eff}^2 L^2 (1 - \delta^2)} (1 - R_2 e^{-\alpha_2 L}), \quad (4.6)$$

where A is the beam area and δ is the degeneracy factor described as follows

$$\delta = \frac{2\omega_2}{\omega_1} - 1. \quad (4.7)$$

When operating above threshold, conversion efficiency η and output signal power P_2 may be determined using the following relationship

$$\eta = \sin^2 \Gamma, \quad P_2 = \frac{\lambda_1}{\lambda_2} \left(\frac{1 - R_2}{1 - R_2 + \alpha_3 L} \right) \eta P_1(0). \quad (4.8)$$

4.2.2.2. Doubly resonant oscillation

An alternative geometry to the SRO is the application of a DRO. In this case both the signal and idler frequencies are resonated within the OPO cavity. This is achieved by using cavity mirrors which are highly reflecting at both of these frequencies. This method of conversion can be advantageous in some respects, yet have disadvantages in others.

Using the same methods as those in the SRO case above, the oscillation threshold under the conditions of low loss, may be defined as

$$(\Gamma L)_{th}^2 = [1 - R_2 \exp(-\alpha_2 L)][1 - R_3 \exp(-\alpha_3 L)] \quad (4.9)$$

where R_3 and α_3 are the total reflectance of the cavity mirrors and absorption coefficient respectively for the idler frequency. This corresponds to an input pump power threshold of

$$P_{th} = A \frac{\epsilon_0 n_2^2 n_1 c \lambda_1^2}{2\pi^2 d_{eff}^2 L^2 (1 - \delta^2)} (1 - R_2 e^{-\alpha_2 L})(1 - R_3 e^{-\alpha_3 L}) \quad (4.10)$$

If these DRO threshold conditions are compared to those for SROs given in Eq. (4.5) and (4.6), it is found that the threshold of an SRO is larger by a factor of $2/[1 -$

$R_3 \exp(-\alpha_2 L) J$. Therefore the required pump levels to obtain oscillation in DROs are much lower than those required for an equivalent SRO. This is of particular use for cw OPOs whereby the high average powers required in SROs can cause damage to the integrity of the nonlinear medium.

Despite the advantage of reduction in oscillation threshold, DROs have notoriously difficult spectral control due to the requirement of the generated frequencies to satisfy conservation of energy and momentum whilst meeting the resonance condition. This often leads to the fluctuations in the output power along with discontinuous wavelength selection [27].

It is of note that it is also possible for an OPO to be resonant at the signal, idler and pump frequencies [28, 29]. These systems are triply resonant and can provide exceptionally low pump thresholds (< 1 mW). The problems with meeting the conservation of energy and momentum along with the resonance conditions for three frequencies are however very difficult to overcome and the resulting output can be unstable with poor tuning attributes [30].

4.3 Optical parametric oscillator design

In order to utilise an OPO for a specific application, care must be taken with various parameters which determine the output provided by the system. This section looks to provide an overview of the important considerations involved when designing an OPO. Due to the reasons of stability and the characteristic continuous tunability which is available with SROs, as discussed in the previous section, single frequency resonance was selected for this OPO.

As this system was designed for application in three-photon microscopy, there are characteristics of the output which are required. Firstly, high peak power is required in order to induce simultaneous absorption of three photons by a fluorophore. Secondly, this source is required for application to biological samples which use standard fluorescent labels, many of which are excitable in the visible region. Therefore, a wavelength tuning range of $\sim 1.4 - 1.6 \mu\text{m}$ was desirable. Care must also be taken when considering the repetition rate of a source used for fluorescence techniques due to the danger of saturation and bleaching effects [31].

4.3.1 Synchronously pumped optical parametric oscillators

Mode-locked lasers have been used extensively and successfully throughout life science applications. Mode-locked sources which cover the near- to mid-IR are however limited. Use of a synchronously pumped optical parametric oscillators (SPOPO) can address this gap in spectral coverage and in order achieve the properties of a mode-locked laser. Synchronous pumping occurs when the round trip time for an OPO cavity is matched to the round trip time for the pump laser. When this is the case, pump pulses are ensured to arrive within the nonlinear crystal at the same time as each resonating signal pulse, leading to amplification. With application to this technique, mode-locked lasers provide excellent pump sources for a SPOPO. Their high peak power allows for high gain and low average power can alleviate damage to the nonlinear medium.

The temporal behaviour of the signal electric field E_2 for repetitive pulses within a steady-state SPOPO has been described by Chung and Liu [32]. Here they highlighted that $E_2(t)$ can be governed by the following differential equation

$$\left[G(t) - L(t) + \delta T \frac{d}{dt} + \frac{1}{\omega_c^2} \frac{d^2}{dt^2} \right] E_2(t) = 0, \quad (4.11)$$

where $G(t)$ and $L(t)$ and the respective total round trip electric field gain and loss. The term δT is the cavity detuning time and is determined by the difference between the pump pulse repetition time and the round trip time of the signal pulses. The cavity bandwidth ω_c is a factor based upon the frequency selective properties of the cavity elements.

4.3.1.1 Pump lasers for SPOPOs

Selection of a pump laser for SPOPOs is critical in order to tailor the output of the device. Pump attributes such as beam quality, average power, pulse duration and repetition rate all play an important role in the output of the SPOPO.

Often the quality of a laser beam is defined by a single M^2 value. To determine the M^2 of a beam, the beam parameter product (BPP) must firstly be calculated. This can be found from the product of the divergence angle and the beam waist of a focused beam. This must be calculated for the measured laser (BPP_1), and then compared to that of similarly focused a Gaussian beam (BPP_0)

$$M^2 = \frac{BPP_1}{BPP_0} = \frac{(\lambda w_1 / \pi w_0)}{(\lambda w_0 / \pi w_0)} = \frac{w_1}{w_0}, \quad (4.12)$$

where w_0 and w_1 are the respective beam waists for the laser and that of a Gaussian beam. Typically the M^2 value is given for both the x and y axes of the beam. It is not only useful in determining how closely a beam follows the behaviour of a Gaussian,

but also highlights how closely to the diffraction limit a beam may be focused. This in turn plays a factor in the resolution of a laser excitation imaging system. In practice, lasers have an $M^2 > 1$ and this is used as a measure of the ‘quality’ of the laser.

As was seen from Eq. (1.6) in Chapter 1, the number of multiphoton events which occur is strongly dependent upon the peak intensity of the excitation beam. Therefore it is strongly desirable that the pump source provides modelocked, ultra-short pulses. In combination with the synchronous pumping mechanism described in the previous section, this results in the generation of ultra-short pulses with the wavelength tuning properties of a SPOPO. It is also important to consider the repetition rate of the pump source as this will in turn be mimicked by the SPOPO. Following excitation, fluorophores have a typical relaxation time of less than 10 ns. In order to avoid fluorophore saturation, the interval between laser pulses should not be shorter than this [14].

Examples of typical pump sources which have previously been used for SPOPOs are presented in Table 4.1.

Pump source	Crystal	Average output power	Tuning range	Pulse width	Ref
Rhodamine 6G dye laser (620 nm, τ =170 fs, 100 MHz)	KTP	2 mW	820 – 920 nm	220 fs	[33]
Mode-locked Ti:Al ₂ O ₃ (765 nm, τ =110 fs, 76 MHz, 800 mW)	KTP	185 mW	1.2 – 1.34 μ m	62 fs	[34]
Nd:YLF (1064 nm, τ =406 fs, 120 MHz)	PPLN	130 mW	1.45 – 1.63 μ m	450 fs	[35]

MHz, 500 mW)					
Nd:YAG (1064 nm, 10 ps, 120 MHz)	AgGaS ₂	~ 200 mW	2.5 – 4.0 μm	500 fs	[36]

Table 4.1 Table of commonly used pump sources for fs-pulse SPOPOs

The Ti:Sapphire source is of particular interest, as due to its ultra-short pulses and tunability in the near infrared (NIR), this system is already widely used for MPLSM and is therefore existing in many research labs. With this inherent wavelength tuning coupled with the tuning provided by a SPOPO, a single source can cover a very broad spectral range. However the prices of these systems are often beyond the reach of many microscopy labs.

An alternative to this is through the use of fibre lasers as a pump source. Fibre lasers implement a silica optical fibre which is doped using rare earth elements such as Ytterbium, Erbium and Neodymium. These materials provide the gain medium which generates the laser output. The fibre is typically optically pumped using a diode laser or with use of another fibre laser. This can be coupled into the core of the fibre and the waveguide confines the beam and allows fluorescence to be generated throughout the fibre. As gain is only experienced in the core of the fibre, these tend to be high quality lasers with M^2 values close to unity.

The laser cavity within a fibre laser is created by fabricating Bragg gratings within the fibre. These gratings are created by having periodic changes in the refractive index of the fibre. This allows a chosen wavelength to be reflected, allowing for optical feedback which is typical for a laser system.

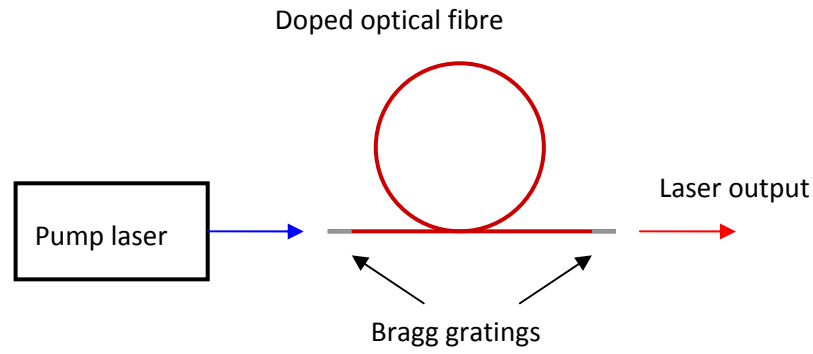


Figure 4.3 Typical setup for a fibre laser.

Additionally, these lasers can provide high output powers, and may be pulsed using either passive or active mode-locking techniques previously described in Chapter 1. As a result, these fibre lasers can support ultra-short pulse generation and provide repetition rates suitable for applications in fluorescence microscopy. At a fraction of the cost of a Ti:Sapphire laser, with high peak output powers and excellent stability, fibre lasers represent a very attractive pump source for SPOPOs.

4.3.2 Crystal selection

When selecting an appropriate $\chi^{(2)}$ nonlinear crystal for SPOPO, quality, availability and price are obvious considerations before selection. There are however many other critical technical factors which need to be taken into account, in order to benefit from the many crystal specific attributes which are available.

As described in Chapter 2, the effective coefficient d_{eff} may be used to quantify the nonlinear susceptibility of a given crystal. For high levels of nonlinear conversion, this parameter is required to be as large as possible.

Crystal transparency for interacting wavelengths is also an important consideration for nonlinear processes. Any linear absorption incurred will lead to heating and can lead to thermal lensing, disrupting the phase matching process.

The damage threshold of a material is also of importance as some materials will exceed the damage threshold prior to most conversion levels. In some cases, materials may be doped in order to increase the tolerance of the crystal to optical damage; such is the case for LiNbO_3 , which is often doped with MgO.

	LBO	BBO	KTP	PPLN
d_{eff} [pm/V]	1.16	1.94	3.64	17.2
Transparency [μm]	0.16 – 2.6	0.19 – 2.5	0.4 – 4.0	0.5 – 6
Damage threshold [GW/cm^2]	2.5	1.5	0.5	4

Table 4.2 Summary of common crystals employed for OPOs

Table 4.2 provides a list of the discussed properties of various common nonlinear optical crystals used in SPOPO systems. A high d_{eff} value of 17.2 pm/V can be achieved as a result of the periodic poling, described in Chapter 2.7, which allows the pump beam to be propagated in the direction of the highest nonlinear index for lithium niobate. By having a wide range of transparency and high damage threshold, PPLN becomes a very desirable medium for SPOPOs operating in the near- to mid-IR.

4.3.3 Wavelength control

As described in Section 4.2, the output wavelengths from a SPOPO are determined by the phase matching conditions of the system. With reference to conservation of

energy and momentum, changes to the pump source may be used to alter the output frequencies of the signal and idler photons. However in the event that a fixed wavelength source is used, alternative methods of tuning are available. These methods are applied via temperature control of the nonlinear crystal, period length selection or through cavity length de-tuning. As was seen from Eq.(2.5), the temperature-dependent Sellmeier equation illustrates how accurate temperature control of the nonlinear crystal can lead to a continuously tunable output for the signal and idler frequencies.

By plotting output wavelengths as a function of temperature using the Sellmeier equations using the nonlinear crystal modelling program SNLO; theoretical predictions for the tuning range of the signal and idler wavelengths can be shown in Fig. 4.4.

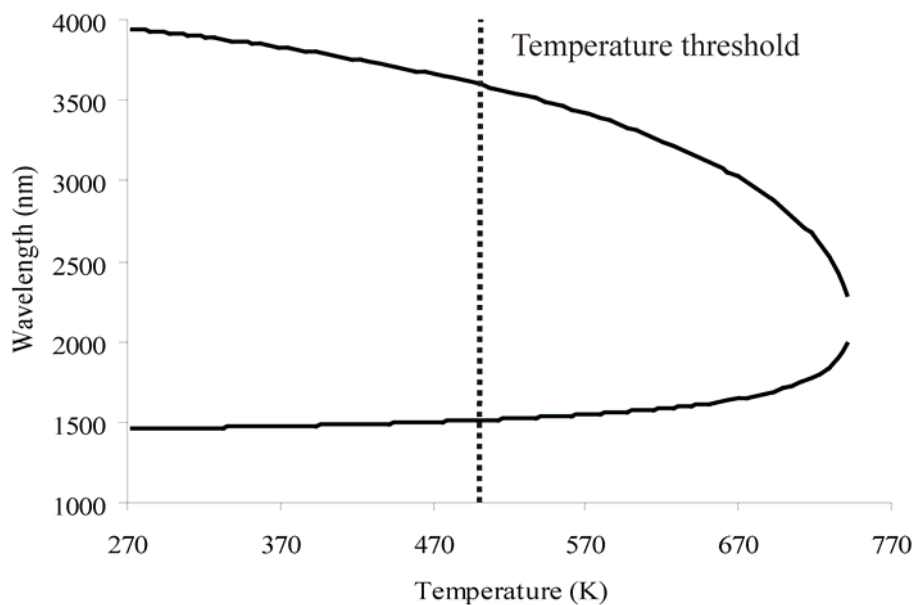


Figure 4.4 Theoretical wavelength tuning curves for varying temperature at a constant pump wavelength and crystal period length. Resulting from predicted outputs in SNLO, based upon the temperature dependent Sellmeier equation.

The above situation demonstrates the tuning achieved when using a 1064 nm pump source in a singly resonant, PPLN SPOPO, with a fixed period length of 29.3 μm .

For completeness, a temperature tuning range is shown to a point where the OPO reaches degeneracy. In practice, this temperature exceeds the thermal damage limit for PPLN which is approximately 500 °K. Additionally the integrity of the crystal oven would likely be compromised at these temperatures due to the melting point of solder (~ 450 °K).

Again, by with analysis of the Sellmeier equation for QPM crystals, it is seen that there is a dependence on length of poling period, Λ . During the manufacturing stage of a crystal, it is possible to produce crystals which have alternative period lengths depending upon the vertical positioning on the crystal. This can either be in a grating or fan structure. As various periods can be selected, this provides an additional method to meet the phase matching condition and therefore wavelength tuning.

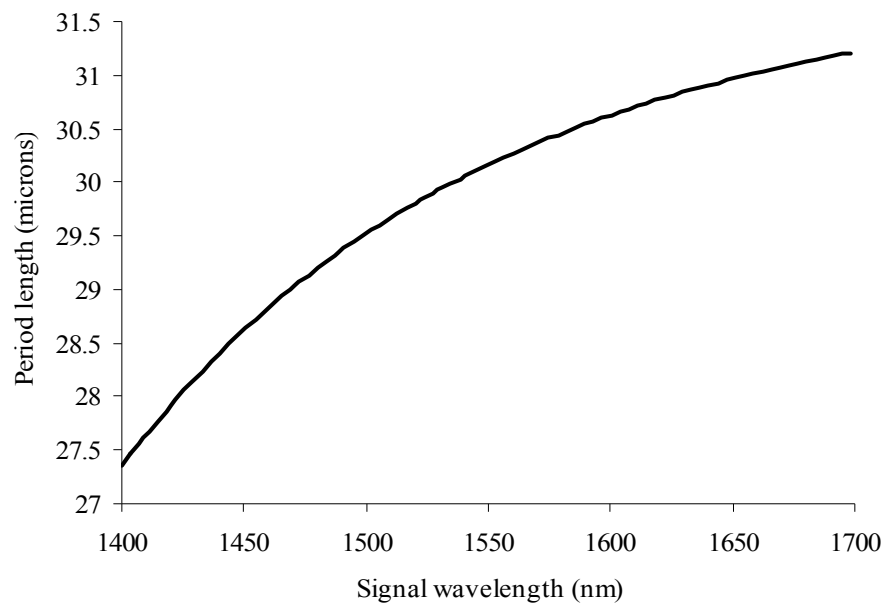


Figure 4.5 Theoretical signal wavelength tuning curve with period length at a fixed temperature of 373 °K and pump wavelength of 1064 nm.

Figure 4.5 shows theoretically, that for a fixed temperature of 373 °K, and pump wavelength of 1064 nm, a period lengths of 27 – 30 μm provides an equivalent signal output of approximately 1400 – 1600 nm. This was the desired wavelength for the three photon excitation imaging which was the intended application for this source.

4.3.4 OPO cavity design

The OPO cavity plays a vital role in the characteristics of the generated output, including contributions to the average power, pulse duration and even the generated spectrum. When considering coupling of pump light into a SPOPO resonator, there are various requirements which need to be fulfilled to ensure optimal efficiency.

When focusing light into a nonlinear crystal, the beam waist of the pump source is a key factor to achieving the high intensities required for nonlinear interactions and in the output efficiency of the system. In 1968, Boyd and Kleinman presented a focusing parameter ξ , which for optimal conversion should yield a value of 2.84 [37]. This was derived from theoretical value for optimal output with variation of ξ

$$\xi = \frac{L}{b}. \quad (4.13)$$

Here, L is the crystal length, and b is the confocal parameter,

$$b = \frac{2\pi n w_0^2}{\lambda_0}. \quad (4.14)$$

Combination of Eq. (4.13) and (4.14), whilst introducing the optimal focusing parameter, yields an equation from which the beam waist w_0 , which produces the maximum output power may be calculated

$$w_0^2 = \frac{l\lambda_0}{5.68\pi m}. \quad (4.15)$$

When seeking to achieve efficient nonlinear optical frequency conversion, it is also very important to ensure that a pump beam provides good spatial overlap within the SPOPO resonator. This is known as mode matching, as one looks to match the resonator axial modes to the profile of the incoming pump beam. A good overlap ensures efficient transfer of energy from the pump to the signal wavelength.

When designing a laser system based on a Gaussian beam, it can be effectively described by using a “q-parameter”. This is a complex parameter which describes both the beam size and the curvature of the wavefront at a given point z . The Gaussian beam size $w(z)$, can be described using Eq. (4.16)

$$w(z) = w_0 \sqrt{1 + \left(\frac{z_0}{a}\right)^2}. \quad (4.16)$$

The curvature of the wavefront $R(z)$ is described by

$$R(z) = z \left[1 + \left(\frac{z_0}{z} \right)^2 \right]. \quad (4.17)$$

Using these relations, it is then possible to calculate a value for the q-parameter, $q(z)$

$$\frac{1}{q(z)} = \frac{1}{R(z)} + i \frac{\lambda}{\pi w^2(z)}. \quad (4.18)$$

SPOPO resonators may be designed using beam modelling programs such as WinLase. This software uses the above equations combined with the theory of ABCD matrix multiplication in order to model beams within a cavity. ABCD matrices allow complex optical systems to be portrayed as the product of a series of 2 x 2 matrices unique to each element. Upon interaction with each matrix, the initial q-parameter q_1 , is converted to q_2 with use of the ABCD law

$$q_2 = \frac{Aq_1 + B}{Cq_1 + D}. \quad (4.18)$$

This value q_2 represents the Gaussian beam following interaction with a given optical element.

Where the signal wavelength serves as the useful output, singly resonant cavities have end mirrors which are designed to be highly reflective at the signal wavelength, with the exception of the output coupler. The reflectivity of this mirror should be chosen in order to extract the highest output power from the cavity. The technique which is used for efficient extraction is known as impedance matching and ensures

that maximum electric field transfer is achieved. This condition is achieved by matching the input coupler's transmission to the sum of all of the losses incurred inside the resonator. A zero lens input coupler can be used in order to ensure that the pump beam is not deformed upon coupling into the resonator, although optical loss will be incurred. Both pump and idler beams should be transmitted through cavity end mirrors and will not be resonated.

A linear cavity was selected due to its unidirectional output coupled with the straightforward synchronous pumping possibilities. An alternative to this linear cavity is the ring resonator, which is more difficult to align. The ring cavity does provide gain upon every pass through the crystal, unlike that seen in a linear cavity which typically experiences gain in a single direction. Appropriate considerations of linear cavity pumping geometries, can address this disadvantage, as will be discussed in the following sections.

4.4 Experiment

4.4.1 Single pass pumping SPOPO

Conventionally, synchronously pumped singly resonant SPOPOs are pumped in a single direction. With reference to the coupled amplitude equations, amplification of the resonating signal wavelength pulse occurs within an SPOPO crystal when both the pump and signal pulses are present and temporally overlapped. Therefore, a single pass geometry allows amplification of the signal upon propagation through the crystal, in the forward direction.

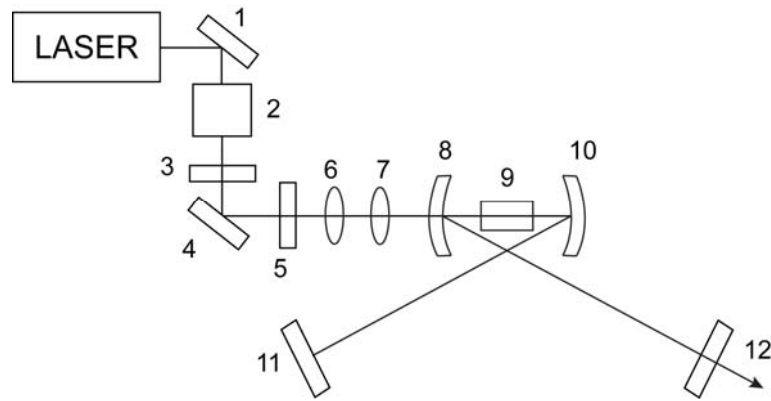


Figure 4.6 A singly resonant, single pass pumped SPOPO

Figure 4.6 gives a system diagram of the components required for a single pass pump geometry for a synchronously pumped SPOPO.

Component	Description
1	Beam steering mirror (HR @ 1064 nm)
2	Faraday isolator (30 dB)
3 & 5	Half-wave plates
4	50/50 beam-splitter
6 & 7	Spherical lenses ($f = 35$ mm and 63 mm, AR coated @ 1064 nm)
8 & 10	Zero lens curved mirrors (ROC = 100 mm, HR @ 1.4 – 1.6 μm)
9	PPLN crystal stored within a home-built oven (3 mm long, 1 mm thick)
11	Cavity end mirror (HR @ 1.4 – 1.6 μm)
12	Output coupler (50% reflection @ 1.4 – 1.6 μm)

Table 4.3 List of optical components described in Fig. 4.6

A Femtopower-fs-2 system (Fianium) was selected as the pump source for this SPOPO due to the benefits described in section 4.3.1.1.

The pump source output is the result of four main components. The first of which is a mode locked, low power master source. This was followed by a pre-amplifier, high-power polarization-maintaining cladding pumped, fibre amplifier, and then finally a pulse compression unit.

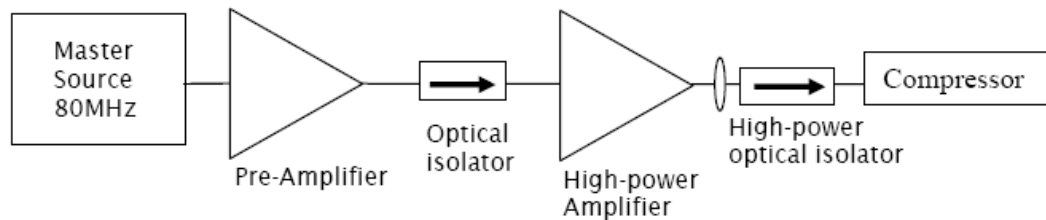


Figure 4.7 Yb-doped fibre laser components

The master source was a passively mode locked fiber laser based on a core-pumped, Ytterbium doped fibre providing pulses ~ 3 ps at a repetition rate of 80 MHz. The passive mode locking of the laser was achieved with use of a semiconductor saturable absorber mirror (SESAM).

An amplifier chain, such as that described in figure 4.7, can be used to provide higher performance than that of a single amplifier. That is, when considering the pre-amplifier, gain efficiency is preferred to be high – requiring the mode area to be small. Conversely the high-power amplifier requires a larger mode size in order to reduce nonlinearities and remain below damage thresholds. Hence individual elements are preferred. The high power amplifier was a double-clad Yb-doped fibre and was air cooled to reduce the temperature of the pump’s heat sink.

This Yb-doped fibre laser provided a fixed wavelength $\lambda = 1064$ nm, average power $P_{av} \sim 2$ W, pulse duration $\tau_p \sim 250$ fs, repetition rate $\Delta\nu = 80$ MHz, an $M^2 = 1.17$ and spectral width of $\Delta\lambda = 12$ nm.

As the output pulse duration provided from a SPOPO typically matches that of the mode-locked pump source, resultant peak powers yet moderate average powers from the SPOPO allows the source to be considered for inducing multiphoton absorption within samples. The high beam quality provided by the pump source also tends to be mimicked by a SPOPO [38], resulting in close to diffraction limited focusing. With a repetition rate of 80 MHz, this corresponds to an interval between pulses of 12 ns, which is also suitable for applications in fluorescence microscopy.

Directly following the pump source, a Faraday isolator was implemented into this system to remove optical feedback from entering the pump laser (this can often disrupt mode-locking). The isolator is comprised of three components; two polarisers and a Faraday rotator.

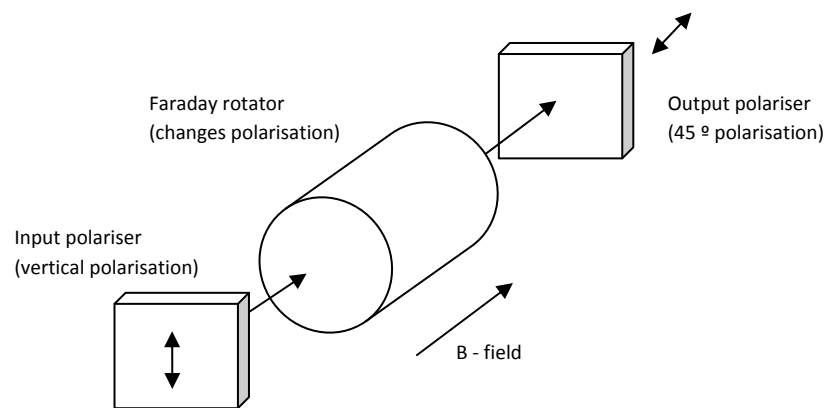


Figure 4.8 Diagram of the polarisation dependence permitted by a Faraday isolator

Upon input to the Faraday isolator, the beam has vertical polarisation and therefore can pass through the polariser. Upon propagation through the Faraday rotator, polarisation is altered by 45° due to the Faraday effect. The beam can then pass

through the 45 ° output polariser. Any feedback which is incurred after the isolator will maintain this 45 ° polarisation. Therefore as it passes through the rotator, it is rotated a further 45 ° and is thus blocked by the input polariser. This effect is made possible due to the direction of polarisation change being independent of the direction of propagation.

Element 3 is a half-wave plate used to control the polarisation incident to the beam-splitter (element 4), as the distribution of power is polarisation dependent. This ensures a 50/50 split in power, whilst the half-wave plate at element 5, controls the polarisation which enters the nonlinear crystal.

The lenses used as elements 6 & 7 were used to provide mode-matching of the pump to the resonator, ensuring that efficient transfer of energy can take place. From Eq. (4.15), it was calculated that the optimal beam waist of the pump beam w_0 , should be 9 μm for this system. In practice however, other considerations must be taken into account. As seen from Table 4.2, nonlinear crystals have limited damage thresholds. With application of the full 100 kW of peak power available from the pump, confined to a 9 μm beam waist, a peak intensity of 40 GW/cm^2 would be achieved. This greatly exceeds the damage threshold for all nonlinear crystals. Therefore compromises in pump power and beam waist had to be made. A practical pump beam waist of 19 μm , was centred within the PPLN crystal. This was measured using a slit-scanning beam profiler (Thorlabs, BP109-VIS). By implementing half of the total power available from the pump source, a peak intensity of 3.55 GW/cm^2 was provided.

Curved mirrors (elements 8 & 10) were used to provide a resonant cavity with a signal spot size of 25 μm . This value was calculated from mode matching (Eq. 4.14 and 4.15). This beam waist was modelled using WinLase, through the implementation of ABCD matrix theory.

Nonlinear crystals are subject to various acceptance bandwidths. These are described in Section 2.9. A spectral acceptance of 10 nm was calculated from Eq. (2.20). This acceptance covers the majority of the spectral bandwidth of the pump source (12 nm) ensuring that almost all of the pump source is converted. Equation (2.21) gives an acceptance temperature bandwidth of 8 °K. The useful length of the PPLN crystal is determined by Eq. (2.15) and yields a value of 1.5 mm.

Due to restrictions in the commercial availability of crystals, a crystal length of 3 mm was chosen. Period lengths ranging from 28.5 - 29.9 μm were used (covered by 8 grating periods). To reduce reflection losses, an anti- reflection coating (at 1064 nm) was present on the PPLN crystal surface closest to element 8. Since this crystal was cut from a larger piece of PPLN from a previous experiment, the surface closest to element 10 remained uncoated. The crystal was held in a home-made oven which used feedback dependent temperature controller (RS components, 340-083) to provide a temperature accuracy of ± 0.1 °K.

Element 11 was a cavity mirror used to create the standing wave. The output coupler (element 12) was selected in order to provide impedance matching, resulting in the highest efficiency possible. It was also placed upon a micrometre translation stage in order to ensure that the cavity round trip time matched the repetition rate of the pump laser for synchronous pumping. An overall effective SPOPO cavity length of 1.875 m was used, corresponding to the 80 MHz repetition of the pump source.

4.4.2. Double pass pumping SPOPO

The concept of non-resonant reflection of an undepleted CW pump beam upon passing through a OPO crystal was first introduced by Bjorkholm *et al* in 1970 [39]. The benefits suggested by this recycling of the pump beam are a reduction in threshold and greater conversion efficiencies. This concept was experimentally

shown by Yang *et al* [40]. With the introduction of an external cavity mirror, the undepleted pump beam was returned into the crystal.

In more recent times double pass pumping has also been realised for a pulsed pump sources. In 1997 Lee *et al* [41, 42] used the nanosecond pulsed output of a frequency doubled Nd:YAG laser to pump a BBO crystal to show the reduction in threshold and high efficiencies can also be achieved using a double pass pumping geometry. In 2008 Kaneda *et al* [42] showed, using a similar pump source to Lee, an 85% increase in conversion efficiency when comparing this method to the single pass pumped case. They also reported the use of a time delay when returning the pump pulse into the crystal. To date, however, no sub-nanosecond double-pass pumping has been carried out in optical parametric oscillators.

Despite the excellent continuous tuning range available from a single pass pumping geometry, the output power from the system was found to be moderate (< 200 mW) [11]. Upon transmission through the optics in a commercial laser scanning microscopy system (which are designed for visible wavelengths) up to 95 % loss was observed [43]. This unfortunately did not provide the ~ 20 mW which is typically required at the sample, for multiphoton microscopy applications.

In the case for singly resonant single pass pumping, the pump light is not fully depleted, and as the cavity mirrors are highly transmitting at the pump wavelength, this light is dumped and transmitted through the first cavity mirror which is encountered following the crystal. Reflection of this non-depleted pump does not constitute the creation of a DRO as a standing wave is not formed. Therefore, the reduced thresholds and increased efficiencies could be obtained without compromising the tuning ability of the system.

For the single pass pumping geometry described in the previous section, an average undepleted pump power of ~ 550 mW was measured following from the second curved cavity mirror. Using the setup described below, it was possible to reflect this undepleted pump beam and couple it back into the SPOPO cavity.

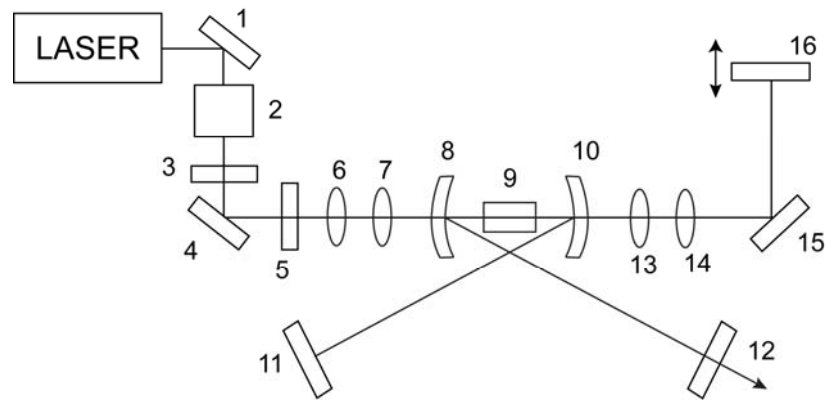


Figure 4.9 Double pass pumping schematic diagram

The OPO was set up in a similar manner to that shown in Fig. 4.6, however additional elements were required. In the experiment of Bjorkholm *et al* [39], the positioning of the undepleted pump reflector was placed at a somewhat arbitrary position. Due to its application in cw or Q-switched lasers, the overlap with the circulating signal wavelength is not critical. However, as this setup is for a femtosecond pulsed SPOPO, it is critical that overlap is ensured. This is because the reflected pulse must be synchronised with the resonating pulse during the short period of time that it is propagating through the crystal. Control of this synchronisation was achieved through the introduction of a delay line.

Elements 13 & 14 were spherical lenses ($f = 75$ mm & 100 mm, AR coated at 1064 nm) were used to collimate the pump beam following exiting the resonator and then re-coupling into the cavity on the return path. Elements 15 and 16 are steering mirrors (plane HR @ 1.064 μm) with element 16 being placed upon a micrometer-based translation stage in order to provide the time delay.

With reference to the coupled amplitude equations in Chapter 2.4, it is clear that additional pump being introduced into the cavity will provide an overall increase to the signal output. One of the advantages of using this technique for ultrafast systems is that the damage limitations are relaxed i.e. additional pump power may be used in a crystal without causing damage. As the reflected pump pulse is synchronised with the circulating signal pulse in the reverse pass through the crystal, no two pump pulses are present within the crystal at any given time. This technique permits a peak pump intensity of 3.55 GW/cm^2 from the forward direction and with 1.85 GW/cm^2 from the undepleted component. A combination of both gives a total useful peak intensity of 5.4 GW/cm^2 , exceeding the damage threshold of 4 GW/cm^2 whilst incurring no crystal damage.

4.4.3. Bi-directional pumping SPOPO

Although the double pass pumping geometry allows application of higher total intensity to the nonlinear optical crystal without inducing damage, this approach still does not permit the use of all available pump intensity. Consequently the total conversion efficiency of the platform remained sub-optimal.

This problem was addressed by investigating a bi-directional pump geometry. In doing so, simultaneous synchronizing of a ‘forward’ pump pulse, and a second counter-propagating pulse in the ‘reverse’ direction, to the circulating signal pulse. Hence the signal electric field amplitude experiences gain in both directions and resulted in an average output power that scaled nonlinearly with the overall input pump power.

By ensuring only one pump pulse with an intensity level below the damage threshold is present in the nonlinear crystal at any given time, this technique permitted a total pump intensity of up to twice the damage threshold intensity, without incurring damage. As a consequence, the crystal damage threshold intensity conditions were relaxed while the average and peak output powers of the SPOPO could be significantly increased.

To explore this geometry, a SPOPO setup similar to that used in Fig. 4.6 was employed (elements 1-12). In the previous section however, 50 % of the pump laser power was dumped following the beam splitter (element 4). This technique implements this additional pump power to generate higher signal power.

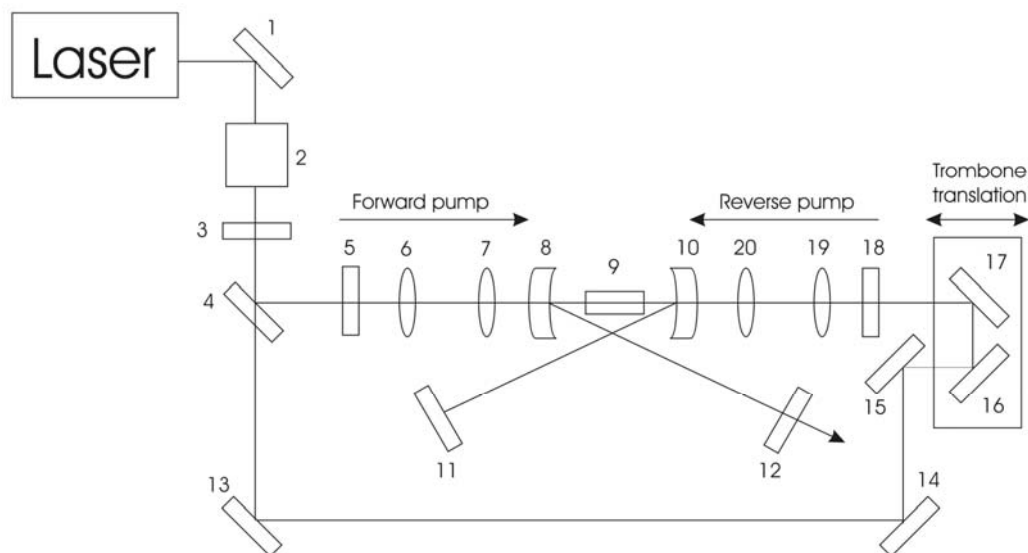


Figure 4.10 Schematic of a bi-directional pumped SPOPO setup

Figure 4.10 shows the additional elements required allowing a conventional single pass pump geometry to be converted to a bi-directional geometry (elements 13 – 20). 13, 14, 15, 16 & 17; plane beam steering mirrors (HR @ 1.064 μm), with 16 & 17 placed upon a translation stage to provide the time delay for temporal overlap. 18;

half wave plate for polarisation control at 1.064 μm , 19 & 20; spherical lenses ($f = 63$ mm and 50 mm, AR coated at 1064 nm). Both sets of spherical lenses (6 & 7 and 19 & 20) provide measured a beam radius of 20 μm using a beam profiler in both the forward and reverse direction. The PPLN crystal was anti-reflection coated at the pump wavelength on one surface only, namely the surface closest to the element 8, due to the crystal being a section cut from a longer PPLN crystal for this study. Neither surface was anti-reflection coated at the signal or idler wavelengths. This resulted in a substantial optical loss which was detrimental to the overall conversion efficiency. For this experiment the crystal was kept in the home-made oven at a constant temperature of 100 $^{\circ}\text{C}$ to ensure fixed signal wavelength operation.

4.5 Results

4.5.1 Single pass pumping SPOPO: Results

As the refractive indices of nonlinear crystals are dependent on the temperature (described by the Sellmeier equation in Eq. 2.5) and the output of a SPOPO is based upon the phase matching conditions, a wide range of wavelength tuning can be achieved through temperature control.

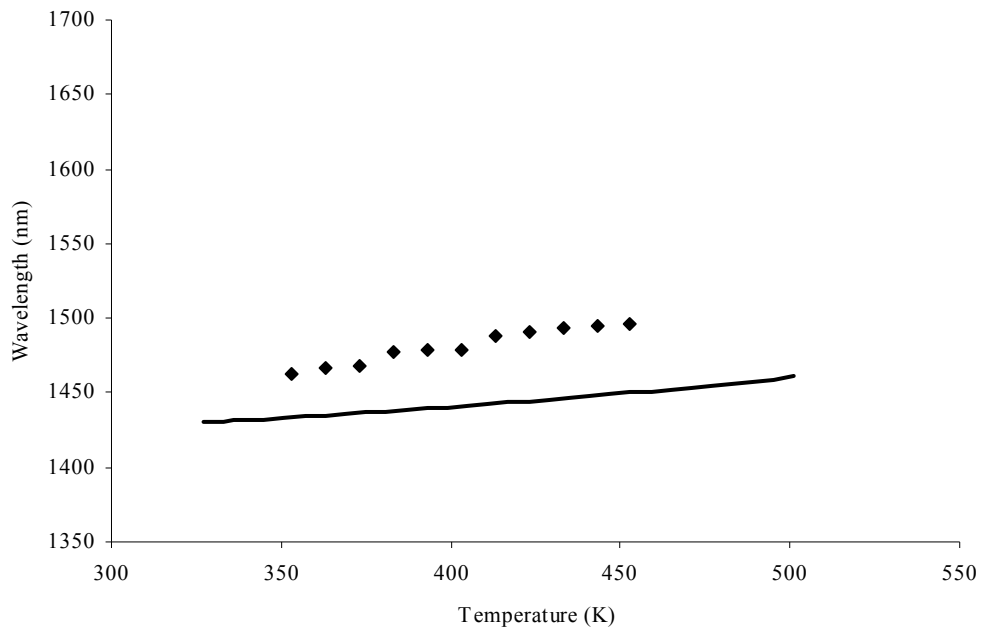


Figure 4.11 Experimental (diamonds) and theoretical (solid line) plot of the wavelength dependence upon temperature for a fixed period length of 28.5 μm .

Figure 4.11 shows the relation between experimental and theoretical results for temperature dependent wavelength tuning. Discrepancies of up to 30 nm between experimental and theoretical results were observed. This is due to the inconsistencies in period length across each grating [5].

A practical crystal temperature range of 353 – 453 °K was available. This range was restricted by two factors. Firstly, intense laser sources within PPLN crystals at temperatures below 353 °K often lead to photo-refractive damage [44]. Secondly, an upper limit of 453 °K was imposed by the limitations of the crystal oven – beyond this value; the integrity of the oven was compromised.

Analysis of the resulting data demonstrates an experimental tuning range of the signal wavelength from $\lambda = 1455 - 1650$ nm. Despite a deviation from the theoretical values calculated in Eq. 2.5, the experimental results follow a similar trend.

Deviation from the theoretical value is mainly due to the use of the Sellmeier coefficients which were used in this analysis. Values for bulk Lithium Niobate were used as an approximation to the periodically poled case since these coefficients are unavailable to PPLN. The temperature conditions under which each wavelength was generated was recorded for each of the eight poling periods and in doing so, allowing straightforward wavelength selection over this range.

An important consideration for application of longer wavelength sources to microscopy platforms is the knowledge that coupling losses to the microscope are like to be high. The reason for this is the elements of commercial microscopes typically being coated for application to visible wavelengths. Therefore the output power from the SPOPO should be high to pre-compensate for this loss. By tuning across the wavelength range of the SPOPO and noting the average output power, it was found that a maximum value of 200 mW could be achieved. Average powers remained approximately constant throughout this tuning range, exhibiting a standard deviation of $\sim 10\%$.

Each of the average power readings measured above were taken at the optimum overlap of pump pulses and resonating signal pulses (i.e. synchronously pumped). However, in some instances it is beneficial to operate the SPOPO with a small amount of de-synchronisation, which is achieved through manipulation of the SPOPO resonator length.

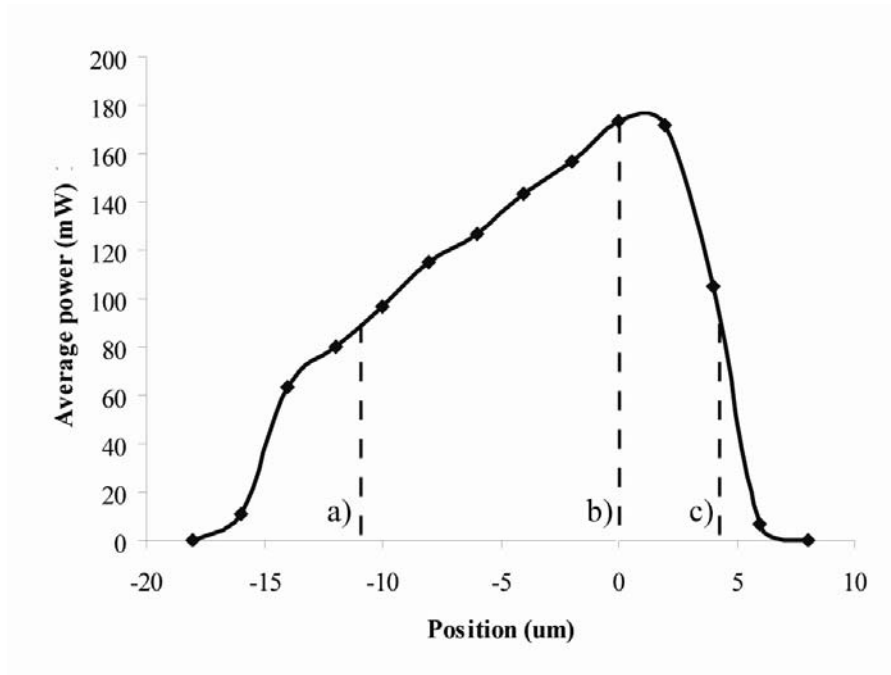


Figure 4.12 Cavity length tolerance with average signal power. Values at a) and c) represent the FWHM and b) giving the point of synchronisation.

Figure 4.12 gives the measured tolerance of the average signal power as a function of translation of an end mirror of the SPOPO cavity. To establish a convention used throughout this thesis, positive values represent an increase in cavity length, and negative values represent a decrease in cavity length. Pulse durations were also measured at points a, b and c.

An asymmetric cavity length tolerance of $\sim 15 \mu\text{m}$, at FWHM, was found. This asymmetry was to be expected and has been reported previously by Lefort *et al* [45] who attribute this asymmetry to the group velocity mismatch (GVM) of the pump and signal pulses experienced within the crystal.

Upon reducing the cavity length beyond optimal synchronisation, group velocity dispersion plays a role in the pulse duration of the signal. Upon propagating through the crystal, group velocity dispersion can often lead to the broadening or

compression of pulses (depending upon whether the cavity is shortened or lengthened). In the case of Lefort *et al*, compression of up to 20 times could be observed using this method.

When the SPOPO cavity length is greater than the optimal synchronisation, the signal pulse enters the nonlinear crystal with a time delay with respect to the pump pulse. Upon transmission through the crystal, the signal can catch the pump wavelength and deplete the full length of the pulse. In doing so allowing signal pulses become shortened. Using the reference points a, b and c in Fig. 4.12, corresponding pulse durations can be given: $\tau_a = 280$ fs, $\tau_b = 250$ fs and $\tau_c = 160$ fs. This observed effect was less prominent than that seen by Lefort *et al*. This is likely to be due to their use of a longer nonlinear crystal and pump pulses in the picosecond regime.

It was noted that the signal wavelength was also altered as a result of the cavity length tuning. This again has been previously observed [23] and is the result of a shift incurred to alter the group velocity dispersion in order to maintain a constant cavity round trip time.

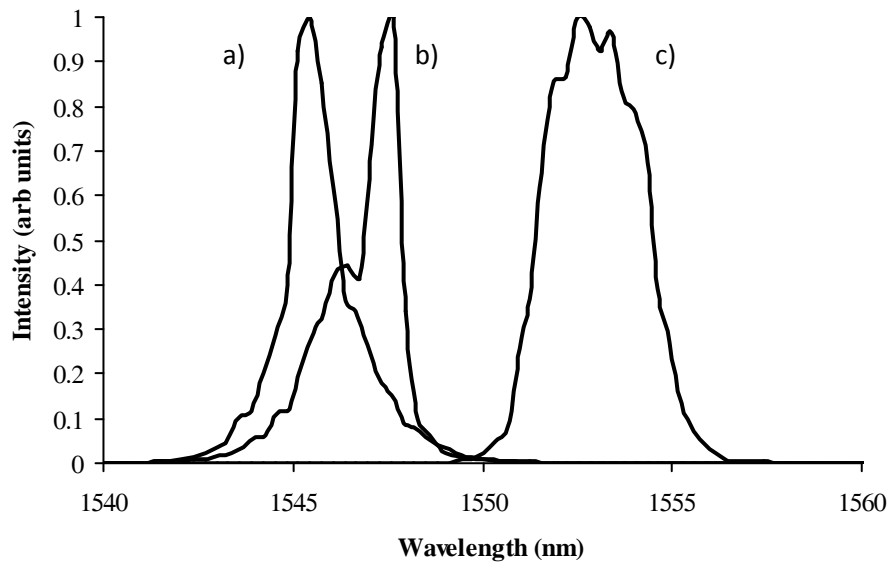


Figure 4.13 Output signal wavelength at a) lengthened cavity, b) synchronised cavity and c) shorter cavity.

For the shortened, synchronised and lengthened cavity lengths corresponding to a, b and c in Fig. 4.12, the spectrum for each position was measured and is shown in Fig. 4.13. Manipulation of the cavity length offers an additional ~ 10 nm control of spectral tuning. As seen from Fig. 4.12, this comes however at the expense of a reduction in power.

These observations are consistent with previous reports of SPOPOs and provide an additional method for fine adjustment to wavelength tuning, which is important for the application in fluorescence microscopy.

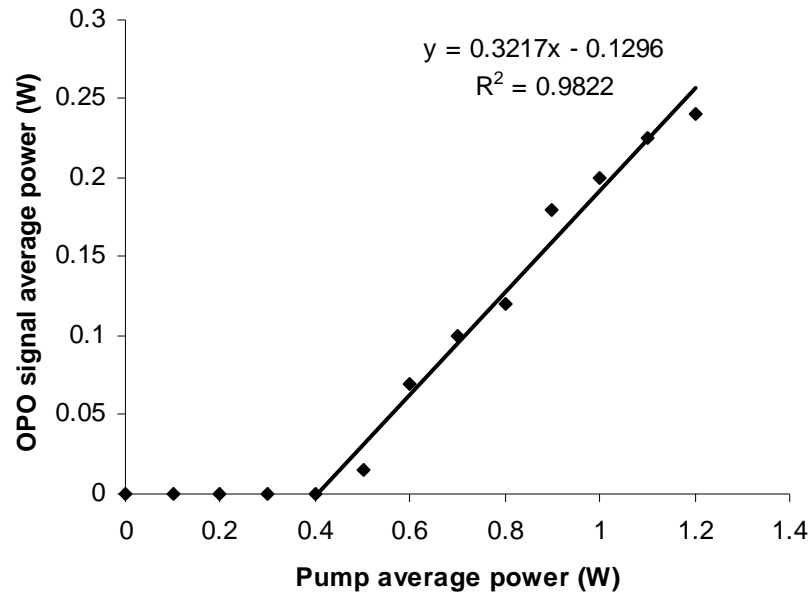


Figure 4.14 Threshold measurement and slope efficiency.

Figure 4.14 shows the generated average signal power as a function of the increase in average pump power. From this it was obtained that the threshold of the SPOPO was found at 400 mW. The slope efficiency was found from the linear best-fit gradient of the pump powers above threshold, yielding a slope efficiency of 32 %.

4.5.2. Double pass pumping SPOPO: Results

Applying the system described in Section 4.4.2. where the undepleted pump beam is non-resonantly reflected back into the cavity, the following power outputs were observed as a result of manipulation of the time delay (element 16, Fig. 4.9).

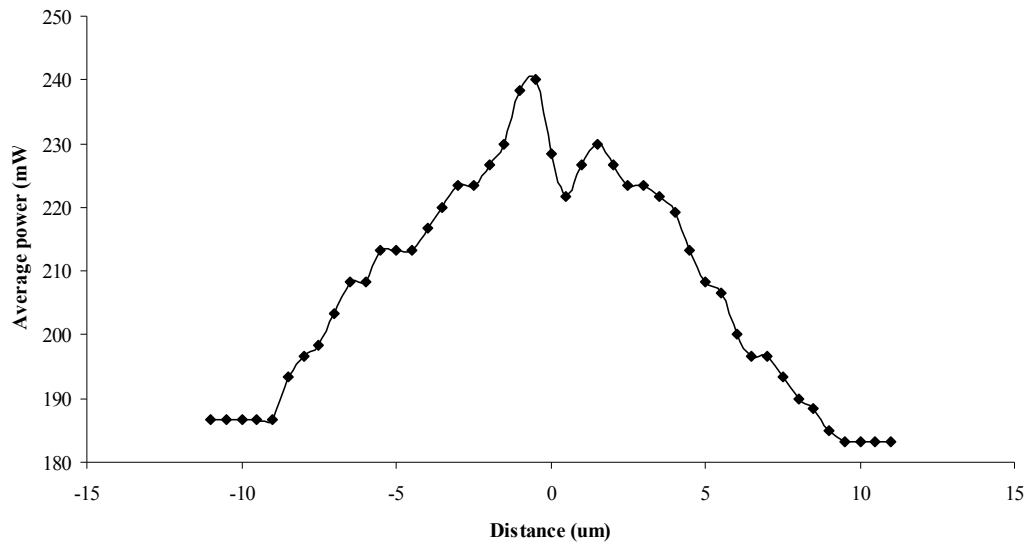


Figure 4.15 Overlap of reflected undepleted pump pulse as a function of average signal power

Figure 4.15 shows the increase experienced average output power as a consequence of the reflected undepleted pump pulse as it passes through the point of synchronisation with the resonating signal pulses. A maximum average output power of 240 mW was recorded at the point of synchronisation. The pulse duration at this point is relatively unchanged when compared to the input pulse (~ 250 fs). This corresponded to a peak power of ~ 11 kW which corresponded to an increase of 20% when comparing to the single pass output geometry.

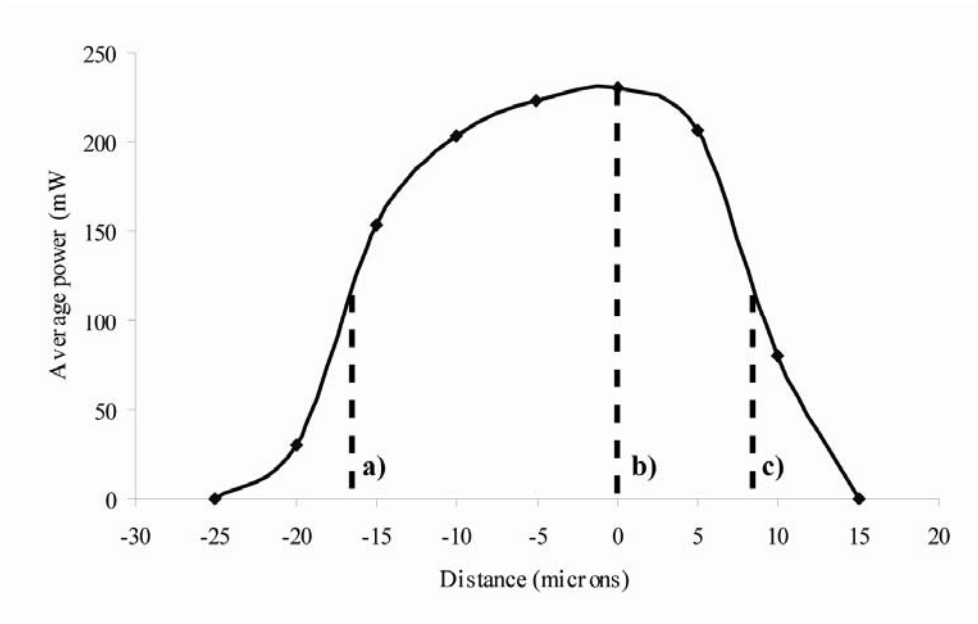


Figure 4.16 Double pass pumping cavity length tolerance dependence upon average power. a) and c) represent the FWHM values and b) represents synchronisation.

Figure 4.16 shows that an increase in cavity length tolerance is also observed, changing from $\sim 15 \mu\text{m}$ in single pass pumping (at FWHM) to $\sim 25 \mu\text{m}$ for double pass pumping. This suggests that the introduction of a reflected pump beam partially compensated for the poor temporal synchronization of the pump/signal pulses in addition to increasing the average output power of the signal wavelength.

4.5.3. Bi-directional pumping SPOPO: Results

The following results were obtained using the novel bi-directional pumping geometry as described in Section 4.4.3. This geometry was designed to provide maximum peak power extraction from a SPOPO.

Figure 4.17 shows the measured average signal output powers resulting from single-pass pumping in the forward and reverse directions independently. Also shown is the nonlinear increase in average power when both the forward and reverse pump pulses

were synchronized with the resonating signal pulse, as per the bi-directional pump geometry described previously. The average powers obtained from the independent forward and reverse pumping schemes were 200 mW and 120 mW respectively, which in turn equated to pump depletions of 64 % and 47 %. This discrepancy in average output power, despite the similar characteristics of the pump pulses, arose as a result of the presence of the anti-reflection coating on only one surface of the crystal. The x-axis in Fig. 4.17 represents the translation of the delay line (elements 16 and 17, Fig. 4.10) which resulted in a synchronization of the reverse pump pulse and the resonating signal pulse created by the initial forward pump pulse.

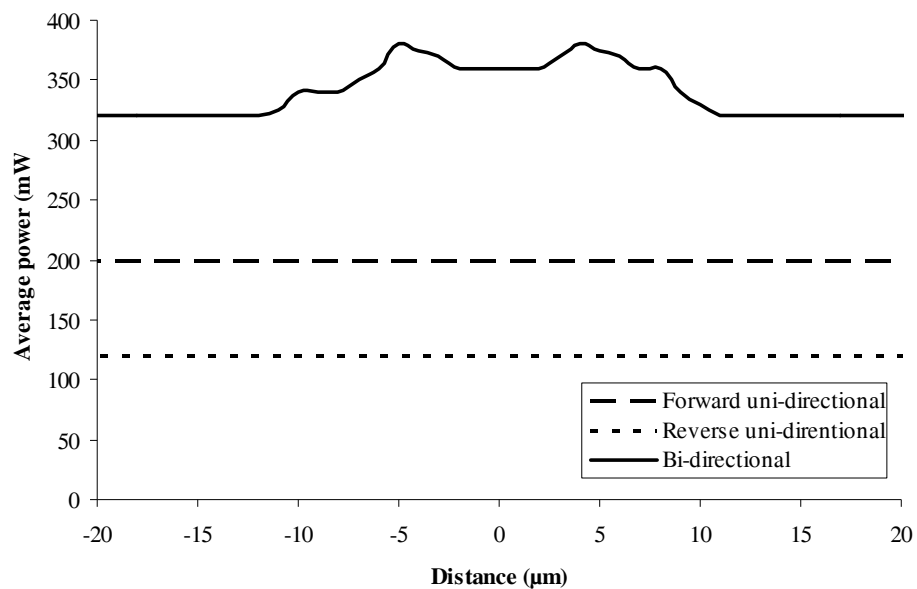


Figure 4.17 Nonlinear increase in net average output power when forward and backward pump pulses were brought into synchronization with the resonating signal pulse. The x-axis zero point corresponds to exact overlap of the reverse pump and signal wavelength pulses

As a result of applying an appropriate time-delay to the reverse pump pulse relative to the circulating signal wavelength pulse, an increase in average signal wavelength output power was achieved. In this demonstration, using the bi-directional pump geometry the average output power was measured to be 390 mW when the pump pulses were synchronized with the intracavity circulating signal wavelength pulse.

This increase arises from the linear summation (120 mW + 200 mW) of the independent pump sources and a nonlinear increase of 22 % (70 mW) in average power when both pump pulses operate synchronously. All average powers were measured using a calibrated calorimeter (Spectra-Physics, 407A) after transmission through a long-wave pass optical interference filter which was measured to be 85% transmitting at the signal wavelength (Thorlabs, FEL0450). Importantly, the generated output power was higher than the measured 390 mW with an average output power of 460 mW (140 mW + 235 mW), corresponding to a net average power increase of 95 % observed at the signal wavelength when compared to the single-pass pumping in the forward direction.

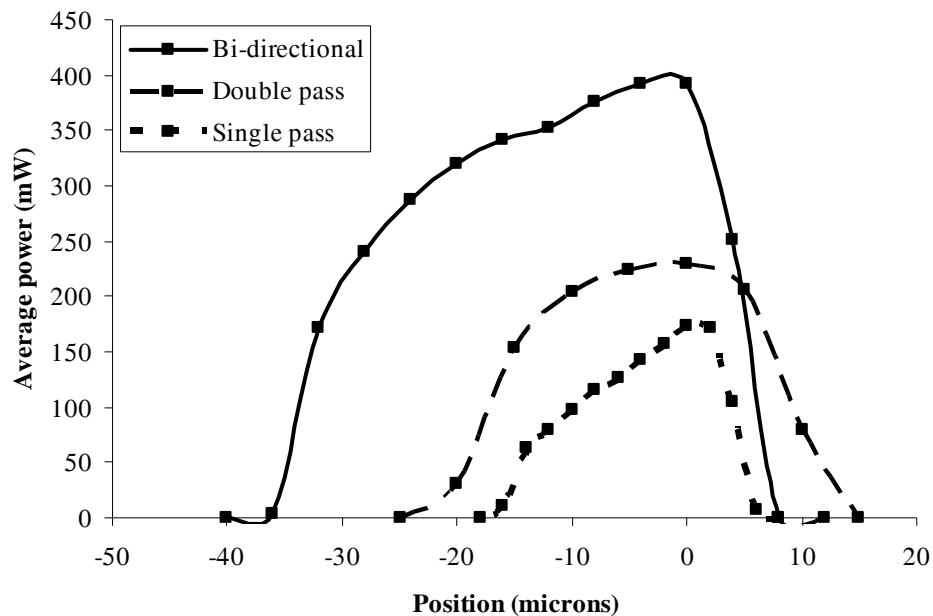


Figure 4.18 Cavity length tolerance for single-, double-, and bi-directional- pass pumping

Figure 4.18 shows the cavity length detuning tolerance when applying the single pass, double pass and bi-directional pump geometries. Using the single-pass geometry a maximum SPOPO cavity length detuning tolerance at FWHM was 15 μm . When applying double pass pump geometry, cavity length detuning tolerance

increased to 25 μm as a result of the reflected pump beam partially compensating for the poor temporal synchronization of the pump/signal pulses. When applying the bi-directional pump geometry, the SPOPO cavity length detuning tolerance increased to $\sim 40 \mu\text{m}$. This indicated that the application of two separate pump beams further compensated for the poor temporal synchronization of the pump/signal pulses as was seen to some extent from the double pass results.

	Average power	Cavity length tolerance (FWHM)	Peak output power
Single pass	200 mW	15 μm	10 kW
Double pass	240 mW	25 μm	12 kW
Bi-directional	390 mW	40 μm	18.8 kW

Table 4.4 Collected data from single pass, double pass and bi-directional pump geometries

Table 1 highlights an increase of $\sim 90 \%$ in peak signal power generated from the OPO when comparing the bi-directional to single pass pump geometries. When comparing to the double pass technique, bi-directional pumping also generates $\sim 60 \%$ more peak power.

4.6 Discussion

A conventional single pass pumped SPOPO can provide excellent tuning capabilities through a combination of temperature and period length tuning. Using this setup a tuning range of 1.45 – 1.6 μm was achieved. This is ideal for application in three photon fluorescence microscopy as many of the common fluorophores have a peak excitation at $\sim 500 \text{ nm}$. Having this tunability would allow optimal wavelength excitation for each fluorophore. However, only an average power of 200 mW was possible when using this geometry, at unchanged pulse duration of 250 fs. When

looking to apply this source to a conventional laser scanning microscope, it was found that substantial losses were incurred due to the optics with not being designed for longer wavelengths. This resulted in low power at the sample; as a result three photon absorption was not possible.

Efficiency enhancing techniques were then pursued, beginning with double pass pumping of the SPOPO. This geometry introduced the non-resonant reflection of the undepleted pump beam after passing through the nonlinear crystal. This technique had previously only been applied to cw and Q-switched OPOs, however, by introducing a time delay, it was possible to ensure that good synchronisation to the resonating signal was achieved. Applying this to the ultra-short pulsed OPO designed for the single pass geometry, it was possible to experience an increase of up to 20 % in peak power. Pulse durations were relatively unchanged in comparison to the single pass case. It was noted that the cavity detuning tolerance of this system was improved as a result of the reflected beam, which somewhat compensated for the temporal differences between signal and pump pulses. This geometry allowed the relaxation of crystal damage limitations, as 5.4 GW/cm^2 of overall pump power could be used within a PPLN crystal with a tolerance of 4 GW/cm^2 . Despite this increase in SPOPO output efficiency, peak power at the sample was still too low to achieve three photon microscopy.

Noting that 50 % of power from the laser pump source was being dumped, and expanding upon the crystal damage threshold relaxation, a novel, bi-directional pump geometry was conceived. This involved the use of the otherwise 'dumped' pump laser pump being re-routed to pump the SPOPO designed in the single pass experiment from the opposite direction. By ensuring that this counter-propagating 'reverse' pump pulse had a peak intensity equal to that of the forward pump pulse ($\sim 3.55 \text{ GW/cm}^2$) which is just below the damage threshold, it was possible to optimise the power from the system. Pumping the SPOPO from both directions permitted oscillation in both directions (either running the SPOPO with the forward or reverse

pump). Independently, the forward and reverse pump beams produced 200 mW and 120 mW respectively. The low power in the reverse pass is a result of no anti-reflection coating at the pump wavelength on the 'reverse' surface of the crystal. When running both pump beams synchronously, not only do the generated signal beams sum together, but there is an additional nonlinear increase of 22 % giving 390 mW opposed to a linear 320 mW. This was a result of the dependence of the signal electric field upon signal which is already resonating in a cavity. If this system was not limited by the loss induced by the crystal surface with no anti-reflection coating, it is conceivable that over a 100 % increase in peak power could be achieved. It was also noted that the cavity length detuning tolerance was substantially increased from the single and double pass case of 15 and 25 μm respectively, to 40 μm at FWHM. This increase was a result of the second pump beam compensating for the temporal separation of the signal and pump pulses.

Using this geometry, 18.8 kW of peak power was available from the SPOPO. This represents a 90 % increase upon single pass pumping and a 60 % increase comparing with double pass pumping.

As a result of this the output of the bi-directional SPOPO was thought likely to provide enough excitation peak power at the sample to achieve three photon microscopy.

4.7 Application of the bi-directionally pumped SPOPO to three photon laser scanning microscopy

The bi-directionally pumped SPOPO source was coupled into a commercial laser scanning microscope system (Bio-Rad MRC 1024 and inverted microscope) as shown in Fig. 4.19, to evaluate performance for three photon laser scanning microscopy.

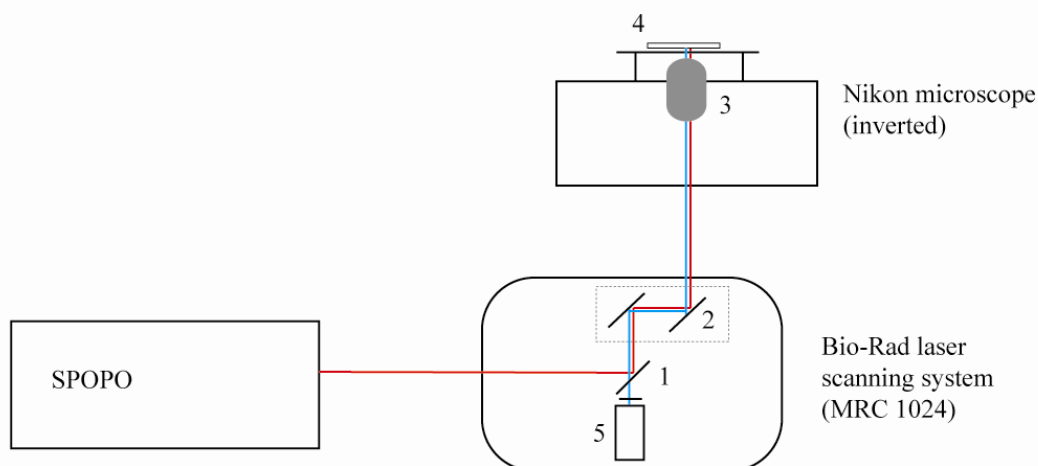


Figure 4.19 Inverted laser scanning microscope applied to three photon excitation

Fig. 4.19 represents the commercial microscope system which was used for imaging where the red beam illustrates the excitation pathway and the blue beam highlights the emission path. This system was designed for CLSM and while the optical loss of this system when used with the SPOPO will be appreciably higher than when used with the intended Kr/Ar laser source, this imaging system was used to test the developed source as no commercially available three photon laser scanning microscope presently exists.

Element 1 is a two photon filter cube (which was designed for reflection of wavelengths $\sim 700 - 900$ nm and transmitting in the visible). Element 2 is a pair of galvo-scanning mirrors which are used to raster scan the laser across the sample. Element 3 was a 20x objective lens (0.75 NA). Element 4 was the sample, which in this case was ‘fluoresbrite’ beads (0.5 μm diameter, peak absorption at 529 nm). Element 5 was a PMT designed for optimal detection between 500 – 620 nm. Directly preceding the PMT, a 700 nm short pass filter was placed within the emission path. Following collection of fluorescence by the PMT, images are reconstructed using the imaging software Laserssharp 2000.

This system exhibited high loss for the 1550 nm wavelength which was used for excitation. Approximately 11 % of the power which was entered into the laser scanner and the microscope reached the sample. By looking at Table 4.4, and considering the 11 % transmission which was available, this corresponded to average powers of 42, 26 and 22 mW for the bi-directional, double pass and single pass SPOPOs respectively.

When imaging with the single pump pass and double pump pass geometries, no three photon fluorescence signal could be obtained.

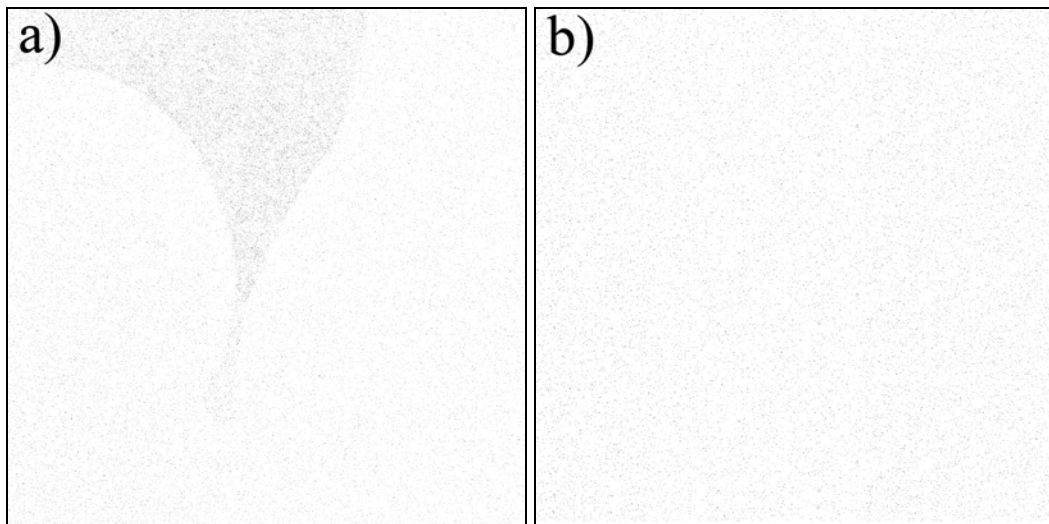


Figure 4.20 a): Bi-directionally pumped SPOPO operating solely in the forward pump direction and b): solely in the reverse pump direction. Contrast in both images have been inverted for the purpose of clarity.

When applying the bi-directionally pumped SPOPO independently in the forward pump direction (20 mW at sample) and then in the reverse pump direction (13.5 mW at sample), it can be seen that effectively no three photon fluorescence may be observed (Fig. 4.20). However, when both pump directions operate simultaneously as described in section 4.4.3. (42 mW), a clear fluorescence image is produced.

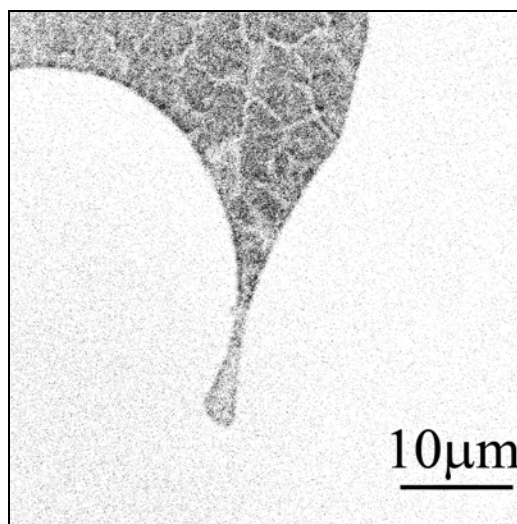


Figure 4.21 Bi-directional operation of the SPOPO for three photon imaging of 0.5 μm Fluoresbrite beads. Contrast has been inverted for the purpose of clarity.

Figure 4.21 shows the three photon emission produced by 0.5 μm Fluoresbrite beads, which have a peak excitation wavelength of 529 nm and an emission at 546 nm.

In order to confirm three photon excitation, incremental power scaling was performed and a log/log plot of the excitation power versus fluorescence intensity was graphed, which is the standard test for multiphoton excitation confirmation [10, 46].

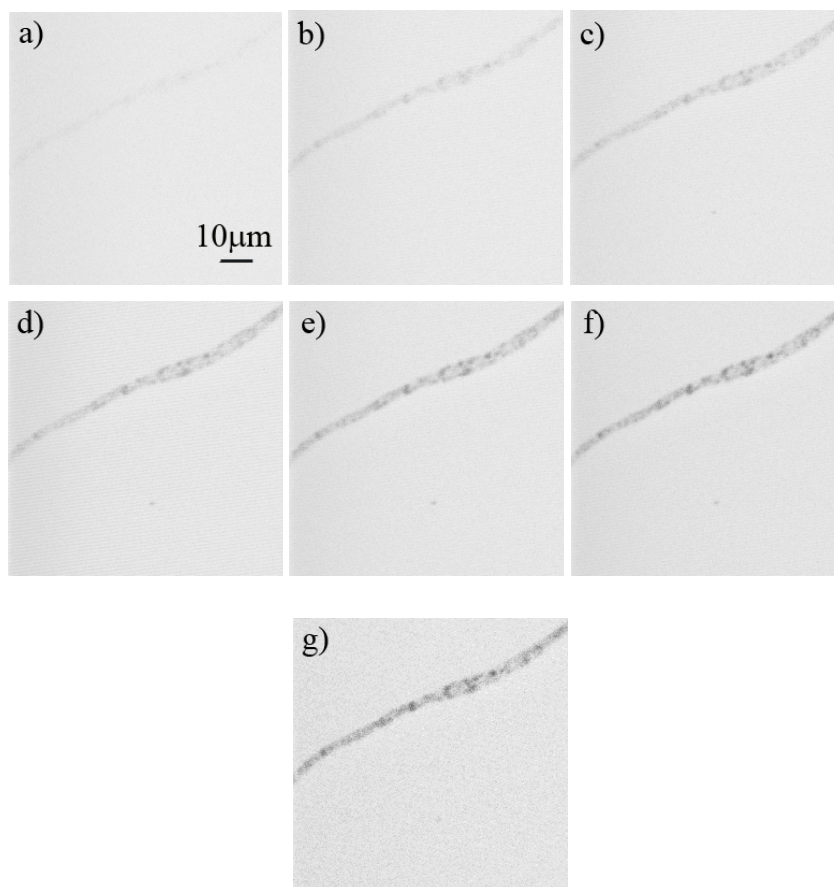


Figure 4.22 Three photon excitation power scaling of fluorescent beads ranging from 30 – 42 mW

From each of the images shown in Fig 4.22, the average image pixel intensity was measured using image analysis software (Metamorph). In doing so, these provided values for a relative intensity generated in each image and could be plotted to confirm the three photon nature of the excitation.

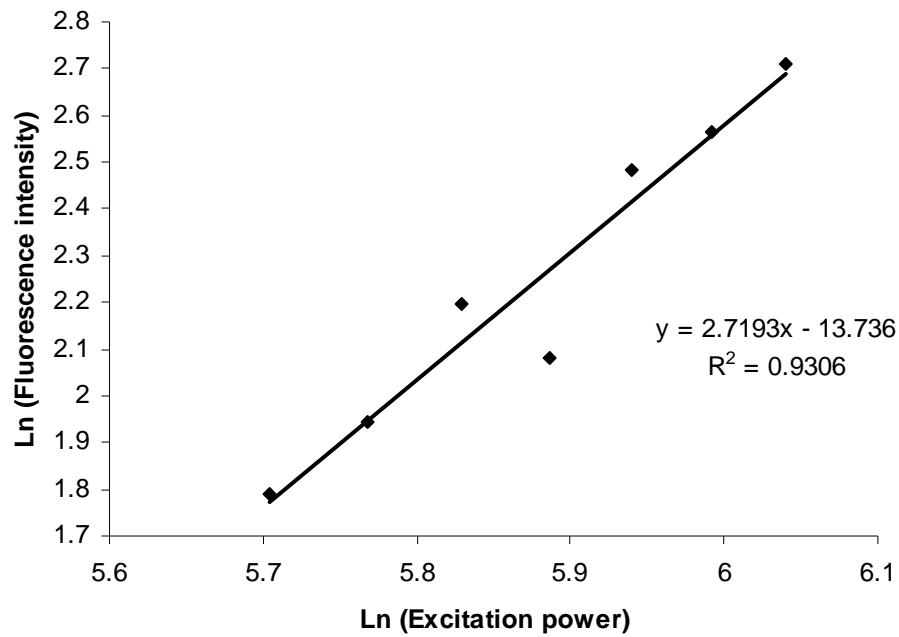


Figure 4.23 log/log plot of the excitation power and the fluorescence intensity (arbitrary units).

The resulting best fit line from the data acquired from the power scaling images yields a gradient of 2.72. With the data providing a standard deviation of 12 %, the data range falls within the expected value of 3 (indicating three photon excitation), the small discrepancy may be a result of saturation.

In light of the three photon excitation applied to fluorescent beads, imaging was also performed on a fixed biological sample. Dendritic cells which had been labelled using Fluorescein (FITC) were chosen due important role which these cells play within the immune system and the peak excitation wavelength of 495 nm and emission at 525 nm were ideally suited for this system.

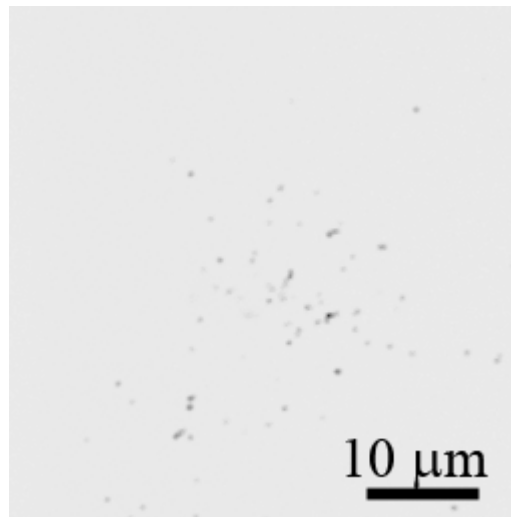


Figure 4.24 Three photon image of dendritic cells labelled with FITC. Contrast is inverted for the purpose of clarity

Figure 4.24 was obtained using an average power of 42 mW at a wavelength of 1550 nm. This illustrates that the system developed can be used for biological imaging. It also demonstrates that SPOPOs can be adapted to provide a useful tool for three photon excitation fluorescence microscopy.

4.8 Conclusion

This chapter presented a novel bi-directional pump geometry that nonlinearly increased the nonlinear optical conversion efficiency of a SPOPO.

This bi-directional pumping method synchronised the circulating signal pulse with two counter-propagating pump pulses within a linear OPO resonator. Through this pump scheme, an increase in nonlinear optical conversion efficiency of 22 % was achieved at the signal wavelength, corresponding to a 90 % overall increase in average power.

Given an almost unchanged measured pulse duration of 260 fs under optimal performance conditions, this related to a signal wavelength peak power output of 18.8 kW, compared with 10 kW using the traditional single-pass geometry. In this study, a total effective peak intensity pump-field of 7.11 GW/cm² (corresponding to 3.55 GW/cm² from each pump beam) was applied to a 3 mm long PPLN crystal, which had a damage threshold intensity of 4 GW/cm², without impairing crystal integrity.

The application of this novel pump geometry provided opportunities for power-scaling of synchronously pumped OPO systems together with enhanced nonlinear conversion efficiency through relaxed damage threshold intensity conditions.

Within this chapter, the need for high peak intensity excitation sources for application in three photon laser scanning microscopy has been highlighted. These are required as a result of the losses in the region of 90 %, when applying longer wavelength sources to commercial microscopes. This source has been successfully applied to three photon laser scanning microscopy of both fluorescent beads and biological samples.

4.9 References:

1. Helmchen, F. and W. Denk, *Deep tissue two-photon microscopy*. Nature Methods, 2005. **2**(12): p. 932.
2. Masters, B., P. So, and E. Gratton, *Multiphoton excitation fluorescence microscopy and spectroscopy of in vivo human skin*. Biophysical Journal, 1997. **72**(6): p. 2405.
3. Zumbusch, A., G.R. Holtom, and X.S. Xie, *Three-Dimensional Vibrational Imaging by Coherent Anti-Stokes Raman Scattering*. Physical Review Letters, 1999. **82**(20): p. 4142.

4. Freudiger, C.W., W. Min, B.G. Saar, S. Lu, G.R. Holtom, C. He, J.C. Tsai, J.X. Kang and X.S. Xie, et al., *Label-free biomedical imaging with high sensitivity by stimulated Raman scattering microscopy*. *Science*, 2008. **322**(5909): p. 1857.
5. Harris, J., G. Norris, and G. McConnell, *Characterisation of periodically poled materials using nonlinear microscopy*. *Optics Express*, 2008. **16**(8): p. 5667.
6. Xu, C. and W. Denk, *Two-photon optical beam induced current imaging through the backside of integrated circuits*. *Applied Physics Letters*, 1997. **71**: p. 2578.
7. Szmacinski, H., I. Gryczynski, and J.R. Lakowicz, *Three-photon induced fluorescence of the calcium probe Indo-1*. *Biophysical Journal*, 1996. **70**(1): p. 547.
8. Lakowicz, J.R., I. Gryczynski, H. Malak, M. Schrader, P. Engelhardt, H. Kano and S.W. Hell, *Time-Resolved Fluorescence Spectroscopy and Imaging of DNA Labeled with DAPI and Hoechst 33342 Using Three-Photon Excitation*. *Biophysical Journal*, 1997. **72**(2, Part 1): p. 567.
9. Hell, S.W., K. Bahlmann, M. Schrader, A. Soini, H. Malak, I. Gryczynski, and J.R. Lakowicz, *Three-photon excitation in fluorescence microscopy*. *Journal of Biomedical Optics*, 1996. **1**(1): p. 71.
10. Wokosin, D.L., V.E. Centonze, S. Crittenden, J. White, *Three-photon excitation fluorescence imaging of biological specimens using an all-solid-state laser*. *Bioimaging*, 1996. **4**(3): p. 208.
11. McConnell, G., G.L. Smith, , J.M. Girkin, A.M. Gurney, and A.I. Ferguson, *Two-photon microscopy of fura-2-loaded cardiac myocytes with an all-solid-state tunable and visible femtosecond laser source*. *Optics Letters*, 2003. **28**(19): p. 1742.
12. Baxter, G.W., M.J. Johnson, J.G. Haub and B.J. Orr, *OPO CARS: coherent anti-Stokes Raman spectroscopy using tunable optical parametric oscillators injection-seeded by external-cavity diode lasers*. *Chemical Physics Letters*, 1996. **251**(3-4): p. 211.
13. Débarre, D., W. Supatto, A.M. Pena, A. Fabre, T. Tordjmann, L. Combettes, M.C. Schanne-Klein, and E. Beaurepaire. , *Imaging lipid bodies in cells and tissues using third-harmonic generation microscopy*. *Nature Methods*, 2005. **3**(1): p. 47.
14. Matsumoto, B., *Cell biological applications of confocal microscopy*. 2002: Academic Press.

15. Shank, C., *Measurement of ultrafast phenomena in the femtosecond time domain*. Science, 1983. **219**: p. 1027.
16. Duarte, F.J., *Tunable lasers handbook*. 1995: Academic Press.
17. Kroll, N.M., *Parametric Amplification in Spatially Extended Media and Application to the Design of Tuneable Oscillators at Optical Frequencies*. Physical Review, 1962. **127**: p. 1207.
18. Armstrong, J., N. Bloembergen, J. Ducuing, and P.S. Pershan, *Interactions between light waves in a nonlinear dielectric*. Physical Review, 1962. **127**(6): p. 1918.
19. Giordmaine, J. and R.C. Miller, *Tunable Coherent Parametric Oscillation in LiNbO_3 at Optical Frequencies*. Physical Review Letters, 1965. **14**(24): p. 973.
20. Smith, R.G., J.E. Geusic, H.J. Levinstein, J.J. Rubin, S. Singh, L.G. Van Uitert, Continuous optical parametric oscillation in $\text{Ba}_2\text{NaNb}_5\text{O}_{15}$. Applied Physics Letters, 1968. **12**(9): p. 308.
21. Byer, R.L., M.K. Oshman, J.F. Young, S.E. Harris, Visible cw parametric oscillator. Applied Physics Letters, 1968. **13**(3): p. 109.
22. Burneika, K., M. Ignatavicius, V. Kabelka, A. Piskarskas, A. Stabinis, *Parametric light amplification and oscillation in KDP with mode-locked pump.*, IEEE Journal of Quantum Electronics, 1972. **8**(6): p. 574.
23. Khaydarov, J.D.V., J.H. Andrews, and K.D. Singer, *Pulse compression in a synchronously pumped optical parametric oscillator from group-velocity mismatch*. Optics Letters, 1994. **19**(11): p. 831.
24. Becker, M., D.J. Kuizenga, D.W. Phillion, A.E. Siegman., *Analytic expressions for ultrashort pulse generation in mode-locked optical parametric oscillators*. Journal of Applied Physics, 1974. **45**: p. 3996.
25. Oberparleiter, M. and H. Weinfurter, *Cavity-enhanced generation of polarization-entangled photon pairs*. Optics Communications, 2000. **183**(1-4): p. 133.
26. Sutherland, R.L., D.G. McLean, and S. Kirkpatrick, *Handbook of nonlinear optics*. 2003: Marcel Dekker.
27. Bass, M., *Handbook of Optics: Optical properties of materials, nonlinear optics, quantum optics*. 2009: McGraw-Hill.

28. Richy, C., K.I. Petsas, E. Giacobino, C. Fabre, and L. Lugiato, *Observation of bistability and delayed bifurcation in a triply resonant optical parametric oscillator*. Journal of the Optical Society of America B, 1995. **12**(3): p. 456.
29. Teja, J. and N. Wong, *Twin-beam generation in a triply resonant dual-cavity optical parametric oscillator*. Optics Express, 1998. **2**(3): p. 65.
30. Trager, F., *Springer handbook of lasers and optics*. 2007: Springer.
31. Pawley, J., *Handbook of biological confocal microscopy*. 1995: Plenum Press.
32. Cheung, E. and J. Liu, *Theory of a synchronously pumped optical parametric oscillator in steady-state operation*. Journal of the Optical Society of America B, 1990. **7**(8): p. 1385.
33. Edelstein, D.C., E.S. Wachman, and C.L. Tang, *Broadly tunable high repetition rate femtosecond optical parametric oscillator*. Applied Physics Letters, 1989. **54**(18): p. 1728.
34. Fu, Q., G. Mak, and H. Van Driel, *High-power, 62-fs infrared optical parametric oscillator synchronously pumped by a 76-MHz Ti: sapphire laser*. Optics letters, 1992. **17**(14): p. 1006.
35. McConnell, G., *Nonlinear optical microscopy at wavelengths exceeding 1.4 μm using a synchronously pumped femtosecond-pulsed optical parametric oscillator*. Physics in Medicine and Biology, 2007. **52**: p. 717.
36. Kurti, R.S. and K.D. Singer, *Pulse compression in a silver gallium sulfide, midinfrared, synchronously pumped optical parametric oscillator*. J. Opt. Soc. Am. B, 2005. **22**(10): p. 2157.
37. Boyd, G. and D. Kleinman, *Parametric Interaction of Focused Gaussian Light Beams*. Journal of Applied Physics, 1968. **39**: p. 3597.
38. Van Driel, H., *Synchronously pumped optical parametric oscillators*. Applied Physics B: Lasers and Optics, 1995. **60**(5): p. 411.
39. Bjorkholm, J., A. Ashkin, and R. Smith, *Improvement of optical parametric oscillators by nonresonant pump reflection*. IEEE Journal of Quantum Electronics, 1970. **6**: p. 797.

40. Yang, S., R. Eckardt, and R. Byer, *Continuous-wave singly resonant optical parametric oscillator pumped by a single-frequency resonantly doubled Nd: YAG laser*. Optics Letters, 1993. **18**(12): p. 971.
41. Lee, S.W., S-H. Kim, D-K. Ko, J-M. Han and J. Lee, *High-efficiency and low-threshold operation of the pump reflection configuration in the noncollinear phase matching optical parametric oscillator*. Optics Communications, 1997. **144**(4-6): p. 241.
42. Kaneda, Y., N. Peyghambarian, K. Miyazono, H. Shimatani, Y. Honda, M. Yoshimura, Y. Mori, Y. Kitaoka, and T. Sasaki, *Improved efficiency of a pulsed optical parametric oscillator by delayed double-pass pump*. Optics Letters, 2008. **33**(3): p. 231.
43. Keatings, S.R., W. Zhang, and G. McConnell, *Characterization of microscope objective lenses from 1,400 to 1,650 nm to evaluate performance for long-wavelength nonlinear microscopy applications*. Microscopy Research and Technique, 2008. **71**(7): p. 517.
44. Nakamura M., M. Sugihara, M. Kotoh, H. Taniguchi and K Tadatomo, *Quasi-phase-matched optical parametric oscillator using periodically poled MgO-doped LiNbO₃ crystal*. Japanese Journal of Applied Physics, 1999. **38**(11): p. 1234.
45. Lefort, L., K. Puech, S. D. Butterworth, Y. P. Svirko, and D. C. Hanna, *Generation of femtosecond pulses from order-of-magnitude pulse compression in a synchronously pumped optical parametric oscillator based on periodically poled lithium niobate*. Optics Letters, 1999. **24**(1): p. 28.
46. Denk, W., J. Strickler, and W. Webb, *Two-photon laser scanning fluorescence microscopy*. Science, 1990. **248**(4951): p. 73.

Chapter 5 Femtosecond-pulsed tunable visible laser source for short wavelength two photon microscopy

5.1 Introduction

Ultraviolet radiation has many applications in optical imaging. Many widely used synthetic fluorophores such as DAPI, Hoechst Blue, Fura-2 and Indo-1 have peak excitation wavelengths smaller than $< 380\text{nm}$ [1-7]. Additionally, many naturally occurring molecules present in cells and tissue are fluorescent under the application of ultraviolet radiation. These include tryptophan, NAD(P)H, flavins and some porphyrins, which exhibit absorption/emission peaks of 275/350 nm, 360/470 nm, 440/520 nm and 490/630 nm respectively. The resultant fluorescence signal arising from naturally occurring and intrinsic molecules is usually referred to as autofluorescence. Autofluorescence can be advantageous, as an intrinsic contrast agent as it requires no additional synthetic label to build an image of the sample. There are however disadvantages arising from autofluorescence too. The fluorescence signal from naturally occurring molecules typically has a wide emission spectral bandwidth [1] and is often a source of background over the entire sample, rather than a marker for a specific region of interest. Autofluorescence signals can be difficult to interpret, especially when specificity is low. In spite of this, autofluorescence is widely studied: this method has been implemented for cancer diagnosis, utilising the autofluorescent properties of tissue to identify if cancer is present [2, 3]. Further applications include dental analysis [4] and widespread use in cell physiology [5].

5.1.1 Light sources for ultraviolet excitation

There are many options available for ultraviolet excitation of synthetic and intrinsic fluorescent molecules. Perhaps the most widely used is the Hg or Xe arc lamp that is routinely applied in epi-fluorescence microscopy [6]. This system is relatively cheap

and offers the potential of wavelength flexibility when used with suitable bandpass filters to discriminate the excitation wavelength to match the sample. However, arc lamps are inefficient, with only a small percentage of the spectrally-filtered radiation reaching the sample, and there is a risk of ozone leak from the bulbs, which have a short life-span (typically < 300 hours per bulb).

A more recent alternative to arc lamp systems are light emitting diode (LED). High-powered LEDs offer narrower bandwidth emission (<50 nm) relative to the broadband arc lamp (>300nm) with high brightness and average power [7]. These are efficient systems and have long operational lifetimes, often exceeding 10000 hours [8]. The wavelength range of light emitting diodes is however limited: at present, the shortest wavelength commercially available light emitting diode has a peak emission wavelength of 374 nm and is unsuitable for excitation of many naturally occurring and synthetic fluorescent molecules. Furthermore, light emitting diodes are useful only for epi-fluorescence microscopy and cannot be used in a CLSM or MPLSM geometry. For these applications, a laser system is required.

Options for ultraviolet emitting laser sources are limited. The 405 nm semiconductor diode laser is often colloquially referred to in optical microscopy as a 'UV source', although it is not strictly in the ultraviolet spectral range of < 400 nm. This system has found applications in excitation of DAPI [9] but it is somewhat used in anger as the peak absorption wavelength of DAPI at 351 nm, is more than 50 nm shorter than 405 nm. Another laser source routinely used in optical microscopy is the Kr/Ar laser, which has a laser line at 351 nm. However, this gas-based laser often exhibits high-noise, and is not wavelength tunable.

The solid-state alternative to the Kr/Ar laser is a laser based on a frequency-tripled neodymium-doped gain medium. Multiple frequency tripled solid state sources are also commercially available, providing outputs in excess of 200 mW at a wavelength of 355 nm [10]. However, these systems, using a cascaded nonlinear optical

frequency conversion process to convert 1064 nm radiation to 355 nm are very inefficient.

5.1.2 Challenges and limitations in application of ultraviolet radiation in optical microscopy

There are fundamental challenges in applying ultraviolet radiation to microscopy. From the perspective of the optical physicist, specialist beam shaping and objective lenses that permit high-efficiency transmission of ultraviolet radiation are required [11]. These are expensive and often a custom microscope is required that is beyond the financial capability of the standard research laboratory.

Considering biology, direct application of ultraviolet radiation can be extremely harmful to live cells and tissue [12]. In a study by Debarre *et al* [13], it was demonstrated that increased cell survival rates were observed when using an alternative excitation source to single photon excitation of UV excitable molecules. This alternative approach to the application of ultraviolet radiation is to use two photon absorption. Here, photons of approximately double the wavelength are simultaneously absorbed by the sample to provide the energy required for a single-photon transition. It has been demonstrated that greater depth penetration and increased cell viability may be provided by using two photon excitation [14]. Moreover, the use of two photon absorption can overcome the need for specialist ultraviolet optics and minimises photo-damage to biological tissues [13, 15]. Additional benefits when specifically applied to UV excitable dyes such as DAPI include reduced bleach rates and greater contrast [16].

As described briefly in Chapter 1, the traditional source applied in two photon excitation imaging is the femtosecond-pulsed Ti:Sapphire laser [12]. It can deliver average powers larger than 1W with pulse durations shorter than 200 fs and

wavelength tuning spanning from 690 – 1050 nm. The wide tuning range allows the user to identify the wavelength which corresponds to the peak two-photon absorption of a given fluorophore. Although the Ti:Sapphire laser source is widely wavelength tunable, performance for excitation of short-wavelength absorbing molecules is limited. The shortest emission wavelength, of around 700 nm is comparable in most cases to a single photon absorption wavelength of > 350 nm, yet many molecules, such as Indo-1 and Hoechst Blue have peak absorption wavelengths < 350 nm. For other molecules, due to inavailability of laser systems, the peak two photon excitation wavelength remains uncertain. For example, in a study by Huang *et al* [17], two-photon excitation of the endogenous fluorophores NAD(P)H and Flavoprotein was investigated using a Ti:Sapphire laser. The wavelength dependence of two photon excitation action cross section was highlighted (replicated in Fig. 5.1).

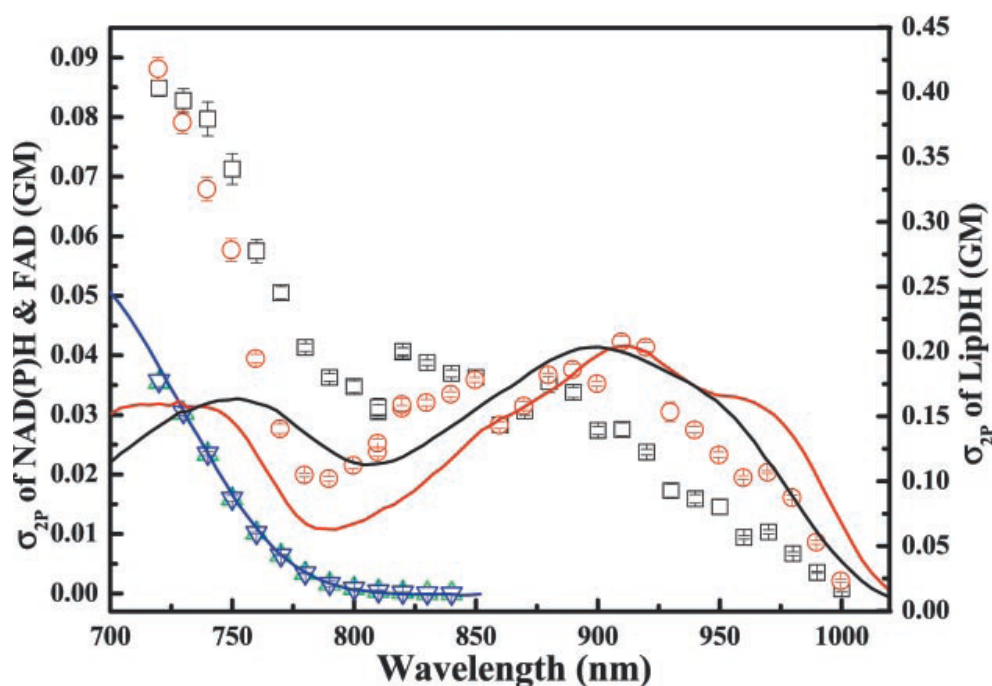


Figure 5.1 Two photon excitation action cross section of NAD(P)H (green triangles) as a function of Ti:Sapphire wavelength (Reproduced from [17]).

Figure 5.1 highlights the tuning range of a Ti:Sapphire plotted against the output fluorescence intensity. In this figure green triangles represent the output from

NAD(P)H. At shorter excitation wavelengths a reduction in Ti:Sapphire wavelength results in a higher fluorescent output. When reaching the lower wavelength tuning limit of the Ti:Sapphire laser, it is unclear from the analysis of Fig. 5.1 if the output has reached a maximum. This suggests that greater outputs may be achieved when using wavelengths shorter than the Ti:Sapphire can provide.

Sum Frequency Mixing (SFM), introduced in Chapter 2, may be used as a method for the generation of an ultra-short pulsed source which has a wavelength below the capabilities of a commercial Ti:Sapphire laser.

This chapter covers three aims; the construction and characterisation of a SFM source at a wavelength of ~ 630 nm, the application of the same source for two photon laser scanning microscopy, and provide a comparison of effectiveness between the Ti:Sapphire and the SFM source.

5.2 Sum frequency mixing: Theory

When considering the electrodynamics of materials like those used in nonlinear optics, the use of Maxwell's equations is required. They may be manipulated in order to describe the response of a material to an incident electric field. This is provided by use of the de-coupled wave equation

$$-\nabla^2 \tilde{E}_n + \frac{\epsilon^{(1)}(\omega_3)}{c^2} \frac{\partial^2 \tilde{E}_n}{\partial t^2} = -\frac{4\pi}{c^2} \frac{\partial^2 \tilde{P}_n^{NL}}{\partial t^2}. \quad (5.1)$$

where P_n^{NL} is the nonlinear polarisation field and $\varepsilon^{(l)}(\omega_3)$ being the linear dielectric constant. Throughout this analysis, tilde represents a field which is rapidly varying in time.

In the case where two strong incident beams, at frequencies ω_1 and ω_2 , are propagated, in the z direction, through a nonlinear medium, a new frequency component may be generated ω_3 , which is the sum of both frequencies. This is caused by the nonlinear atomic response of the medium. The plane wave equation describing the electric field of a beam induced in such an interaction may be shown, in terms of amplitude, is given by Boyd [18]

$$\tilde{E}_3(z, t) = A_3(z, t)e^{i(k_3z - \omega_3t)} + c.c., \quad (5.2)$$

where it is assumed that the amplitude of the electric field, $A_3(z, t)$ is a slowly varying and the wave vector k is described by

$$k_3 = \frac{n_3\omega_3}{c}, \quad n_3 = \sqrt{\varepsilon^{(l)}(\omega_3)}. \quad (5.3)$$

The nonlinear source term may be represented by the following

$$\tilde{P}_3(z, t) = 4d_{eff}A_1(z, t)A_2(z, t)e^{i(k_1+k_2-\omega_3t)} + c.c. \quad (5.4)$$

By substituting Eq. (5.2) and (5.4) into Eq (5.1) and simplifying, we arrive at the following relationship

$$\frac{d^2 A_3(z, t)}{dz^2} + 2ik_3 \frac{dA_3(z, t)}{dz} = \frac{-16d_{eff}\omega_3^2}{c^2} A_1(z, t)A_2(z, t)e^{i(k_1+k_2-k_3)z}. \quad (5.5)$$

At this a point the slowly varying amplitude approximation (SVAA) may be applied (Eq. (5.6)). This allows the second derivative, with respect to time, in Eq. (5.5), to be neglected since

$$\left| \frac{\partial^2 A_3(z, t)}{\partial z^2} \right| \ll \left| k_3 \frac{\partial A_3(z, t)}{\partial z} \right|. \quad (5.6)$$

By using the SVAA, the second derivative term may be ignored and Eq. (5.5) becomes

$$\frac{\partial A_3(z, t)}{\partial z} = \frac{8\pi d_{eff}\omega_3^2}{k_3 c^2} A_1(z, t)A_2(z, t)e^{i\Delta k z} \quad (5.7)$$

In the event where phase matching is perfect ($\Delta k = 0$), $A_3(z, t)$ increases linearly upon propagation through the z direction, in turn resulting in a squared increase in the intensity due to

$$I = \frac{nc}{2\pi} |E_1||E_2| \quad (5.8)$$

thus, the nonlinear intensity is always the highest when the phase matching condition is met.

When considering the interaction of the propagating beams within a SFM process it is important to consider not only the effect of the input beam upon the output, but also the effect that the output beam has upon the inputs. Equivalent equations for each may be represented by the following

$$\frac{\partial A_1(z,t)}{\partial z} = \frac{8\pi d_{eff} \omega_1^2}{k_1 c^2} A_3(z,t) A_2^*(z,t) e^{i\Delta k z} \quad (5.9)$$

and

$$\frac{\partial A_2(z,t)}{\partial z} = \frac{8\pi d_{eff} \omega_2^2}{k_2 c^2} A_3(z,t) A_1^*(z,t) e^{i\Delta k z} . \quad (5.10)$$

For these coupled amplitude equations, it was assumed that the propagation E-field incurred zero losses through the dielectric medium and that the effective nonlinear susceptibility d_{eff} is constant for each equation.

5.3 Sum frequency mixing: Geometries

A variety of geometries including single pass, intra-cavity or within an external cavity may be used for increased efficiency. This section looks to identify the most appropriate method for this application.

5.3.1 Single pass pumping

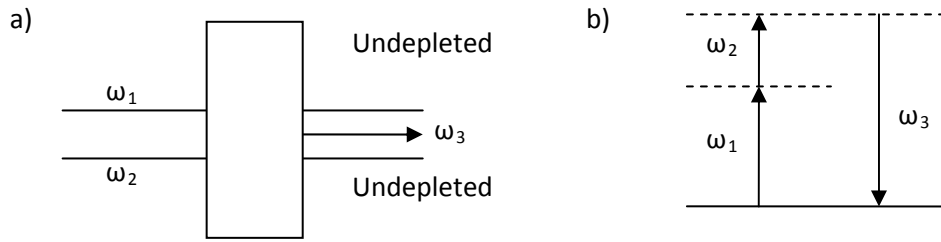


Figure 5.2 a) Single pass SFM within a nonlinear crystal b) Energy level illustration of SFM

Single pass SFM geometries are perhaps the simplest configuration for frequency conversion. Figure 5.2 illustrates two pump beams of differing frequencies ω_1 and ω_2 focused into a nonlinear crystal in order to produce a third frequency, ω_3 , equal in energy to that of the two pump beams combined. The output intensity of ω_3 in a single pass conversion may be calculated under the assumption of zero pump depletion [19]:

$$I(\omega_3, l) = \frac{2\omega_1\omega_2 d_{eff}^2 l^2}{n_{\omega_3} n_{\omega_1} n_{\omega_2} c^3 \epsilon_0} \left(\frac{\sin(\Delta kl/2)}{\Delta kl/2} \right) I(\omega_1) I(\omega_2) \quad (5.11)$$

Despite its simplicity, single pass SFM has been shown to provide useful outputs in the visible range [20], support the creation of femtosecond pulses [21] and provide conversion efficiencies in excess of 30 % [22]. Control over the output wavelength for SFM is dictated by the phase matching conditions and conservation of energy described in chapter 2. The nonlinear crystals used for SFM are also subject to the same acceptance tolerances as those described in section 2.2.5.

5.3.2 Extra-cavity pumping

An alternative geometry for SFM can be achieved through placing the mixing crystal within an external resonator, such as that illustrated in Fig 5.3. Reflection of the generated wavelength back upon itself leads to the formation of a standing wave. Mode matching of the pump beams to the SFM cavity allows for efficient build-up of power within the cavity. Having a partially-reflecting mirror at the SFM wavelength allows greater power to be extracted from the resonator than is possible in the single pass case. This is particularly so when impedance matching is applied, i.e. where the transmission of the input mirror is equal to the sum of all other losses with the cavity [23].

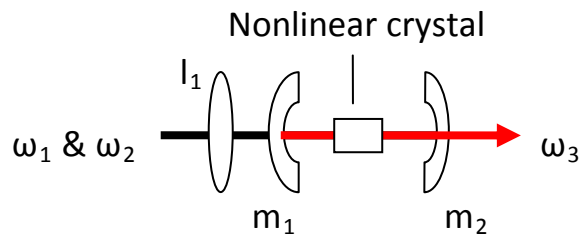


Figure 5.3 An example of an external SFM enhancement cavity. Pump beams ω_1 and ω_2 are required to be temporally overlapped. Lens l_1 is used for mode-matching. Cavity mirrors m_1 and m_2 are HR at ω_3 .

In the case where double refraction is ignored, the power transmitted through the output coupler P_t , can be given by

$$P_t = \frac{tP_{NR}}{(1-r)^2 + 4r \sin^2 \frac{\varphi}{2}}, \quad (5.12)$$

where, t is the power transmission coefficient, P_{NR} is the SFM power within a cavity in the non-resonant state, r is a power reflection coefficient determined by the reflections within the crystal and φ is the round trip phase shift within the resonator.

At resonance $\varphi = 0$, and hence the resonant enhancement ratio for output SFM power is given by

$$\frac{P_t}{P_{NR}} = \frac{t}{(1-r)^2}. \quad (5.13)$$

Enhancement cavities have been applied extensively throughout nonlinear optics [24-27]. With application of external cavities, conversion efficiencies of SFM in excess of 90% have been reported [28]. However, there can be issues with standing wave enhancement cavities. By creating a standing wave, the cavity allows for complete saturation of the gain at the peaks of the resonant wave. Conversely, at the troughs of the wave, no gain saturation occurs, this effect is known as spatial hole burning [23]. This can lead to competing modes depleting gain, resulting in issues with single frequency operation and laser efficiency. Additionally, wavelength tuning and ultra-short pulse generation can be problematic with the occurrence of spatial hole burning. One solution to this, which is commonly used in commercial lasers, is the implementation of a ring resonator. Instead of the light folding back upon itself, as with a standing wave resonator, a ring configuration implements a travelling pump wave around an enclosed system. This negates the possibility of spatial hole burning and allows for uniform saturation of gain throughout the crystal, thus favouring a single longitudinal mode. In order to permit uni-directionality, an optical isolator is typically introduced into the resonator. Along with increased efficiency, the uni-directionality of a ring laser allows all generated light to be extracted from a single output coupler without any losses incurred from reverse propagation. Despite the advantages of ring resonators, they are notoriously difficult to align and have low tolerance to misalignment.

5.3.3 Intra-cavity pumping

When looking to extract optimal SFM power from a crystal and efficient nonlinear conversion, it is important to ensure that pump intensities are as high as possible whilst remaining below the damage threshold of the nonlinear crystal. When high intensities are not possible in a single pass geometry, a good option is to place the nonlinear crystal within the laser cavity. This concept was first demonstrated in 1963 by Wright [29] who made use of the higher intensity within a laser resonator for intra-cavity SHG. In doing so, unconverted light stays within the cavity whilst the generated nonlinear frequency may be extracted through use of a specially-designed output coupler.

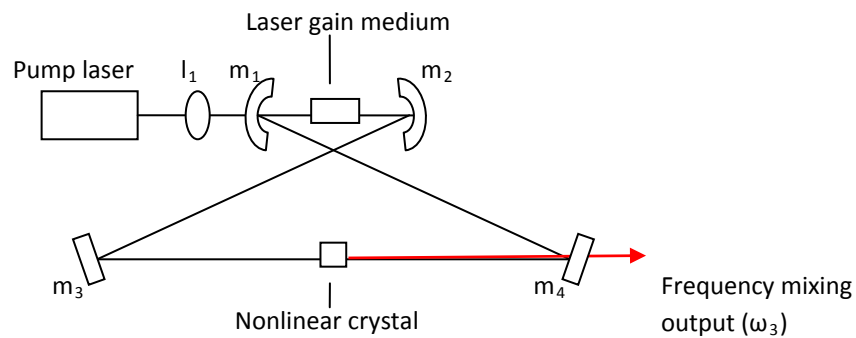


Figure 5.4 An example of an intra-cavity SFM geometry. Element I_1 is a lens for mode-matching and m_{1-4} are cavity mirrors highly reflecting at the two wavelengths supported by the laser gain medium (ω_1 and ω_2). Additionally, m_4 is transparent at ω_3 and acts as an output coupler.

Through judicious choice of resonator design, laser gain media such as Nd:YAG or Nd:YVO₄ may be simultaneously operated at two independent laser lines [30, 31]. The presence of a secondary frequency within a laser cavity may also be achieved through the introduction of an additional nonlinear crystal for frequency doubling [32]. The presence of two frequencies resonating within a cavity provides a useful pump source for intra-cavity SFM. Such geometries have been shown to generate visible wavelengths [33] with high output powers [32]. By placing a nonlinear crystal

inside of a resonator which is either doubly resonant [33] or has an additional nonlinear process occurring such as SHG [32], it is possible to expose the crystal to higher pump powers resulting in greater conversion. Despite the benefits of placing a nonlinear crystal with a laser resonator, it has been noted that chaotic power fluctuations are often incurred when using this method for increasing efficiency [34, 35].

An additional form of intra-cavity SFM is that commonly experienced is that produced within an SPOPO resonator [36, 37]. Due to the multiple wavelengths which are generated in the parametric process, SFM is often found to be a by-product of the system. This can result in ultra-short pulse generation at the SFM frequency and may be optimised to extract the greatest power. Using this technique, it has proven possible to couple the SFM light into a microscope platform and perform two photon excitation imaging [20, 37]. As the SPOPO nonlinear crystal is not designed to be phase matched at the SFM frequency the process has poor efficiency. Output powers were therefore restricted to $< 15\text{mW}$ at the sample. However, average powers of up to 50 mW at the sample tend to be used as the upper limit for multiphoton excitation with regards to saturation of a fluorophore (assuming excitation is provided by a typical $< 200\text{ fs}$ -pulsed Ti:Sapphire laser) [38].

Despite the greater efficiency offered by external- and intra-cavity SFM, their application tends to be with cw or Q-switched pump lasers [28, 33, 39]. These lasers do not provide high peak intensities and thus these alternative methods of increasing efficiency are essential.

With widespread availability of ultra-short pulsed laser sources, high peak powers are already available and can therefore be used with a simpler single pass SFM geometry.

5.4 Sum frequency mixing: Experiment

In order to perform the SFM process required to provide a wavelength suitable for efficient two photon excitation source for UV excitable samples, two pump sources of different frequencies are required. The first pump beam, ω_1 (which will be referred to as the ‘pump’ beam), was a single pass SPOPO, the same as that described in Chapter 4. As described in the single pass configuration, the pump source for the OPO provided 2 W of average power. Due to the damage threshold of the OPO crystal, only 1 W of the source could be utilised. The additional, unused, 1 W from this source was implemented as the second pump source, ω_2 (which will be termed the ‘fundamental’ beam) for SFM generation. The experimental setup for this is shown in Fig. 5.5.

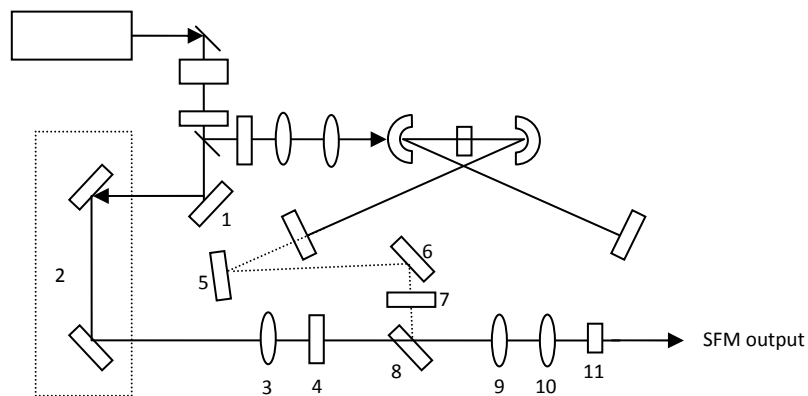


Figure 5.5 System diagram of SFM of a SPOPO and Yb-doped fibre laser. Numbered elements are additions to the system shown in Chapter 4.

Component	Description
1	Beam steering mirror (HR @ 1064 nm)
2	Delay line

3	Collimating lens ($f = 150$ mm, AR coated @ 1064 nm)
4 & 7	Half-wave plates
5 & 6	Beam steering mirror (HR @ 1.4 – 1.6 μm)
8	Beam steering mirror (HR @ c, HT @ 1064 nm)
9 & 10	Mode matching optics (63 mm & 75 mm, AR coated at 1.4 – 1.6 μm)
11	PPLN crystal stored within a home-built oven (1 mm long, 1 mm thick), $A = 10.9$ μm , uncoated.

Table 5.1 List of new components applied in Fig. 5.5.

With use of beam shaping optics (elements 3, 9 and 10) and the use of a time delay (element 2) it was possible to spatially and temporally overlap the fundamental and pump beams. The OPO provided 200 mW of average power to the crystal over a wavelength range of 1.45 – 1.6 μm , and the 1064 nm source provided 750 mW, following loss experienced upon propagation through the optics solely coated for wavelengths greater than 1.4 μm . Lenses with coatings at both of these wavelengths were unavailable. Both beams were focused into a nonlinear crystal, in order to generate SFM.

Due to its high nonlinearity, damage threshold and wide transmission band, PPLN was selected as the nonlinear crystal for SFM. With reference to the Sellmeier equations and acceptance parameters described in Chapter 2, input wavelengths of $\omega_1 = 1530$ nm $\omega_2 = 1064$ nm may be used to generate an output of $\omega_3 = 630$ nm within the QPM PPLN crystal. Fig. 5.6 shows the tuning of pump ω_1 (SPOPO) which permit phase matching with a constant pump frequency of ω_2 (Yb:doped fibre laser). Both sources were described previously in Chapter 4.

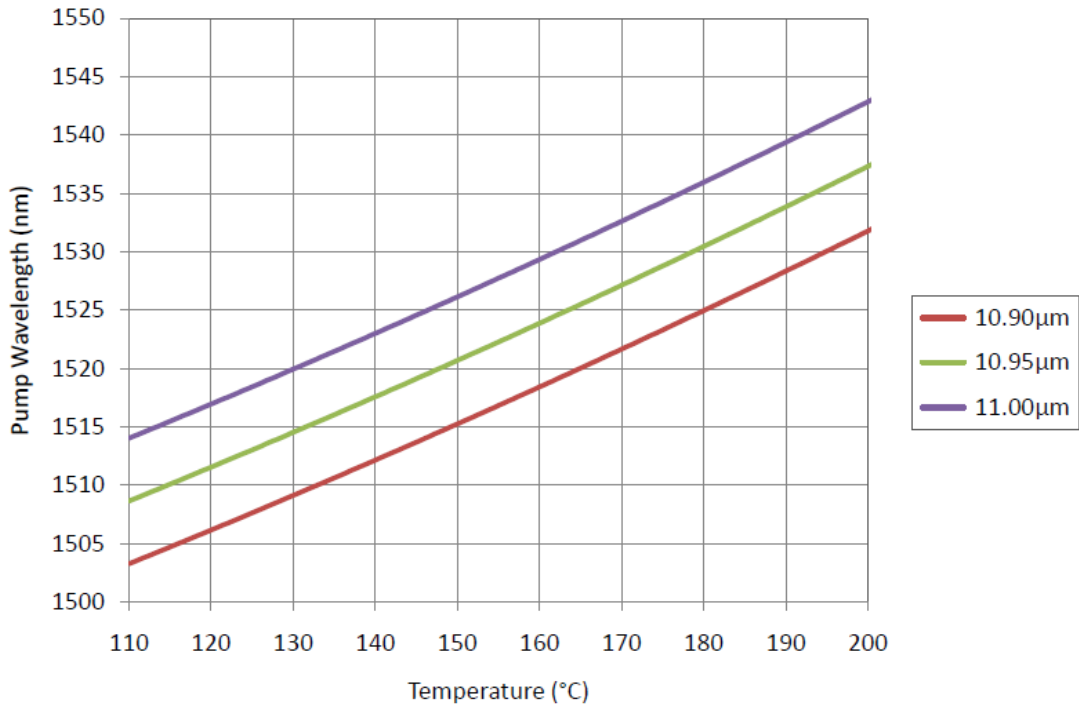


Figure 5.6 The variables required for a fixed $\omega_2 = 1064 \text{ nm}$ to produce an output $\omega_3 = 630 \text{ nm}$. Including ω_1 , temperature and period length.

The crystal was 1mm long (approx. one coherence length) determined by Eq. (2.15), with a period length of 10.9 μm and kept at a temperature of 160 $^{\circ}\text{C}$ in order to satisfy phase matching conditions. A spectral acceptance of 11 nm and temperature acceptance of 12 K were calculated for this crystal using the equations given in Section 2.9. Due to commercial limitations the crystal could not be anti-reflection (AR) coated at both of the input wavelengths.

This source was designed for use with the life sciences and despite the large increase in signal when applying the source to the reference sample, it was of interest to analyse the response from a biological samples.

A comparison between the SFM source and Ti:Sapphire, operating it its lowest wavelength (710 nm), was carried out for a biological sample. A mouse kidney

(Invirogen, fluocells prepared slide 3) which was labelled with DAPI was used in this analysis. As with the reference sample, 20 mW of average power and ~ 350 fs pulse durations were used for both sources.

For comparative studies, a commercial fs pulsed Ti:Sapphire laser (Coherent, MIRA 900F) was also available as a source of excitation. This laser provided an output average power of ~ 400 mW with a wavelength tuning range of 710 – 800 nm and pulse durations < 200 fs (repetition rate of 76 MHz and spectral width ~ 10 nm).

5.5 Sum frequency mixing: Results

A benefit of using an OPO as one of the pump sources a SFM experiment was the ability to vary the wavelength in order to optimise and manipulate the phase matching condition. In conjunction with the control of the temperature of the SFM PPLN, the wavelength of the SFM output can therefore be altered whilst maintaining a zero phase mismatch. Application of the experimental setup described in Section 5.4, a SFM wavelength tuning range of 622 – 636 nm was achieved. Fig 5.7 shows the SFM average output power corresponding to input OPO wavelength, at varying temperatures of the SFM crystal.

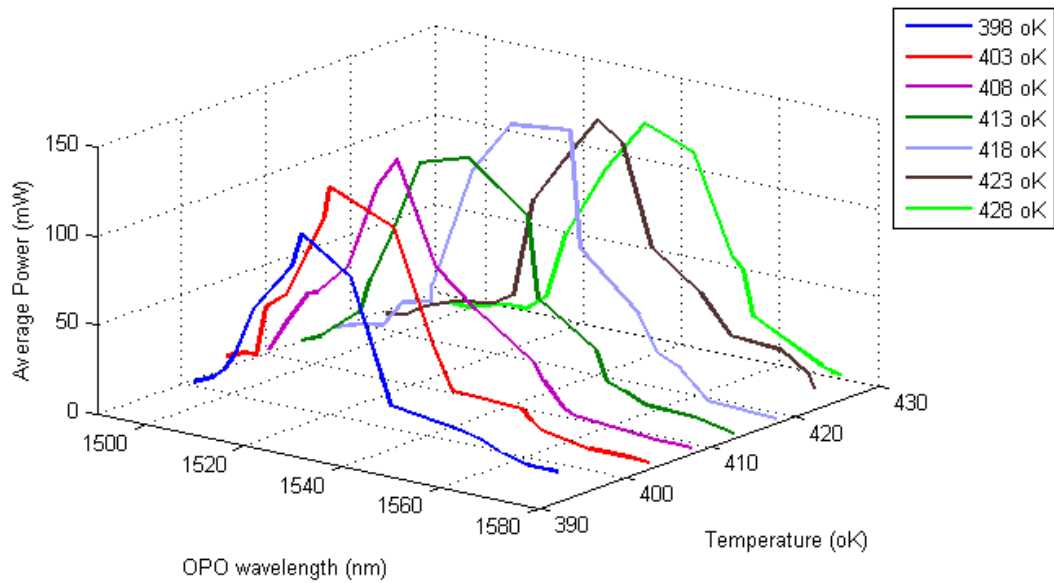


Figure 5.7 Average SFM power dependence upon the signal output from the SPOPO for varying temperatures of SFM crystal.

The maximum average output power from the SFM process generated 150 mW at a wavelength of 630 nm. This condition corresponded to a pump wavelength of 1538 nm and a SFM crystal temperature of 418 °K. Tuning of the SPOPO signal was achieved through a combination of temperature tuning and period length selection. For each wavelength an average signal power of 200 mW was applied. Signal wavelengths which were below 1500 nm and above 1570 nm generated negligible powers. This was also the case of SFM crystal temperatures below 398 °K and above 428 °K.

In order to achieve greatest SFM conversion, it was necessary to ensure temporal overlap of the two pump beams within the crystal. This was achieved through control of a delay line seen in element 2 from Fig. 5.5.

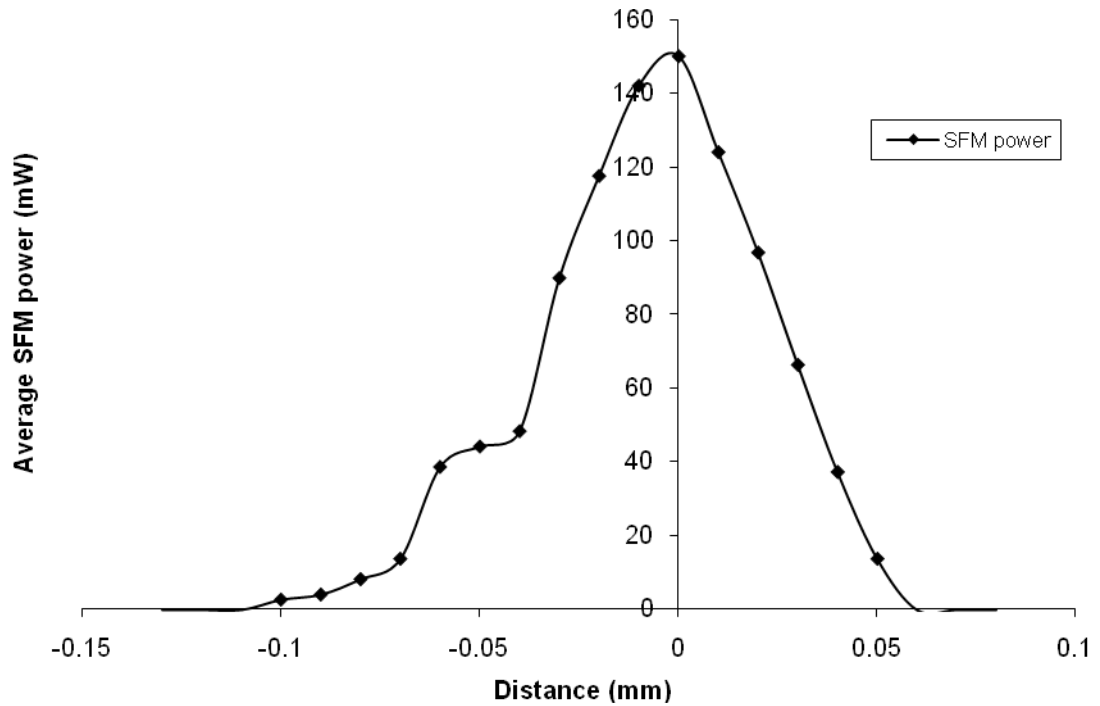


Figure 5.8 Average SFM power as a function of temporal overlap of the two pump beams.

At a constant wavelength of 630 nm, the FWHM range of overlap was found to span over approximately 60 μm . Over this range pulse durations measured 390 – 420 fs. This figure highlights the importance of the temporal overlap of pump pulses for ultra-short pulsed SFM experiments.

With use of a variable neutral density filter to incrementally increase power, it was possible to determine the dependence of the generated SFM average power upon both the 1064 nm and 1530 nm sources, as seen in Fig. 5.9 & 5.10.

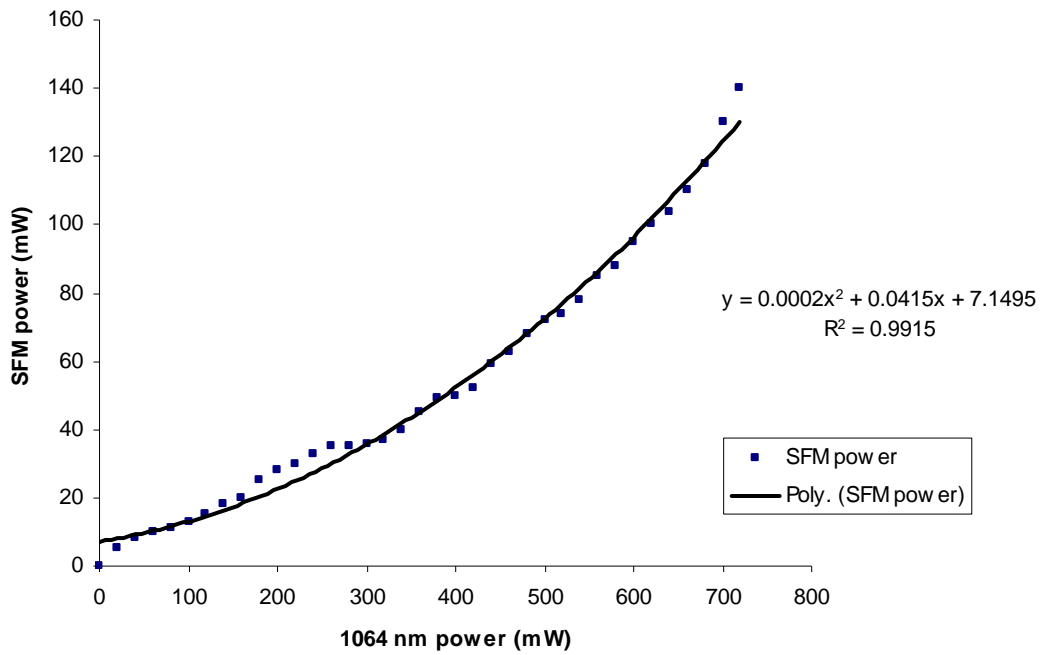


Figure 5.9 Plot of SFM average power as a function of 1064 nm pump power (constant OPO power 200 mW)

Incremental changes of 20 mW to the 1064 nm average power resulted in the SFM power closely following a squared relation as was expected from this nonlinear interaction ($R^2 = 0.9915$).

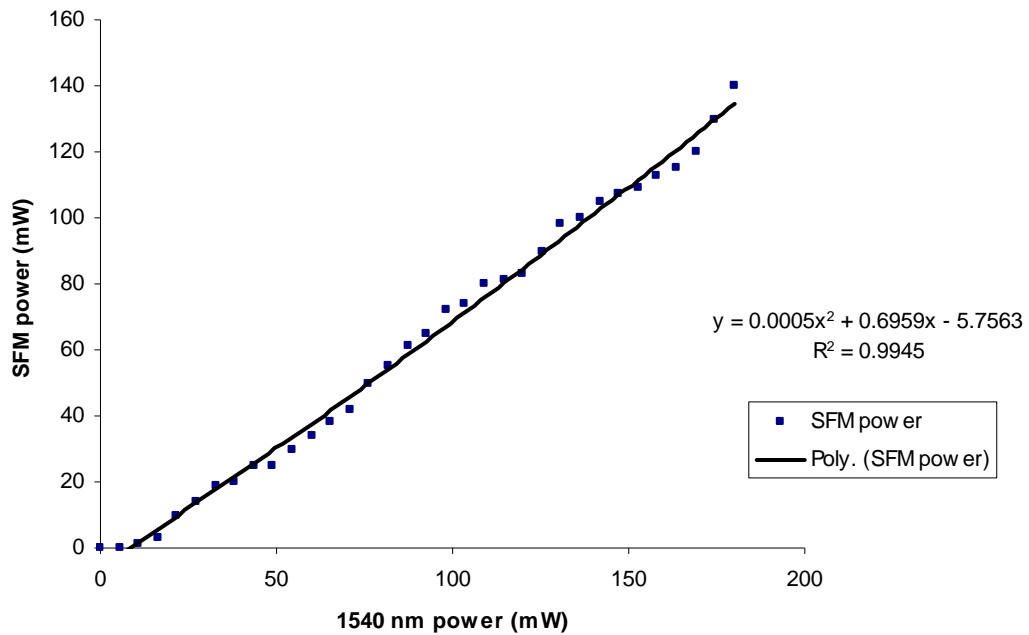


Figure 5.10 Plot of SFM average power as a function of 1530 nm pump power (constant 1064 power 750 mW)

Resultant SFM average power generated, with incremental changes of 5 mW to the 1530 nm input average power, was plotted. It could be seen that the power dependence closely followed a squared fit ($R^2 = 0.9945$).

The results from Fig. 5.9 and 5.10 follow the expected dependence of pump power upon the SFM process as highlighted by Eq. (5.8).

5.6 Application and comparison of a Ti:Sapphire laser and a SFM source for two photon microscopy: Experiment

Non-commercial excitation sources often experience high optical loss when coupled into commercial microscopes. This is due to the optics within not being designed for operation at the wavelengths or pulse durations, which has previously seen to provide

up to 80 % losses in the IR [40, 41]. For this purpose, a home-built inverted laser scanning microscope was used in order to minimise these losses.

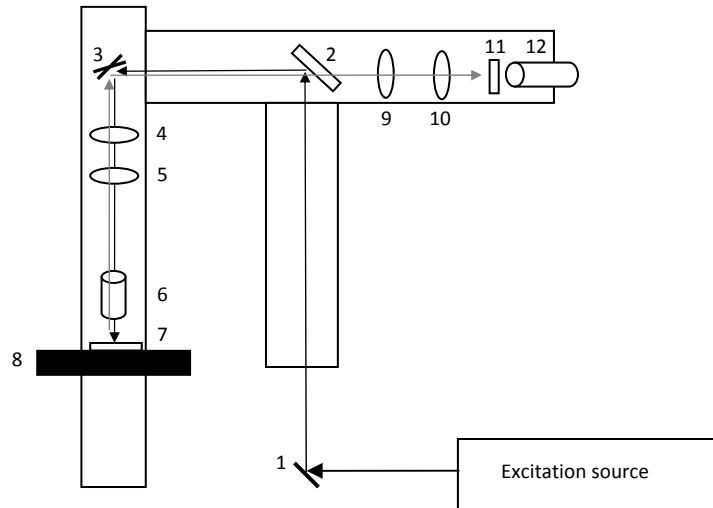


Figure 5.11 Home built microscope in a two photon configuration

Component	Description
1	Input beam steering mirror (HR @ visible)
2	40/60 beamsplitter (visible)
3	Galvo-scanning mirrors (General Scanning, M-series)
4 & 5	Beam expander ($f = +50$ mm & $f = +100$ mm lenses AR coated @ visible)
6	Objective lens (20x 0.75 NA), Olympus
7	Sample slide
8	X – Y translation stage
9 & 10	Imaging lenses ($f = +75$ mm, AR coated @ visible)
11	550 nm SP filter (85 % transmission, OD > 2), Edmund optics

12	PMT (spectral range $\lambda = 200 - 850$ nm, gain: 0.8 kV), Electron Tubes, (no longer commercially available, similar systems available from Hamamatsu)
----	---

Table 5.2 List of components applied for the home-built inverted laser scanning microscope in Fig. 5.11.

By inserting an aperture at the focus prior to the PMT, the system may be used as a confocal microscope, but as two photon excitation was being implemented, an optical sectioning aperture was not required. A flipper mirror prior to element 1 provided a method of alternating between 630 nm and Ti:Sapphire excitation whilst maintaining the imaging region of interest. Control of the average power applied to the sample was achieved with use of a variable neutral density filter.

The first sample, which was used as a reference to determine levels of two photon emission, was a paper labelled with the fluorescent dye ‘Page Blue’ (provided by Dr Brad Amos, MRC). Although absorption and emission spectra were not available for this sample, this was chosen only as a reference prior to imaging biological specimens. Strong fluorescence resulted from single photon UV excitation under epi-fluorescence illumination and the fibres in the paper were useful contrast indicators. Moreover, this three-dimensional structure was useful to confirm the inherent optical sectioning provided by two photon excitation.

The second sample analysed was a commercial biological sample. This was a mouse kidney slice (Invitrogen, fluocells prepared slide 3) labelled with the fluorophore DAPI. DAPI is a commonly used fluorophore within life sciences as a cell nuclei indicator. Absorption and emission spectra are given in Fig 5.12.

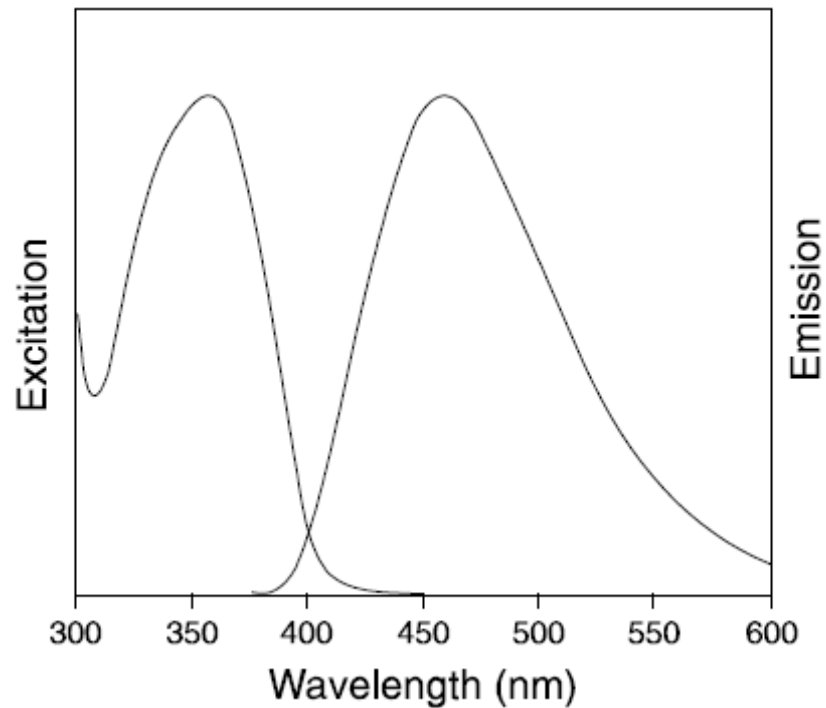


Figure 5.12 DAPI absorption/emission spectra (courtesy of Invitrogen)

As DAPI is excitable in the UV, it is of particular interest for two photon excitation using the wavelengths provided by the SFM setup.

Before application of the SFM source to UV excitable samples, it was of interest to determine if the commonly used fluorophore DAPI, exhibited the same wavelength dependency as that seen in NAD(P)H.

To achieve this, a commercial fs pulsed Ti:Sapphire laser (Coherent, MIRA 900F) was coupled into the homebuilt microscope. This was applied as the source for two photon excitation of the mouse kidney sample labelled with DAPI. Using a constant power of 20 mW at the sample it was possible to extract the intensity of fluorescence from each image plot against varying wavelengths produced by the Ti:Sapphire. The laser supported mode-locking over a wavelength range of 710 – 800 nm. With use of

a neutral density filter, an average power of 20 mW was supplied to the sample and images acquired at each 10 nm increment over this range.

In order to quantify levels of fluorescence produced by samples, the average grayscale intensity was analyzed from by each image. These grayscale values were extracted from each image using Metamorph in the same fashion as was used for image analysis in Chapter 3.

5.7 Application and comparison of a Ti:Sapphire laser and a SFM source for two photon microscopy: Results

Figure 5.13 highlights the fluorescence response of the Page Blue paper sample with application of the Ti:Sapphire laser at varying wavelengths. For each image, excitation conditions were kept constant in order to provide comparable outputs ($P_{av} = 20$ mW, $\tau = 350$ fs and $\Delta\nu = 76$ MHz).

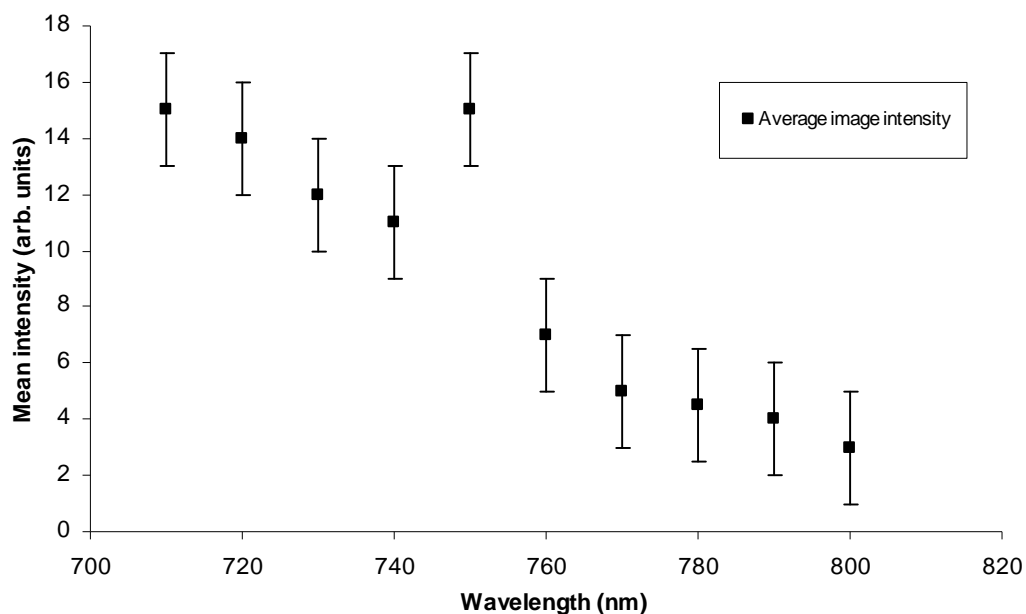


Figure 5.13 Plot of the fluorescence intensity obtained from a UV excitable sample (Page Blue) versus Ti:Sapphire wavelength tuning .

The average grayscale intensity of each image was plotted as a function of wavelength in Fig. 5.13. It was apparent that the trend observed by Huang *et al*, who applied a similar Ti:Sapphire source to NAD(P)H, is reflected in this data. Again, it is uncertain whether the two photon excitation wavelength has peaked at the lowest wavelength provided by the range of a Ti:Sapphire. It is therefore of interest to investigate whether more efficient fluorescence generation could be obtained with use of a lower wavelength source for two-photon excitation of DAPI. The error in Fig. 5.13 represents one standard deviation of the intensity across each image, which was extracted from analysis in Metamorph.

Upon optimisation of the $P_{av} = 150$ mW, 630 nm source, it was then coupled into the home-built microscope described in Section 5.4. Following a steering mirror, a beam splitter is used to split the beam with 40 % reflectance and 60 % transmission. The transmitted beam was dumped, whereas the 60 mW reflected beam was sent to the

galvo-scanning mirrors. The beam was then passed through a beam expander, and finally to an objective lens.

The objective lens chosen was a 20x, air lens with a 0.75 NA. This was to permit a wide field of view whilst providing a high numerical aperture for, as described by Abbe's equation (Eq. 1.3) in Chapter 1. Using this setup, it was possible to provide up to 32 mW of average power to the sample at a wavelength of 630 nm. With use of a variable neutral density filter, it was possible to alter the excitation power supplied to the reference sample. No averaging was performed in the acquisition of these images and the gain was kept constant throughout.

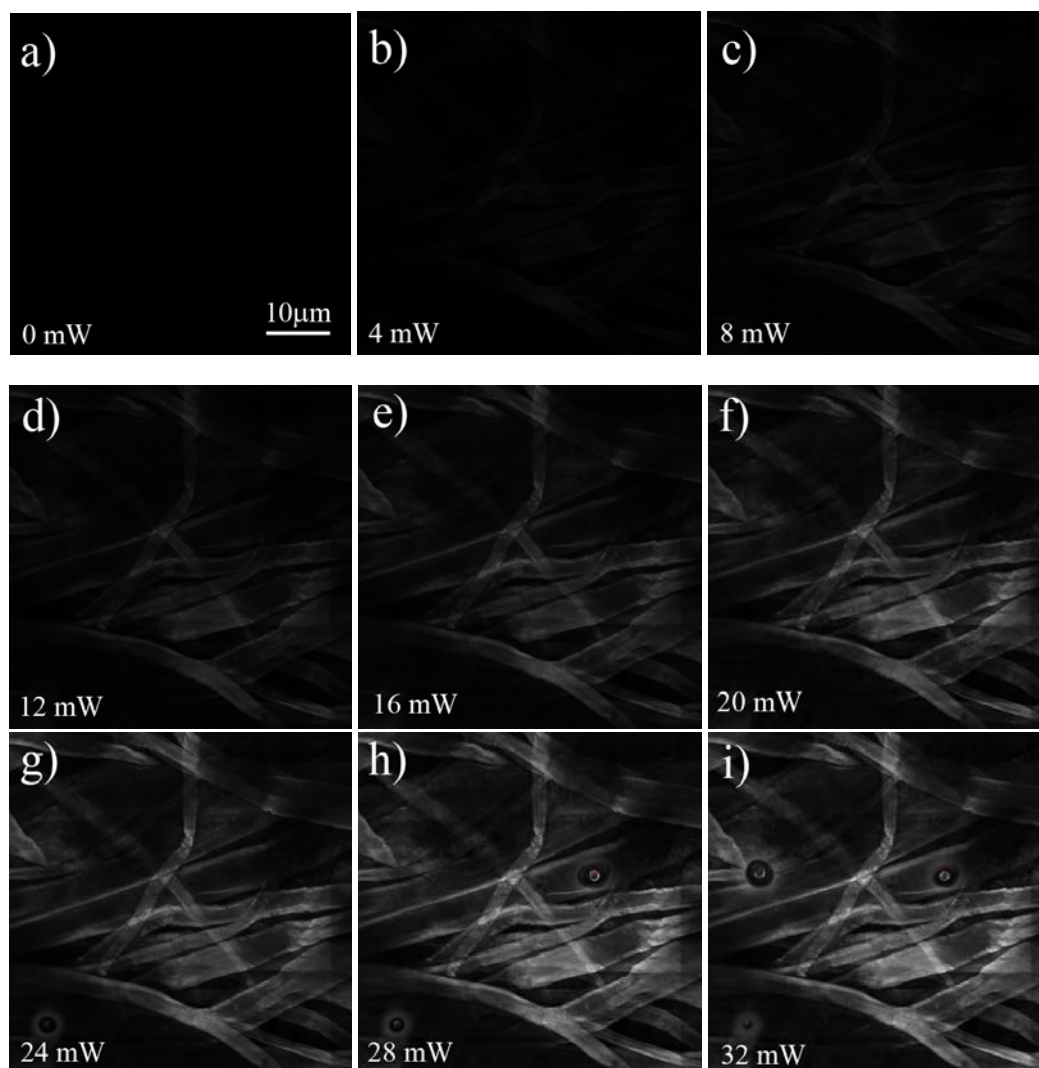


Figure 5.14 (a-i) Two photon images of Page Blue fluorescent paper at incremental SFM average powers

Power scaling of the sample allowed determination of the relation between excitation power and emitted fluorescence, as shown in Fig 5.15.

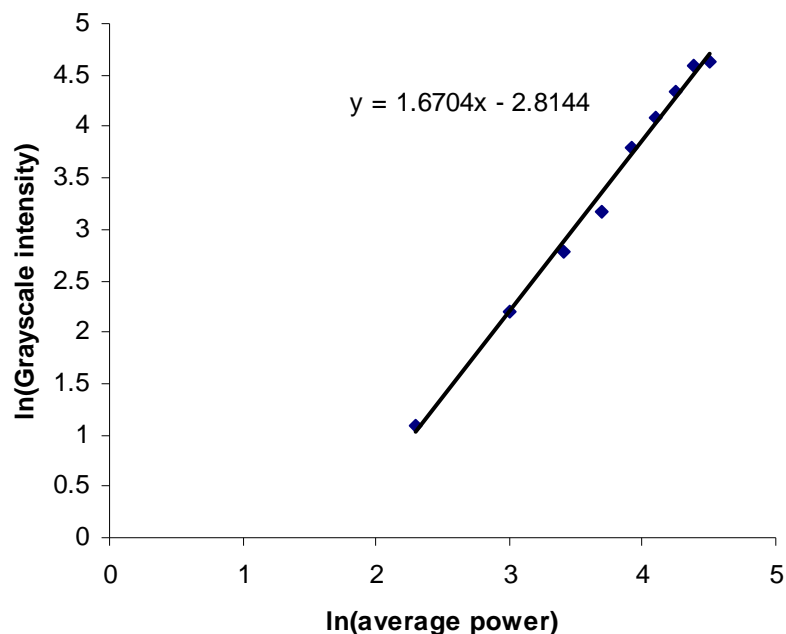


Figure 5.15 ln/ln plot of fluorescence intensity against average excitation power

Using Metamorph image analysis software, it was possible to extract average image intensities from those shown in Fig. 5.14. By taking the natural logarithm of both the fluorescence intensity and their corresponding average power for these images, it was possible to generate a plot highlighting the power relation between each of these values.

The data extracted from the images in Fig. 5.14 yield a 'best fit' linear gradient of 1.67. With a standard deviation of 10 %, this value falls below the expected value of 2 [14] for the two photon process, it is also noted that average power in excess of 20

mW resulted in damage to the paper sample (highlighted in Fig. 5.14 g, h and i) which will greatly reduce the fluorescence induced by the laser.

Despite the lack of electronically-controlled translation of the objective lens within the home-built microscope, it was possible to adjust the position of the lens manually using a micrometer. Incremental translation allowed for approximate z-stacking of the sample.

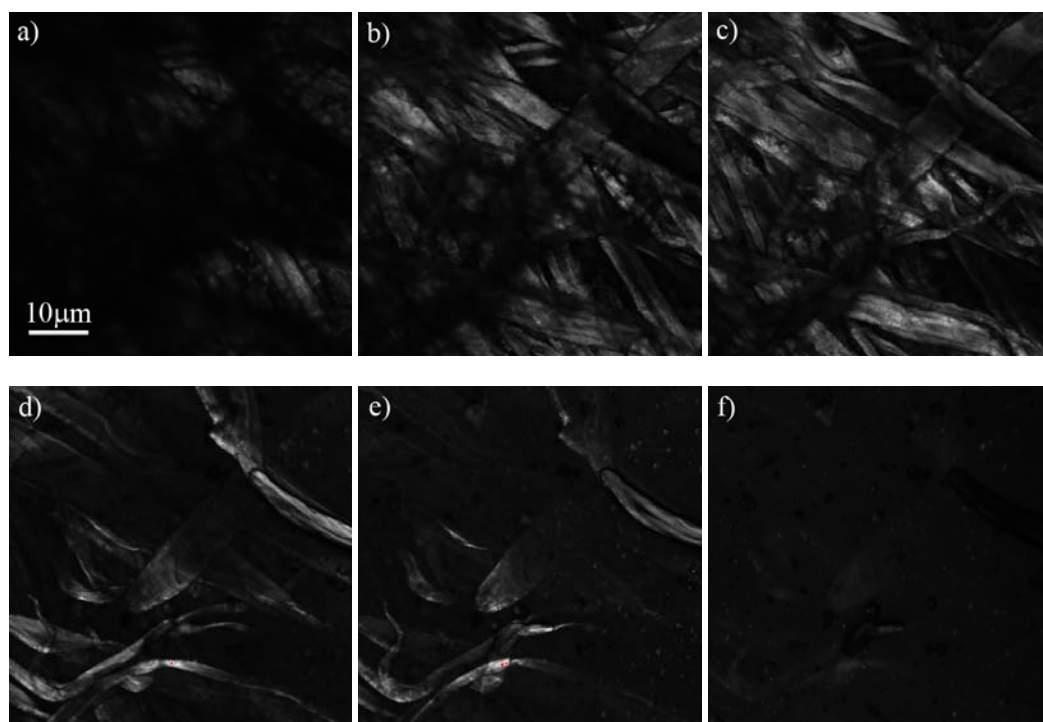


Figure 5.16 Approximate two photon optical-sectioning of fluorescent paper (Page Blue)

Translating over 50 µm in the z-direction, it was possible to use the inherent optical sectioning provided by two photon excitation to image different layers of the paper. This was apparent from the different fibres which became visible at each depth of focus.

Limited resolution in the translation stage controlling the axial position of the microscope objective lens has restricted the increments to 10 μm . Nonetheless, the inherent optical sectioning capability of two photon imaging could still be demonstrated.

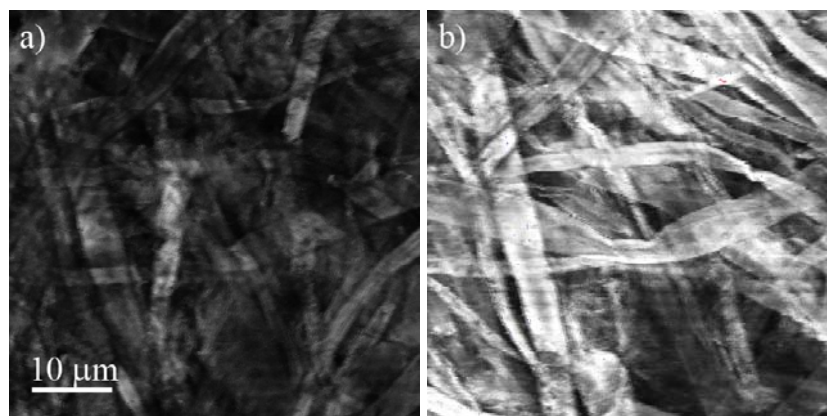


Figure 5.17 Reference sample with irradiation using; a) 710 nm Ti:Sapphire and b) 630 nm SFM source, at the same image acquisition settings.

Comparable average power (20 mW) and pulse durations (~ 350 fs) were applied to the sample for imaging using the home-built microscope system. Whilst maintaining the plane of focus, it was possible to see substantially more fluorescence from the 630 nm source. This could be quantified by comparison of the average grayscale intensities of each image, which gave respective values of 32 and 117 for the Ti:Sapphire and 630 nm source. This marks at least a three fold increase in the fluorescence generated by the sample, merely by judicious choice of the two-photon excitation wavelength.

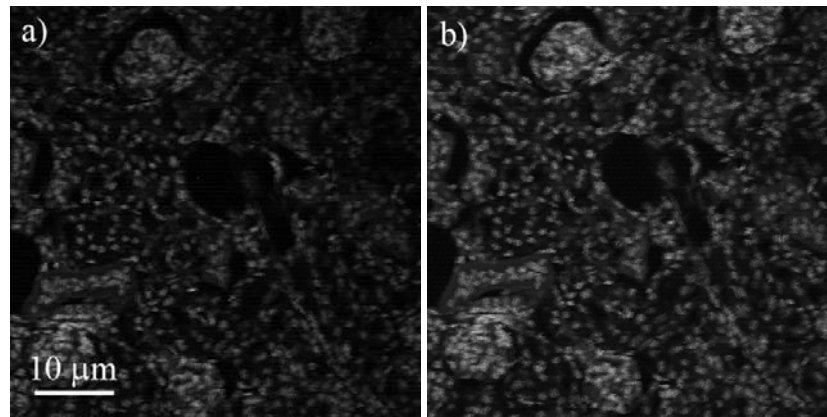


Figure 5.18 Mouse kidney labelled with DAPI under irradiation from a) Ti:Sapphire (710 nm) and b) 630 nm source.

Figure 5.18 shows (a) fluorescence generated by the Ti:Sapphire source at 710 nm when compared to (b) the 630 nm source. Average intensity grayscale values were measured for each image a) 9 and b) 15 (arbitrary grayscale units). This corresponded to ~ 65% increase in fluorescence when applying the 630 nm source. This highlighted the usefulness of a sub-Ti:Sapphire wavelength source biological imaging of UV excitable samples.

In addition to the various UV excitable dyes which are used, it is also common for tissues and botanical samples to autofluoresce. Some examples of autofluorescence are given below for a mollusc radula, a prunus leaf and marine algae.

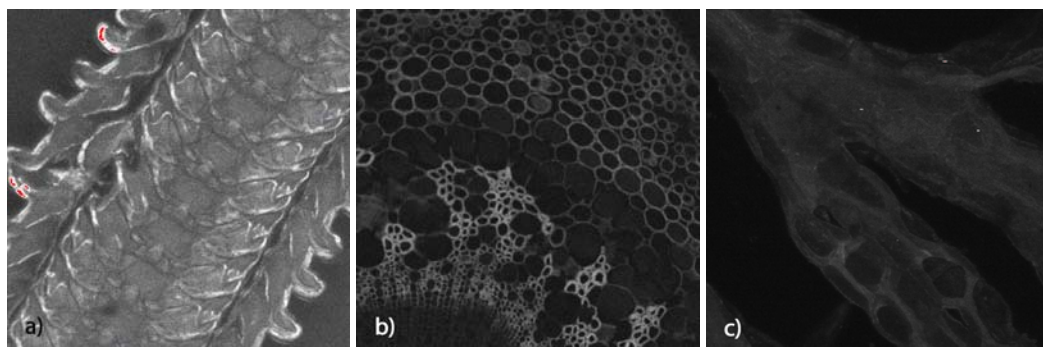


Figure 5.19 Two photon autofluorescence imaging from a) snail radula, b) Prunus leaf and c) Marine Algae.

Each of these samples applied 16 times averaging and they show the suitability of this source to many UV excitable samples. All images were acquired using the 20 mW at the sample and using a 20x objective lens (0.75 NA).

5.8 Conclusion

It has been shown that there is a need for ultra-short pulsed sources at wavelengths below the tuning range of Ti:Sapphire laser for two photon excitation of UV excitable samples; UV dyes and autofluorescence. A wavelength tunable (622 – 636 nm), sub-400 fs source was presented as an alternative source for excitation at these wavelengths. The source was generated through the sum frequency mixing of an SPOPO and an Yb-doped fibre laser.

The SFM source was then coupled into a home-built microscope and applied to various samples. Two photon excitation was confirmed through the standard technique of a \ln/\ln plot of the average fluorescence intensity and average power. This obtained a value of 1.67, which despite being below the expected value of 2, suggested that the signal was generated through two photon excitation. Issues with saturation may have accounted for this inconsistency. The capacity for use of this source and microscope for optical sectioning was also demonstrated. Despite the crudeness of the sectioning capability, this could be easily rectified with the purchase and incorporation of a piezo onto the objective lens mount. This would permit true 3D reconstruction of fluorescent samples.

When applying this source to a UV reference sample, a three fold increase in fluorescence intensity was measured when comparing the SFM source to a Ti:Sapphire source under the same operational conditions. The same comparison was

applied to a biological sample and yielded an increase in fluorescence of at least ~ 65 %.

These improvements highlight that smaller wavelength lasers may be constructed to perform more efficiently than the standard two photon Ti:Sapphire source for excitation of UV excitable samples. Additionally, at a fraction of the cost of commercial OPO systems, the source is financially much more appealing. Therefore serious consideration must be taken when deciding upon the purchase of microscope systems for UV excitable two photon imaging.

5.9 References

1. Zelent, B., T. Troxler, and J. Vanderkooi, *Temperature Dependence for Fluorescence of β -NADH in Glycerol/Water Solution and in Trehalose/Sucrose Glass*. Journal of Fluorescence, 2007. **17**(1): p. 37.
2. Huang, Z., Zheng, S. Xie, R. Chen, H. Zeng, D. I. McLean and H. Lui, *Laser-induced autofluorescence microscopy of normal and tumor human colonic tissue*. International Journal of Oncology, 2004. **24**(1): p. 59.
3. Kobayashi, M., R. Sawada, and Y. Ueda, *Spectroscopic imaging and the characterization of the autofluorescence properties of human bronchus tissues using UV laser diodes*. IEEE Journal of Selected Topics in Quantum Electronics, 2003. **9**(2): p. 142.
4. König, K., G. Flemming, and R. Hibst, *Laser-induced autofluorescence spectroscopy of dental caries*. Cellular and molecular biology (Noisy-le-Grand, France), 1998. **44**(8): p. 1293.
5. Yu, Q. and A. Heikal, *Two-photon autofluorescence dynamics imaging reveals sensitivity of intracellular NADH concentration and conformation to cell physiology at the single-cell level*. Journal of Photochemistry and Photobiology B: Biology, 2009. **95**(1): p. 46.

6. Lichtman, J.W. and J.-A. Conchello, *Fluorescence microscopy*. Nature Methods, 2005. **2**(12): p. 910.
7. Cao, X. and S. Arthur, *High-power and reliable operation of vertical light-emitting diodes on bulk GaN*. Applied Physics Letters, 2004. **85**: p. 3971.
8. Zhang, C., G. Yu, and Y. Cao, *Long operating life for polymer light-emitting diodes*. 1998, Google Patents.
9. Hanaki, K., A. Momo, T. Oku, A. Komoto, S. Maenosono, Y. Yamaguchi and K. Yamamoto, *Semiconductor quantum dot/albumin complex is a long-life and highly photostable endosome marker*. Biochemical and Biophysical Research Communications, 2003. **302**(3): p. 496.
10. Young, D., R.C.Y. Auyeung, A. Piqué, D.B. Chrisey, and D.D. Dlott, *Time-resolved optical microscopy of a laser-based forward transfer process*. Applied Physics Letters, 2001. **78**: p. 3169.
11. Keller, H., *Objective lenses for confocal microscopy*. Handbook of Biological Confocal Microscopy, 2006: p. 145.
12. Pawley, J., *Handbook of biological confocal microscopy*. 1995: Plenum Press.
13. Débarre, D., W. Supatto, A.-M. Pena, A. Fabre, T. Tordjmann, L. Combettes, M.-C. Schanne-Klein and E. Beaurepaire, *Imaging lipid bodies in cells and tissues using third-harmonic generation microscopy*. Nature Methods, 2005. **3**(1): p. 47.
14. Denk, W., J. Strickler, and W. Webb, *Two-photon laser scanning fluorescence microscopy*. Science, 1990. **248**(4951): p. 73.
15. Lakowicz, J., *Topics in Fluorescence Spectroscopy: Nonlinear and two-photon-induced fluorescence*. 1997: Plenum Press.
16. Sako, Y., A. Sekihata, Y. Yanagisawa, M. Yamamoto, Y. Shimada, K. Ozaki and A. Kusumi, *Comparison of two-photon excitation laser scanning microscopy with UV-confocal laser scanning microscopy in three-dimensional calcium imaging using the fluorescence indicator Indo-1*. Journal of Microscopy, 1997. **185**(1): p. 9.
17. Huang, S., A. Heikal, and W. Webb, *Two-photon fluorescence spectroscopy and microscopy of NAD (P) H and flavoprotein*. Biophysical Journal, 2002. **82**(5): p. 2811.

18. Boyd, R., *Nonlinear optics*. 2008: Academic Press.
19. Franken, P., A.E. Hill, C.W. Peters, and G. Weinreich, *Generation of optical harmonics*. Physical Review Letters, 1961. **7**(4): p. 118.
20. Champert, P.A., S.V. Popov, A.V. Avdokhin and J.R. Taylor, *Sum frequency generation of synchronously-seeded, high-power Yb and Er fiber amplifiers in periodically poled KTP*. Applied Physics Letters, 2002. **81**(20): p. 3732.
21. Zhao, H., P. Wang, J. Zhu, Q. Du, and Z. Wei, *Sum-frequency generation between an actively synchronized ultrashort Ti:sapphire laser and a Nd:YVO₄ laser*. Journal of the Optical Society of America B, 2008. **25**(7): p. B39.
22. Taverner, D., P. Britton, P. G. R. Smith, D. J. Richardson, G. W. Ross, and D. C. Hanna, *Highly efficient second-harmonic and sum-frequency generation of nanosecond pulses in a cascaded erbium-doped fiber:periodically poled lithium niobate source*. Optics Letters, 1998. **23**(3): p. 162.
23. Siegman, A., *Lasers*. 1986: University Science Books.
24. Taverner, D., P. Britton, P. G. R. Smith, D. J. Richardson, G. W. Ross, and D. C. Hanna, *Highly efficient second-harmonic and sum-frequency generation of nanosecond pulses in a cascaded erbium-doped fiber: periodically poled lithium niobate source*. Optics letters, 1998. **23**(3): p. 162.
25. Watanabe, M., K. Hayasaka, and H. Imajo, *Sum-frequency generation near 194 nm with an external cavity by simultaneous enhancement of frequency-stabilized fundamental lasers*. Japanese Journal of Applied Physics, 1994. **33**(3B): p. 1599.
26. Bienfang, J., C.A. Denman, B.W. Grime, P.D. Hillman, G.T. Moore, and J.M. Telle, *20 W of continuous-wave sodium D~ 2 resonance radiation from sum-frequency generation with injection-locked lasers*. Optics Letters, 2003. **28**(22): p. 2219.
27. Vance, J., C. She, and H. Moosmüller, *Continuous-wave, all-solid-state, single-frequency 400-mW source at 589 nm based on doubly resonant sum-frequency mixing in a monolithic lithium niobate resonator*. Applied optics, 1998. **37**(21): p. 4891.
28. Mimoun, E., L. De Sarlo, J-J. Zondy, J. Dalibard, and F. Gerbier, *Sum-frequency generation of 589 nm light with near-unit efficiency*. Optics Express, 2008. **16**(23): p. 18684.

29. Wright, J.K., *Enhancement of second harmonic power generated by a dielectric crystal inside a laser cavity*. Proceedings of the IEEE, 1963. **51**(11): p. 1663.
30. Chen, Y.F., *cw dual-wavelength operation of a diode-end-pumped Nd:YVO₄ laser*. Applied Physics B: Lasers and Optics, 2000. **70**(4): p. 475.
31. Shen, H., *Simultaneous multiple wavelength laser action in various neodymium host crystals*. IEEE Journal of Quantum Electronics, 1991. **27**: p. 2315.
32. Haiyong, Z., Z. Ge, H. Chenghui, W. Yong, H. Lingxiong, and C. Zhenqiang, *Multi-watt power blue light generation by intracavity sum-frequency-mixing in KTiOPO₄ crystal*. Optics Express, 2008. **16**(5): p. 2989.
33. Fu, X., H.H. Tan, Y.M. Li, E.J. Hao, G. Shen and L.S. Qian, *Efficient generation of a CW 593.5-nm laser by intracavity sum-frequency mixing with a BiB₃O (BIBO) crystal*. Laser Physics, 2007. **17**(12): p. 1345.
34. Kretschmann, H.M., F. Heine, G. Huber and T. Halldorsson, *All-solid-state continuous-wave doubly resonant all-intracavity sum-frequency mixer*. Optics Letters, 1997. **22**(19): p. 1461.
35. Baer, T., *Large-amplitude fluctuations due to longitudinal mode coupling in diode-pumped intracavity-doubled Nd:YAG lasers*. Journal of the Optical Society of America B, 1986. **3**(9): p. 1175.
36. Jensen, O.B., M. Bruun-Larsen, O. Balle-Petersen, and T. Skettrup, *Yellow nanosecond sum-frequency generating optical parametric oscillator using periodically poled LiNbO₃*. Applied Physics B: Lasers and Optics, 2008. **91**(1): p. 61.
37. McConnell, G., G.L. Smith, J.M. Girkin, A.M. Gurney, and A.I. Ferguson, *Two-photon microscopy of fura-2-loaded cardiac myocytes with an all-solid-state tunable and visible femtosecond laser source*. Opt. Lett., 2003. **28**(19): p. 1742.
38. Diaspro, A., P. Bianchini, G. Vicidomini, M. Faretta, P. Ramoino and C. Usai, *Multi-photon excitation microscopy*. BioMedical Engineering OnLine, 2006. **5**(1): p. 36.
39. El-Taher, A.E., Y.H. Tsang, and D.J. Binks, *Intra-cavity second-harmonic and sum-frequency generation in a diode-pumped broadband Yb-doped fibre laser*. Optics Communications, 2006. **266**(1): p. 317.

40. Wei, Z., G. McConnell, and M. Parsons. *Optical parametric oscillator system for CARS microscopy*. in *Lasers and Electro-Optics 2009 and the European Quantum Electronics Conference. CLEO Europe - EQEC 2009*
41. Keatings, S.R., W. Zhang, and G. McConnell, *Characterization of microscope objective lenses from 1,400 to 1,650 nm to evaluate performance for long-wavelength nonlinear microscopy applications*. *Microscopy Research and Technique*, 2008. **71**(7): p. 517.

Chapter 6 AC and DC optical beam induced current microscopy of InGaN light emitting diodes

6.1 Introduction

Light emitting diodes (LEDs) were first introduced as a practical light source by Holonyak in 1962 [1]. Since this time, LEDs have become one of the most commonly used light sources. Through the process of electro-luminescence, whereby a forward biased voltage is applied across the semi-conductor device, electrons from the n-type region combine with the positive ‘holes’ in the p-type region, as described in Chapter 1.3.3., resulting in the emission of a photon. The frequency of this photon is dependent upon the bandgap energy of this transition, $E = \hbar\omega$.

When compared to other illumination sources, various advantages are noted. Lifetimes of LEDs have been shown to be as high as 50,000 hours [2], exceeding that of most fluorescent tubes (~ 10,000 hours) and incandescent sources (~ 1000 hours). Also tailoring of the output emission wavelength may be achieved through the alteration of the semi-conductor composition. In addition, LEDs, unlike alternative light sources, do not radiate large amounts of IR. A small heat sink is enough to maintain the temperature of an LED, resulting in low-cost, compact devices.

One type of LED, with a wide range of visible outputs (400 – 570 nm) is the Indium Gallium Nitride (InGaN) LED [3]. InGaN LEDs have found widespread use across a range of applications including full-colour display, liquid crystal display back lighting and in low-cost mobile platform technologies [3], largely due to the flexibility in wavelength made possible at the design stage. To obtain full benefit from this technology, the many real-world applications to which InGaN LEDs can be applied clearly require optimum device performance, but structural defects and

inhomogeneity across the active region of an LED are often a problem since these may decrease the operational lifetime of the device [4] and may require higher power consumption [5]. Prior to packaging and integration, it is therefore essential to use non-destructive methods to assess the quality of the semiconductor materials within the device, to ensure that only LEDs with good performance reach the end-user.

One technique which may be used for semi-conductor failure analysis is electron beam induced current (EBIC). This technique is based upon the interaction of a focused electron beam and an electrical device (e.g. a semi-conductor). Upon bombardment of the device with the electrons, electron-hole pairs may be generated, allowing for an observable current to be detected [6]. This may then be used to provide information regarding the internal carrier dynamics of the device and defective areas. A serious disadvantage to this method is incurred through the use of the required high energy electrons (~ 20 keV) as the source for inducing the current. This can lead to damage within the device and alteration of its electrical properties [7].

A few non-destructive optical techniques for semiconductor analysis are available. Photo-luminescence imaging, which is perhaps the most widespread method [8-10] and this is applicable to InGaN [11, 12]. This technique can be used to create a surface map of a semiconductor device when performed on a microscope platform, but information is limited, and details of internal carrier dynamics cannot be obtained. Importantly, this presents an obvious restriction when considering fast LEDs and hence is unsuitable for testing many of the emerging devices. This information can however be obtained using a technique known as optical beam induced current microscopy.

Laser scanning optical beam induced current (OBIC) imaging is an alternative non-destructive technique which provides high spatial resolution analysis of the active

region of LEDs [13, 14]. In the simplest form, OBIC requires irradiation of a photo-sensitive semiconductor using a laser source (typically a continuous wave laser) with energy equal to, or greater than, the electronic bandgap of the p-n junction in the device [15]. This results in the creation of electron-hole pairs. A bias voltage is typically also applied across the sample, permitting higher collection efficiency of the generated free carriers via an electrical contact [16]. Lateral raster scanning of the laser source relative to the stationary semiconductor under investigation results in an optically induced current that can be detected and used to provide a surface image in the active region of the device.

When performing OBIC imaging, the signal generated is composed of two current components, one of which is direct current (DC) and the other alternating current (AC). Traditionally, signals in the DC domain have been widely applied throughout semiconductor analysis, due to the straightforward methods of detection [17] in both one photon and two photon geometries. In 1999, Xu *et al* demonstrated that the application of one photon geometries to OBIC yielded lower signal to noise as a result of the increase in scattered light when compared to a two photon geometry [18]. Additional advantages of the two photon process were shown to include the spatial confinement of carrier generation, resulting in more accurate imaging and the possibility for increased spatial resolution [18].

As a method to obtain additional information from a given device, it can be of interest to analyse AC component of the response. This was first demonstrated in an experiment in a one photon geometry by Kao *et al* [16], where it was highlighted that, uniquely, this technique could provide a spatially resolved frequency response to excitation of the active region of a device in real-time. Together, application of AC and DC OBIC techniques allows mapping of the electronic properties of the active region along with details of the structural integrity of the active layer. By measuring the optoelectronic response of a device, details regarding the homogeneity

and quality of the device can be obtained which would not be available through purely optical methods.

In this chapter, AC and DC OBIC was performed on a single imaging platform to analyse the active region of a green emitting InGaN LED. We perform one photon and two photon DC OBIC and also two photon AC OBIC of the same sample to provide a comparison and evaluation of the DC and AC methods for studying InGaN LEDs. This includes information regarding the one photon and two photon DC spectral response, the AC spectral response, modulation frequency and phase variations across the LED, from which we determine the best methods for studying InGaN LEDs.

6.2 Theory of AC detection

AC OBIC signals require an alternative method of detection as to that used for DC detection. Noise levels for the generated AC component from an OBIC signal are higher than that for DC components and consequently, direct measurement techniques are not applicable. Implementation of a lock-in amplifier provides a method to isolate a signal, ω_{sig} , from noise using phase sensitive detection (PSD). A signal generator provides a fixed frequency of excitation, whilst providing a reference frequency, ω_{ref} , for detection. This reference is used to provide an internal reference, which is generated via a phase-locked loop. Following amplification, the signal can then be multiplied by the lock-in reference.

The PSD provides two outputs from the signal, one at $(\omega_{ref} + \omega_{sig})$ and the other at $(\omega_{ref} - \omega_{sig})$. With the use of a low pass filter and in the case where, $\omega_{ref} = \omega_{sig}$, the product of these outputs results in a DC signal which is proportional to its amplitude, $V_{psd} \sim V_{sig} \cos(\theta)$. Here, θ is the phase difference between the signal and the lock-in

reference and V_{sig} is the amplitude of the signal. Any noise which is not equal to the reference frequency is fully attenuated.

The phase dependence of this output can be eliminated with use of a second PSD measuring a reference frequency shifted by 90° . In this case, signal amplitude is given by; $V_{psd2} \sim V_{sig} \sin(\theta)$. Using V_{psd} and V_{psd2} , the magnitude of the signal vector, R , can be calculated, as the phase dependence (which cannot be directly measured) is eliminated.

$$R = (V_{psd}^2 + V_{psd2}^2)^{1/2} = V_{sig} \quad (6.1)$$

The phase difference between the signal and the lock-in can also be calculated using the following:

$$\theta = \tan^{-1}(V_{psd2} / V_{psd}) \quad (6.2)$$

6.3 Experimental method

To perform both AC and DC OBIC imaging of InGaN LEDs, a galvanometer-mirror based laser scanning inverted microscope platform (Fluoview FV300 and IX-81, Olympus) was used.

To facilitate comparison of the different OBIC techniques, the same sample was used throughout the study. The sample was a commercial InGaN LED (Epistar, Venus series), the dimensions and structure of which is shown in Fig. 6.1.

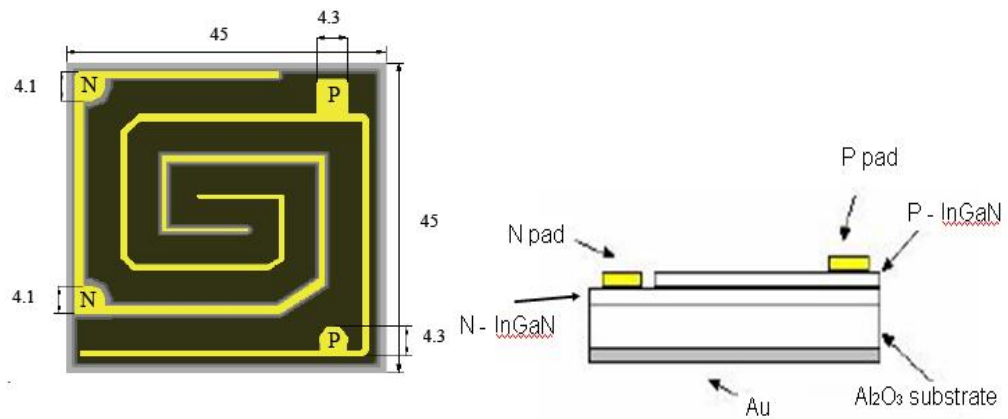


Figure 6.1 Illustrations of the dimensions and structure of the sample LED. Dimensions are in microns

The peak emission wavelength from this LED was found at 525 nm with a bandwidth of 35 nm (FWHM). This was measured using a compact spectrometer (Ocean Optics, USB2000), with a spectral resolution of 0.5 nm.

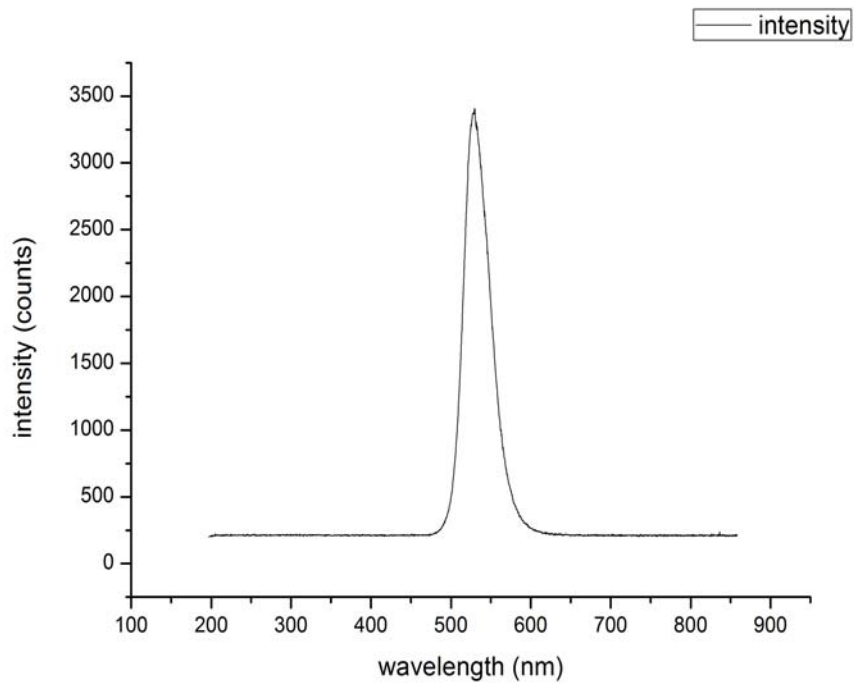


Figure 6.2 Wavelength emission from InGaN LED

6.3.1 One photon and two photon DC OBIC: Experiment

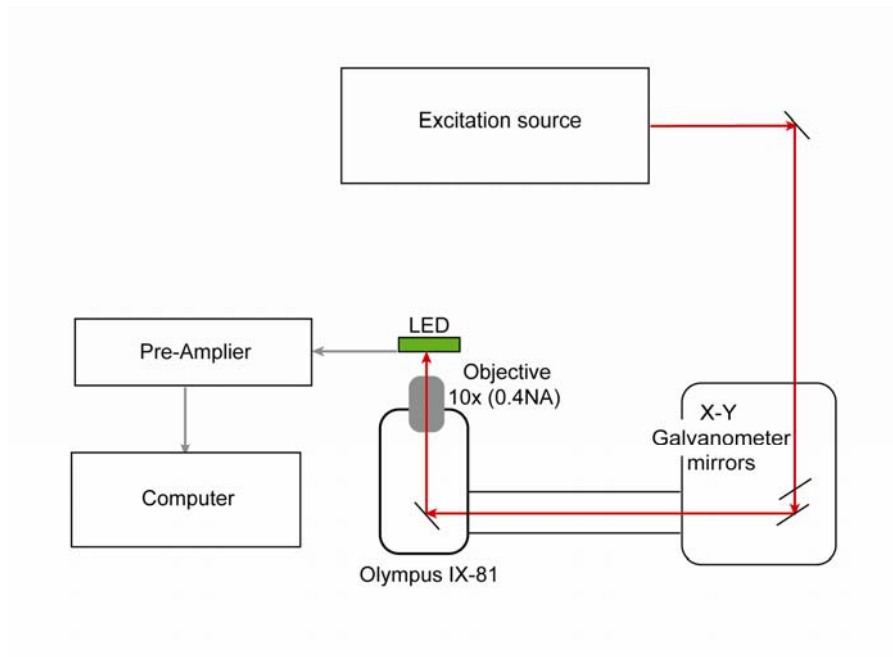


Figure 6.3 Schematic diagram of DC OBIC.

The experimental configuration for DC OBIC is shown in Fig. 6.3. A 10x objective lens (0.4 NA) was used to provide an image of the full active region while maintaining high lateral spatial resolution. The LED was mounted upon a 3-axis high-precision mount in order to align the device perpendicular to direction of laser excitation to ensure that excitation and resultant images were obtained from within the active region and not buffer or substrate layers. Upon irradiation, the current induced within the LED was on the nanoampere scale and was therefore directly sent to a current pre-amplifier (Stanford Research Systems, SR570), allowing the signal to be amplified and then digitized for data processing.

When performing one photon DC OBIC, the generic excitation source described in Fig. 6.3 was a white-light SC source (Fianium, SC400), providing a broadband source ranging from 400 nm to the near-infrared. Pulse durations of approximately 5 ps at a repetition rate of 20 MHz allowed the source to be treated as a continuous wave source. This was used in conjunction with appropriate bandpass interference filters with a peak spectral transmission of $\lambda = 420, 450, 490, 520, 550$ and 580 nm each with ~ 50 % transmission and a bandwidth of 15 nm (Comar) in order to determine the optimal wavelength for maximum DC OBIC signal generation.

In order to stimulate two photon absorption required for two photon DC OBIC, the excitation source was replaced by an ultra-short pulsed Ti:Sapphire laser (Coherent, Mira 900-F, Coherent Verdi V10 pump). The Ti:Sapphire laser provided a conveniently accessed continuous wavelength tuning range from 720 to 900 nm, with pulse durations of approximately 200 fs at a repetition rate of 76 MHz.

Variations in average power across the spectral ranges for both one photon and two photon DC OBIC were experienced (shown in tables 1 & 2). Neither the SC source or the Ti:Sapphire laser source provided the same output power across the available wavelength range. To compensate for this change in excitation power, a linear

scaling relationship between excitation power and generated signal was used for one photon excitation, and a quadratic scaling relation was used when considering two photon excitation [18].

Filter (nm)	Sample power
420	0 W
450	400 nW
490	200 nW
520	1.4 μ W
550	19.5 nW
580	1.9 μ W

Table 6.1 One photon DC OBIC power provided at sample for selected wavelengths

Wavelength (nm)	Sample power (mW)
750	34
760	35
770	38
780	35
790	35
800	30
810	35
820	35
830	34
840	33
850	33
860	32
870	32
880	28
890	26

Table 6.2 Two photon DC OBIC power provided at sample for selected wavelengths

6.3.2 Two photon AC OBIC: Experiment

The system shown in Fig. 6.3 was amended to perform AC detection. In this experiment, the PSD described in section 6.2, was provided with use of a lock-in amplifier. Additionally, as the frequency of pulses from the same Ti:Sapphire laser as used for DC OBIC was in the MHz range, any AC signal generated would be cut off by a large inherent capacitance. In order to reduce the modulation frequency, an electro-optic modulator (EOM) driven by a frequency generator (Stanford Research Systems, SD345) was introduced along with an RF lock-in amplifier (Stanford Research Systems, SR844), as shown in Fig. 6.4.

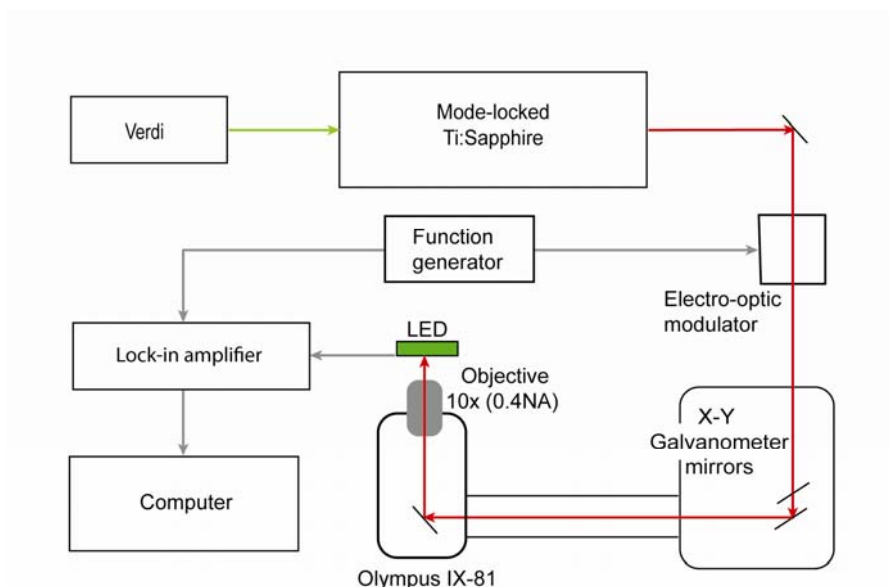


Figure 6.4 Schematic diagram of two photon AC OBIC. An electro-optic modulator was introduced to reduce the repetition rate of the Ti:Sapphire laser, along with a lock-in amplifier in order to detect the AC signal

The EOM was used to control modulation frequency in order to determine the site-specific AC response from the sample. Since the EOM used in these experiments was designed for use at NIR wavelengths, application of the EOM to the visible

wavelengths of the supercontinuum source resulted in large losses. Consequently, upon reaching the sample there was insufficient excitation power available to perform one photon AC OBIC imaging.

Although the EOM was designed for NIR wavelengths, an optical loss of approximately 15 % was measured. This provided average power in excess of 25 mW at the sample, which was sufficient for two photon excitation. As a result, the two photon AC OBIC signal could be collected and used to create a 2D image of the active region of the sample. For this experiment, the EOM could provide useful excitation frequencies ranging from 200 - 850 kHz.

6.4 Analysis method

Upon laser scanning of the LED, electron-hole pairs are generated. This induced current is relative to the scanning position of the beam. Following this, the current was amplified and digitised permitting the scanning software (Fluoview, Olympus) to convert the signal into an 8-bit grayscale image of the active region. This was achieved by assigning relative 'intensity' values to the magnitude of the signal, ranging from values of 0-255.

As a method to determine the homogeneity of the active region of the LED, data from five regions of interest (ROI) were analysed. A ROI at each of the four sides of the image of the active region was chosen along with an ROI in the centre of the image in order to provide a spread of data throughout the sample. With use of image analysis software (Metamorph 7.7, Universal Imaging), it was possible to extract numerical data from the average grayscale intensities produced by the OBIC images within the areas of interest.

6.5 Results and discussion

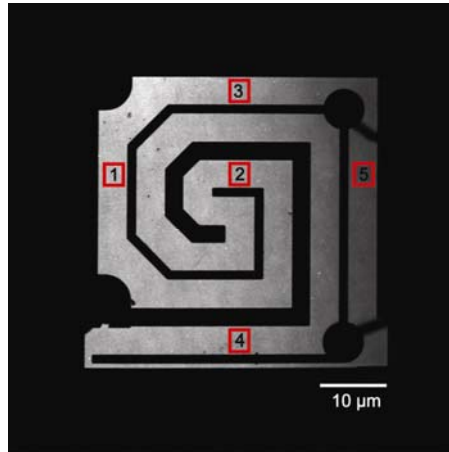


Figure 6.5 OBIC image of LED with five labeled ROIs

An example OBIC image is shown in Fig. 6.5, highlighting the five relative ROIs which were analysed for each image. Upon collection of these OBIC greyscale images, Metamorph was used to calculate the average intensity within selected areas and to also provide values for the standard deviation of the intensity within each ROI.

6.5.1 DC spectral response: one photon DC OBIC

Using the broadband properties of the SC source combined with the previously described optical bandpass filters, it was possible to provide an indirect comparison of one photon and two photon DC OBIC signal level. As described in Section 6.3.1., any fluctuations in one photon excitation power were compensated for using a linear relation and all data was normalised to the largest intensity.

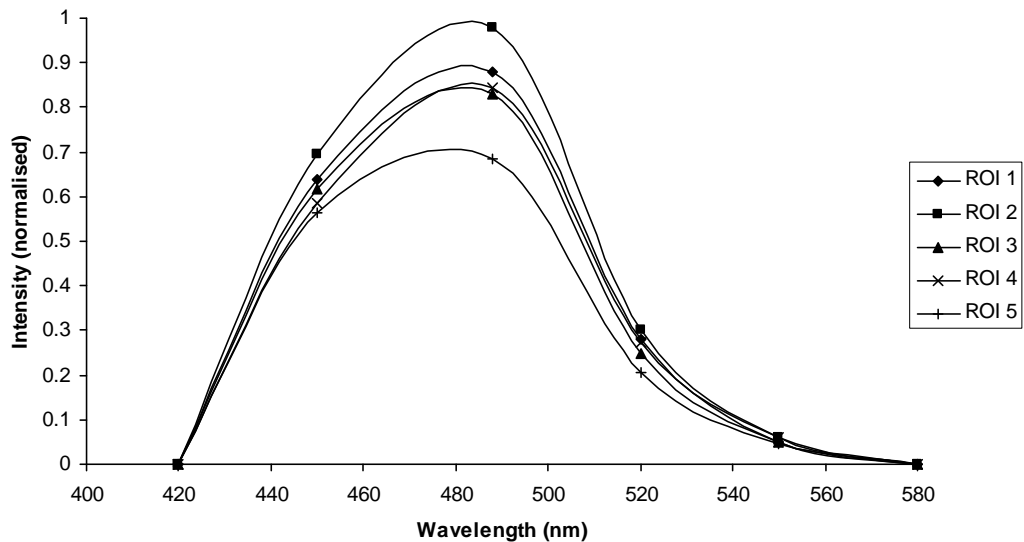


Figure 6.6 The normalized one photon DC spectral response. Each ROI equates to the relative labelled areas in Fig. 6.5, for each image.

Figure 6.6 shows the broad one photon DC response of the LED, which peaked at 485 nm. A standard deviation of 5 % was calculated for one photon DC OBIC data sets. Upon irradiating with wavelengths beyond 485 nm, sufficient energy could no longer be provided to exceed the bandgap of the device (which may vary through the p-n junction) and hence the OBIC signal dropped significantly. Additionally, as seen in Table 6.1, filtering the white-light spectrum below 420 nm provided insufficient power to provide any response. The excitation bandwidth over this range spans 65 nm at FWHM. This broad range of excitation clearly indicates that the excitation source for one photon DC OBIC need not be broadband or tunable and that less expensive sources may be used to observe a strong DC OBIC signal.

With regards to active region homogeneity, a maximum signal intensity difference of up to 30 % was measured between ROI 2 and 5. As described previously, any possibility of the LED having not been perpendicular to the excitation source was kept to a minimum through mounting upon a 3D gimble mount. This suggests that despite uniformity to within 10% between all other regions, ROI 5 appears to possess significant defects in the active region.

6.5.2 DC spectral response: two photon DC OBIC

The continuous wavelength tuning capabilities of the Ti:Sapphire laser provided a very flexible source of excitation for measuring the wavelength dependence of excitation upon optimal two photon DC OBIC signal generation,. The two photon DC OBIC signal relative to the excitation wavelength range is shown in Fig. 6.7. As described in Section 6.3.1, any fluctuations in two photon excitation power were compensated for using a quadratic relation and all data was normalised to the largest intensity.

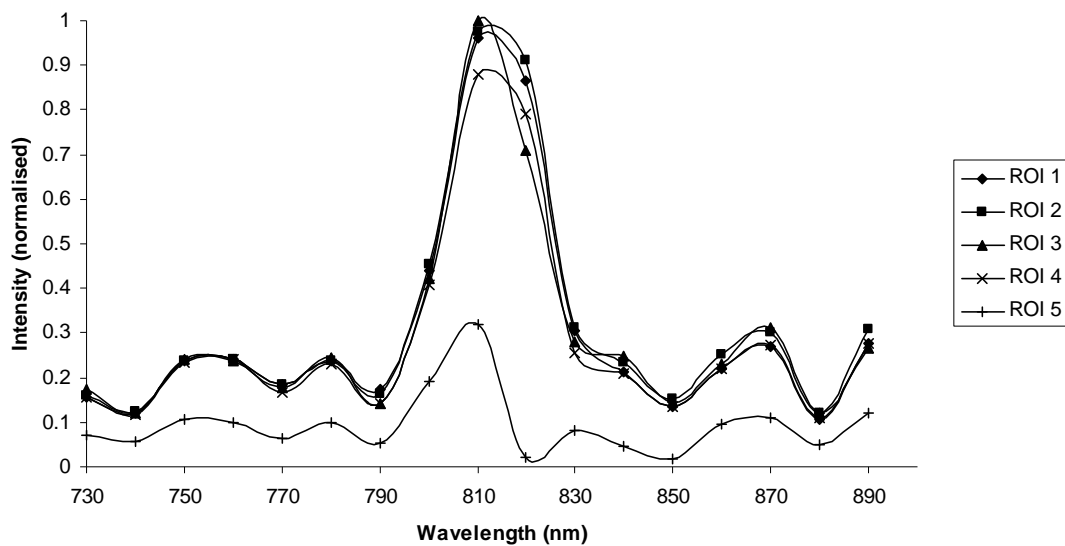


Figure 6.7 The normalized two photon DC response to wavelength tuning. Each ROI equates to the relative labeled areas in Fig. 6.5, for each image.

A standard deviation of 6 % was calculated for two photon DC OBIC data sets. It was found that the wavelength yielding the largest OBIC signal and hence that which gave most efficient excitation was 815 nm. This wavelength does not correspond to double the wavelength required for efficient one photon absorption, which was shown previously to be 480 nm. This can be explained by the mechanism of two photon absorption, which often does not occur at exactly double the wavelength of

the one photon process as a result of quantum mechanical selection rules [19]. It was also noted that the two photon excitation bandwidth of the device was much smaller at 25 nm (FWHM), when compared to one photon, which yielded a FWHM of 65 nm. From this result it was clear that there are much stricter excitation conditions for two photon, which highlight the importance of using a continuously tunable excitation source for two photon DC OBIC.

Similarly to one photon excitation, data from ROI 1-4 were found to exhibit comparable performances. However, for two photon DC OBIC, ROI 5 was substantially lower in amplitude than had been seen previously. A difference in amplitude between ROI 2 and 5 was found to be 70 % in comparison with 30 % for the equivalent ROIs in the one photon DC OBIC case. Upon analysis of the intensity across the two photon DC OBIC image (from left to right), it was found that a gradient in intensity was found. This drop-off in intensity became more prominent at the right hand side of the image (ROI 5). This behaviour is typical of imaging which is out of focus and was not experienced in any other dataset. Despite our efforts to reduce this effect through mounting of the device on a 3D positioner as previously described, it was subject to both drift and optical mis-alignment. Therefore it was appropriate to disregard information collected from ROI 5 in this dataset.

6.5.3 AC spectral response: two photon AC OBIC

Since the EOM used in these experiments was designed for use at NIR wavelengths, application of the EOM to the visible wavelengths of the SC source resulted in large losses. Consequently, upon reaching the sample there was insufficient excitation power available to perform one photon AC OBIC imaging. Given the near-infrared wavelengths of the Ti:Sapphire laser source, it was possible to employ the system for two photon AC OBIC and to compare the two photon AC OBIC spectral response with that of the two photon DC OBIC signal. A fixed modulation frequency of 200 kHz was used throughout the wavelength tuning. As in Section 6.5.2, the two photon

response was quadratically dependent upon excitation power and data was normalised to the highest intensity.

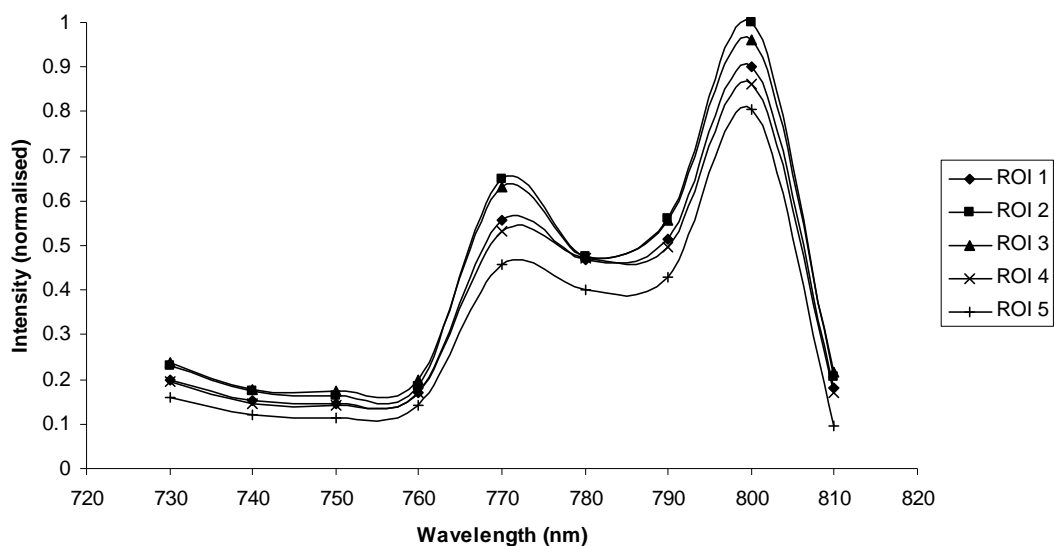


Figure 6.8 Two photon AC OBIC response to wavelength tuning of excitation source. Each ROI equates to the relative labeled areas in Fig. 6.5, for each image.

A standard deviation of 5 % was calculated for two photon AC OBIC data sets. From Fig. 6.8 it was seen that the peak two photon excitation was found at approximately the same wavelength as seen in two photon DC OBIC (Fig. 6.7) of around 800 nm. However, unlike the case for two photon DC OBIC, a much broader range of excitation yields a reasonable signal. This also encompasses a secondary, smaller, peak wavelength of excitation. For powers which were $\sim 10\%$ less than the power used for two photon DC OBIC, this equates to an excitation bandwidth of 40 nm (FWHM) and showed that the excitation wavelengths conditions for two photon AC OBIC were more flexible than for two photon DC OBIC. As a result, alternative fixed wavelength ultra-short pulsed lasers could be used as a source for excitation whilst maintaining reasonable signal in two photon AC OBIC.

It was found that the two photon AC response provided a more homogenous output across the five ROI analysed. The drift/misalignment which was highlighted in Section 6.5.2 was not found in two photon AC imaging. This was due to the continuous adjustments made to the system in order to reduce this effect. A variation of less than 20 % was found between the different ROIs.

6.5.4 Frequency modulation: two photon AC OBIC

As mentioned in Section 6.3.2., the inherent capacitance generated across an LED is proportional to the modulation frequency of the source. Use of the 76 MHz source would have resulted in effectively no AC signal detection, since when the repetition rate is in the MHz range, the active region effectively sees the source as cw, due to the LED having a slower response time than the interval between pulses. Therefore a range of pulse frequencies from 200 – 850 kHz were delivered through control of the EOM to determine the effect of varying the repetition rate for two photon AC OBIC imaging of the InGaN LED. A fixed wavelength of 800 nm was kept constant throughout the experiment, as this wavelength produced the maximum OBIC signal. A constant average power of 30 mW was provided at the sample for this experiment.

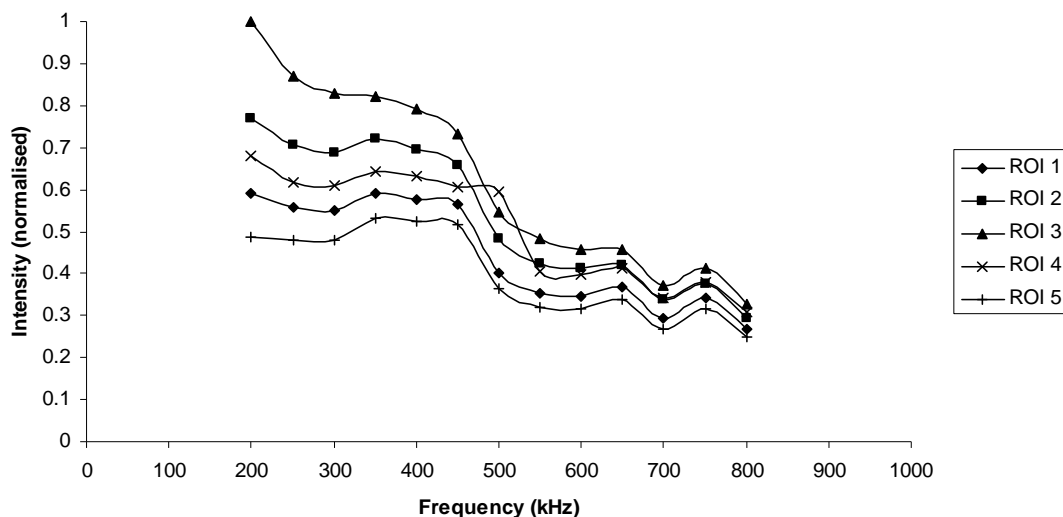


Figure 6.9 Two photon AC OBIC response to modulation of the excitation source. Each ROI equates to the relative labeled areas in Fig. 6.5, for each image.

A standard deviation of 8 % was calculated for two photon AC OBIC frequency modulation data set, which is shown in Fig. 6.9. As expected, a reduction of the modulation frequency led to an increase of up to 70 % in two photon AC OBIC signal when comparing 200 kHz and 850 kHz measurements. Reduction of the capacitance, i.e. noise, across the device, in turn allowed for better isolation of the signal. ROI 3 was most changed by a reduction in modulation frequency; the other regions provided more modest increases (10 – 35 %) for comparable frequencies.

It can also be seen from Fig. 6.9 that highest two photon AC OBIC response in signal intensity was found at the lowest frequency setting of the EOM (200 kHz). Using an alternative pulse picker which could select frequencies below this value would be likely to induce greater OBIC signal.

6.5.5 Phase variation: two photon AC OBIC

As described in Section 6.2, information regarding the response of the device can be obtained through analysing the phase difference between signal and lock-in reference (calculated from Eq. (6.2)).

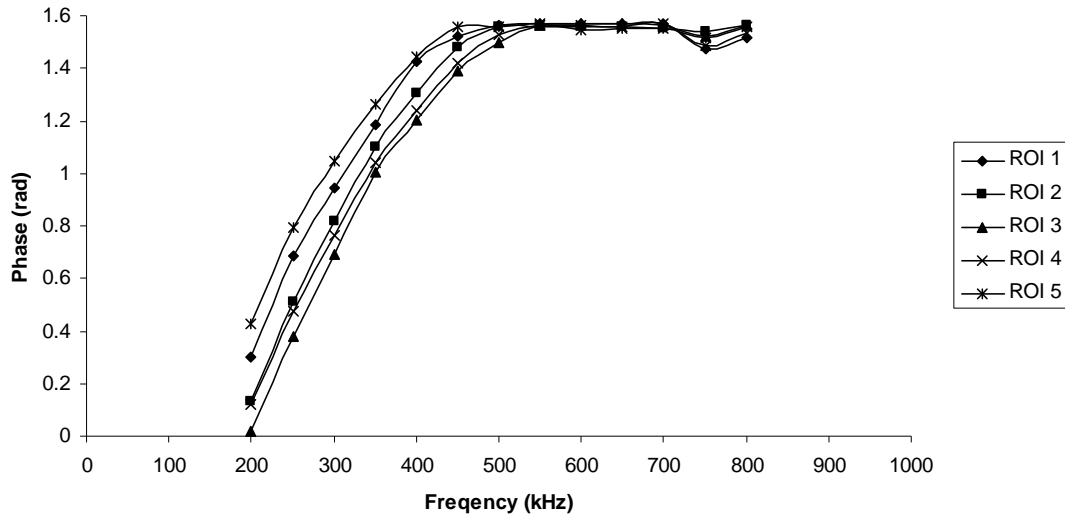


Figure 6.10 Two photon AC OBIC phase difference between signal and lock-in reference vs modulation frequency. Each ROI equates to the relative labeled areas in Fig. 6.5, for each image.

As the same datasets were used in Fig. 6.9 as in Fig. 6.10, a standard deviation of 8 % was also applied to data in Fig. 6.10. From this the phase relationship between OBIC signal and lock-in reference was shown as a function of modulation frequency. As the modulation frequency was decreased, the difference in phase was reduced. When the frequency was greater than 500 kHz, the phase difference between signal and lock-in neared $\pi/2$ and could be no further out of phase; therefore the signal could no longer be well isolated using the reference frequency. As a result, the signal that could be detected was greatly reduced, as seen in Fig 6.9. By demonstrating this phase difference at the various ROIs, it was clear that there was a substantial discrepancy across the active region of up to 0.4 radians. This highlights the non-uniform phase response from the LED, which was not possible to detect using DC techniques.

From this study, it was concluded that DC techniques are good methods for electronically mapping the surface of active regions within InGaN LEDs and for providing insight into the energy required to excite across the bandgap of the device. However, information regarding modulation frequency and phase variation across the sample are unique to AC techniques. These provide a more comprehensive assessment of the performance and quality of the device.

6.6 Conclusion

The expansive range of real world applications for InGaN devices has resulted in the need for techniques to increase their quality. In line with this need techniques for quality analysis are also considered vital. This study presented results obtained from the application of OBIC techniques to a green InGaN device, to determining the homogeneity of the active layer, from which it is possible to infer the performance of the LED.

Results from one photon and two photon DC OBIC experiments provided data regarding the peak spectral response of the InGaN device, occurring at 485 & 815 nm respectively. This data was useful for the determination of the bandgap of the device and providing the optimal operating conditions for efficient signal generation.

Additionally, excitation bandwidths of the device were found to be 25 & 65 nm at FWHM for one photon and two photon excitation, respectively. This showed that the wavelength tuning requirements for one photon excitation were less stringent than the case for two photon excitation. As a result of its broad excitation band, cheaper, discrete sources could be used for generation of one photon DC OBIC signal, whilst maintaining reasonable outputs.

Conversely, application of two photon DC OBIC required tunability as a result of the short band of excitation which was provided. Both of these methods demonstrated inhomogeneity across the InGaN device, to varying extents. A variation in signal amplitude of up to 30 % across the device could be seen in the one photon case. In the case of two photon excitation, ROI 1-4 followed similar trends, however up to a 70 % difference in signal was observed for ROI 5. This was deemed not to be an effect of inhomogeneity but rather a result of defocusing as a result of drift or optical misalignment.

Implementation of two photon AC OBIC to the InGaN LED provided additional information relative to the DC techniques. Analysis of the spectral response revealed an excitation bandwidth of 40 nm. This was shorter than the one photon DC OBIC bandwidth, however was substantially broader than the 25 nm bandwidth experienced with two photon DC OBIC. Therefore, whilst maintaining the advantages of two photon excitation, AC collection provided relaxed requirements upon the need for tunability of the excitation source. As AC signal was low, any capacitance build-up across the device would lead to increased noise and reduced detection. Therefore specific attention was paid to the modulation frequency of the excitation source. By scanning a range of frequencies in the kHz range, it could be seen that up to 70 % greater signal could be collected when operating at 200 kHz than at 850 kHz. This result was expected due to reduction in capacitance at lower frequencies. In addition to describing optimal operating conditions, it was possible to determine information regarding the site specific phase response across the device. With use of PSD it could be seen that the variation in signal phase compared to lock-in reference was inconsistent. A discrepancy of up to 0.4 radians could be found at compared regions, again highlighting the inhomogeneous response of the LED. Additionally, a cut-off of 500 kHz was identified whereby the difference between signal and reference becomes $\pi/2$. This corresponds to the frequency at which capacitance had increased until the signal could no longer be isolated by the reference.

This poor isolation is reflected in Fig. 6.9, where frequencies above 500 kHz exhibit low signal.

In summary, this chapter has highlighted the benefits and limitations of one photon and two photon DC OBIC as a technique for imaging of InGaN LEDs. The additional benefits incurred from the use of the 2P AC OBIC imaging technique, including frequency and phase dependencies, have been shown to be complementary to these techniques.

6.7 References

1. Holonyak Jr, N. and S. Bevacqua, *Coherent (visible) light emission from Ga (AsP) junctions*. Applied Physics Letters, 1962. **1**: p. 82.
2. Jianmin, Z. and Y. Wei. *Experimental investigation on the performance characteristics of white LEDs used in illumination application*. in *Power Electronics Specialists Conference, 2007. PESC 2007. IEEE*. 2007.
3. Ryu, S.-W., J. Park, J-K. Oh, D. H. Long, K-W. Kwon, Y-H. Kim, J-K. Lee, and J-H. Ki, *Analysis of Improved Efficiency of InGaN Light-Emitting Diode With Bottom Photonic Crystal Fabricated by Anodized Aluminum Oxidxe*. Advanced Functional Materials, 2009. **19**(10): p. 1650.
4. Esposito, E., F.J. Kao, and G. McConnell, *Confocal optical beam induced current microscopy of light-emitting diodes with a white-light supercontinuum source*. Applied Physics B: Lasers and Optics, 2007. **88**(4): p. 551.
5. Morkoç, H., *Semiconductor Lasers*. Handbook of Nitride Semiconductors and Devices. 2009: Wiley-VCH Verlag GmbH & Co. KGaA. 169.
6. Leamy, H.J., *Charge collection scanning electron microscopy*. Journal of Applied Physics, 1982. **53**(6): p. R51.
7. Wilson, T. and E. McCabe, *Theory of optical beam induced current images of defects in semiconductors*. Journal of Applied Physics, 1987. **61**(1): p. 191.

8. Van Dao, L., X. Wen, M. T. T. Do, P. Hannaford, E-C. Cho, Y.H Cho, Y. Huang and M.A. Green, *Time-resolved and time-integrated photoluminescence analysis of state filling and quantum confinement of silicon quantum dots*. Journal of Applied Physics, 2005. **97**: p. 013501.
9. Matsuda, K., T. Saiki, S. Nomura, M. Mihara and Y. Aoyagi, *Near-field photoluminescence imaging of single semiconductor quantum constituents with a spatial resolution of 30 nm*. Applied Physics Letters, 2002. **81**: p. 2291.
10. Azzini, G.A., G. Arman, and P. Montangero, *The scanning optical microscope: A powerful tool for failure analysis of electronic devices*. Microelectronics Reliability, 1992. **32**(11): p. 1599.
11. Yoshimoto, N., T. Matsuoka, T. Sasaki and A. Katsui, *Photoluminescence of InGaN films grown at high temperature by metalorganic vapor phase epitaxy*. Applied Physics Letters, 1991. **59**(18): p. 2251.
12. Feng, Z., W. Liu, S.J. Chua, J.W. Yu, C.C. Yang, T.R. Yang and J. Zhao, *Photoluminescence characteristics of low indium composition InGaN thin films grown on sapphire by metalorganic chemical vapor deposition*. Thin Solid Films, 2006. **498**(1-2): p. 118.
13. Kao, F.J., M-K. Huang, Y-S. Wang, S-L. Huang and C-K Sun, *Two-photon optical-beam-induced current imaging of indium gallium nitride blue light-emitting diodes*. Optics letters, 1999. **24**(20): p. 1407.
14. Stamm, U., H. Bergner, K. Hempel and A. Krause, *Techniques for picosecond OBIC measurement on ICs*. Microelectronic Engineering, 1992. **16**(1-4): p. 275.
15. Stengl, R., *High-voltage planar junctions investigated by the OBIC method*. Electron Devices, IEEE Transactions on, 1987. **34**(4): p. 911.
16. Kao, F.J., C. Chen, S-C. Shih, A. Wei, S-L. Huang, T-S. Horng and P. Török, *Optical beam induced current microscopy at DC and radio frequency*. Optics Communications, 2002. **211**(1-6): p. 39.
17. Daria, V.R., J.J. Miranda, and C. Saloma, *High-contrast images of semiconductor sites via one-photon optical beam-induced current imaging and confocal reflectance microscopy*. Applied optics, 2002. **41**(20): p. 4157.

18. Xu, C. and W. Denk, *Two-photon optical beam induced current imaging through the backside of integrated circuits*. Applied Physics Letters, 1997. **71**(18): p. 2578.
19. Mulligan, S. and B. MacVicar, *Two-photon fluorescence microscopy: basic principles, advantages and risks*. Modern Research and Educational Topics in Microscopy, A. Méndez-Vilas, and J. Díaz, eds.(FORMATEX, Badajoz, Spain, 2007): p. 881.

Chapter 7 Conclusion

7.1 Review

The work presented in this thesis represents advances in experimental nonlinear optics including, but not limited to, applications in optical microscopy.

Following a brief introduction to microscopy in Chapter 1, an overview of the nonlinear optical processes involved throughout this project were presented in Chapter 2 with particular attention paid to the choice of nonlinear crystal and the process of quasi-phase matching.

Chapter 3 provided an analysis of PPLN, the nonlinear material at the heart of Chapters 4 and 5. A comparative study of the periodic structure was performed using CLSM and MPLSM: by virtue of the luminescent properties of the nonlinear crystal dopant (MgO), it was possible to use this as a contrast mechanism for imaging of the poling structure. Using CLSM it was only possible to image close to the surface of the crystal. However, when performing MPLSM it was possible to observe the poled regions throughout the entire depth of the crystal. This is important, as through use of this technique, it was seen that structures observed close to the surface of the crystal were often deceiving with regards to the internal structure. Given the dependency of nonlinear optical conversion efficiency on period length, as described in Chapter 2, this approach provided a non-destructive and high-resolution measurement of inhomogeneities that would restrict the nonlinear conversion process.

The motivation for Chapter 4 was to improve the conversion efficiency of a SPOPO for three photon laser scanning microscopy. To date, with the exception of the work

presented in this chapter, all work involved either cw or ns-pulsed pump sources, whereas this research involved ultra-short pulses systems in a synchronous pumping geometry. Furthermore, this chapter describes an innovative bi-directional pump geometry and a comparison with the conventional single pass and double pass pump methods was presented. A nonlinear increase in conversion efficiency was observed using the novel bi-directional pump geometry, with an increase in peak output power of approximately 100% when compared with the single-pass approach. The developed high peak power source was then used as the basis for three photon laser scanning microscopy to overcome the substantial losses (of up to 90%) present within the commercial imaging platform. As a result of the efficiency of this geometry and the output powers obtainable, three photon laser scanning microscopy of fluorescent beads and various biological samples was performed.

Chapter 5 concerned SFM of the single pass SPOPO source described in Chapter 4 with the pump source for the SPOPO to create a sub-700nm ultra-short pulsed laser source for excitation of short-wavelength absorbing fluorophores. The need for such technology at wavelengths below the tuning range of Ti:Sapphire laser for two photon excitation of UV excitable samples was discussed. By careful choice of SFM geometry, a sub 400 fs, wavelength tunable output was generated (622 – 636 nm) at a maximum average power of 150mW. This laser system was applied to a home-built microscope, in order to perform two photon excitation imaging of a range of UV excitable fluorophores and autofluorescent samples. When performing comparative imaging using the industry standard Ti:Sapphire source, it was seen that the SFM source could provide up to 65 % greater signal from biological samples.

Chapter 6 described the materials analysis of InGaN LED sources using both an ultra-short pulsed Ti:Sapphire laser and a SC source. Through use of the OBIC technique and, in particular AC detection of the generated signal, it was possible to determine the frequency and phase responses of the device. In doing so, more

information could be gained regarding the homogeneity of the active region of the device.

7.2 Future work

There exist many opportunities for further work to expand the research outcomes presented in this thesis.

Regarding the materials analysis described in Chapter 3, this technique could be applied to alternative periodically poled materials with luminescent dopants for similar analysis. From this it would be possible to determine whether the inconsistencies observed within the PPLN sample described were found within other nonlinear crystals. The method could also be used to provide a comparison of poling techniques (i.e. electrical vs chemical).

Due to time restrictions and the availability of suitable samples, the OPO source which was described in Chapter 3 was not able to be applied to thick tissue sample. Ideally this would have been performed to highlight the additional depth penetration which is inherently possible through use of longer wavelengths. A comparison of the equivalent two and three photon absorption processes could be carried out. Additionally, the bi-directional pumping geometry developed within this chapter was very efficient and was extremely beneficial with regards to damage threshold conditions. As a result, it would be very interesting to apply this pump geometry to alternative nonlinear processes.

The spatial and temporal overlap of the OPO signal and excess pump described for the SFM experiments described in Chapter 5 are similar to the requirements needed for application of an OPO and pump source to a coherent anti-Stokes Raman

scattering (CARS) microscope. This type of microscopy uses a tunable source (i.e. such as an OPO) and a pump source to generate a signal which is the result of matching these frequencies to the inherent vibration of a specific molecule. With this type of microscopy exogenous labels are not required and therefore biological processes can be imaged without the interference of the labels which can often cause disruptions. An OPO CARS system has been shown previously [1, 2].

Chapter 6 highlighted characterisation of the important semi-conductor InGaN. The outcomes of the study have provided information on the tolerances and output characteristics of the laser sources required for both one photon and two photon AC and DC analysis. Due the tunability of the excitation sources used, it would be possible to analyse other important semi-conductors such as zinc selenide (ZnSe) and aluminium gallium phosphide (AlGaP). Additionally, it was not possible with the instrumentation described to perform one photon AC OBIC of the sample under investigation. To complete this study, a SC source with higher average output power would be highly desirable, particularly at lower wavelengths. As technology in this field improves, it is expected that such studies could be performed imminently.

7.3 References

1. Ganikhanov, F., et al., *Broadly tunable dual-wavelength light source for coherent anti-Stokes Raman scattering microscopy*. Optics letters, 2006. **31**(9): p. 1292.
2. Zhang, W., M. Parsons, and G. McConnell, *Flexible and stable optical parametric oscillator based laser system for coherent anti Stokes Raman scattering microscopy*. Microscopy Research and Technique. 2010. **73**(6): p. 650.